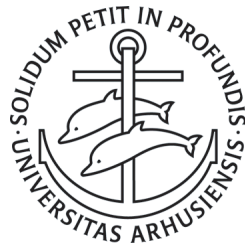
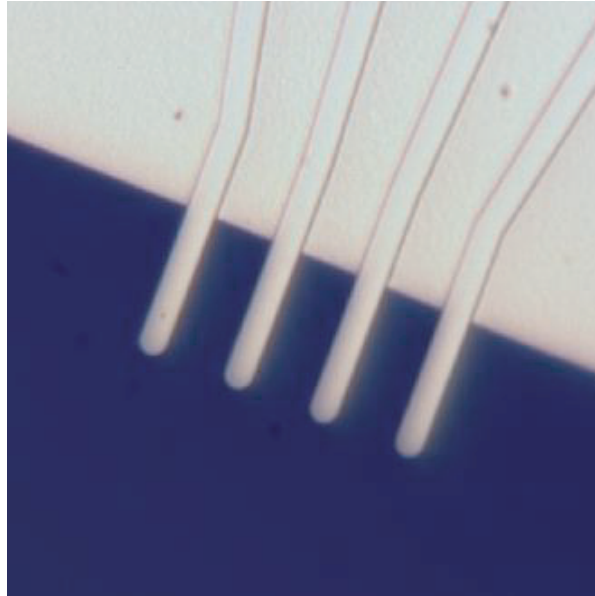


A combined study of the electronic structure
and transport properties of surfaces.



Ph.D. thesis

Justin Wells

July 2006

*Department of Physics and Astronomy,
University of Aarhus, Denmark.*

A combined study of the electronic structure
and transport properties of surfaces.

Justin Wells

July 2006

University of Aarhus

Abstract

This thesis is a study of the geometric, electronic and transport properties of surfaces. In particular, a semiconductor (silicon) and a semi-metal (bismuth) are investigated.

In a previous study of the geometric structure of the Bi(111) surface based on electronic structure measurements, an unusually large surface relaxation has been reported. In this thesis, this is extracted from LEED-IV measurements, and in contradiction to the earlier work, the surface relaxation is found to be very small.

Previous studies of the electronic structure report the existence of a charge density wave on this surface, and the electron-phonon coupling strength is reported to be unusually high. In this thesis, it is shown that the possibility of a charge density wave can be excluded, and that the electron-phonon mass enhancement parameter takes the more realistic value of 0.4.

Although much is already known about the electronic and geometric properties of silicon surfaces, little is known about the surface conductivity, and previous reports are far from consistent. Therefore, in this thesis, new experimental and theoretical approaches are developed and applied to clean and adsorbate covered Si(111) surfaces.

The conductivity of the clean Si(111)(7×7) surface is found to be very low (around $10^{-9} \Omega^{-1}$) which is consistent with the surface being a poor metal. Also, increasing the step density of the surface is found to increase the conductivity by more than an order of magnitude. At high temperatures, the increased conductivity of the space-charge region results in the conductivity measurements no longer being surface sensitive.

Silver thin films on Si(111) have also been investigated. When a network of percolating islands is prepared, the conductivity is enhanced by about 5 orders of magnitude (relative to the (7×7) surface), and exhibits typical metallic behaviour. The Si(111)($\sqrt{3} \times \sqrt{3}$)Ag surface also shows enhanced conductivity relative to the (7×7) surface, and the conductivity is seen to change by 2 orders of magnitude as a result of a geometry altering phase transition.

Dansk Resumé

Denne afhandling er en undersøgelse af de geometriske og elektroniske egenskaber samt transportegenskaberne af overflader. I særdeleshed er en halvleder (silicium) og et semimetal (bismut) studeret.

Tidligere undersøgelser af Bi(111) overfladens geometriske struktur, som har været baseret på målinger af den elektroniske struktur, viser en usædvanlig stor relaksation af de øvre lag. I denne afhandling er det samme undersøgt ved LEED-IV målinger som viser den modsatte konklusion; at denne relaksation er lille.

Ligeledes har tidligere målinger af den elektroniske struktur understøttet eksistensen af en elektron-tæthedsbølge på overfladen samt en usædvanlig stærk elektron-fonon kobling. I denne afhandling bliver det vist, at det er muligt at udelukke eksistensen af elektron-tæthedsbølgen og at elektron-fonon masseforøgelsesparameteren har en mere realistisk værdi på 0.4.

Selvom meget allerede er kendt om de elektroniske og geometriske egenskaber af silicium-overflader, er det begrænset hvad der vides om overfladens ledningsevne, og de tilgængelige kilder er langt fra konsistente. Derfor er der i denne afhandling udviklet nye eksperimentelle og teoretiske metoder og anvendt på rene- og adsorbatdækkede Si(111) overflader.

Den rene overflades ledningsevne af Si(111)(7×7) er meget lille (omkring $10^{-9} \Omega^{-1}$), hvilket stemmer overens med at overfladen er et dårligt metal. Ved at øge tætheden af trin på overfladen vil ledningsevnen øges med mere end en størrelsesorden. Ved høje temperaturer vil den øget ledningsevne af rumladningslaget resultere i at målinger ikke længere er overfladefølsomme.

Derudover er der foretaget et studie af tynde sølvfilm på Si(111). En prøve forberedt med et netværk af perkolerende sølvøer øger ledningsevnen med fem størrelsesordner (i forhold til (7×7) overfladen) og viser typisk metallisk opførsel. Si(111)($\sqrt{3} \times \sqrt{3}$)Ag viser også en øget ledningsevne sammenlignet med (7×7) overfladen, og det viser sig at ledningsevnen ændres med to størrelsesordener på grund af den geometriske alternerende faseovergang.

Contents

Abstract	i
Dansk Resumé	ii
1 Introduction	1
1.1 Motivation	1
1.2 The Contents and Layout of this Work	2
1.2.1 Publications	3
2 The Surface Geometric Structure: Bi(111)	5
2.1 Introduction	5
2.2 Method	6
2.3 LEED calculations	8
2.4 Results: Structural Determination	8
2.5 Conclusion	12
3 The Surface Electronic Structure: Bi(111)	13
3.1 Introduction	13
3.2 The Bulk and Surfaces of Bismuth	13
3.3 Investigating the Electronic Structure	16
3.3.1 Measuring the Electron-Phonon Mass Enhancement	16
3.3.2 Spin Orbit Coupling and its Consequences	21
3.3.3 Experimental Setup	24
3.4 Results	25
3.4.1 Estimating the Mass Enhancement Parameter	26
3.4.2 Evidence Against a Charge Density Wave	26
3.5 Conclusion	28
4 Transport Measurements	30
4.1 Multi-Point Probe Measurements	30
4.1.1 Introduction	30
4.1.2 Theory	30

4.1.3	Experimental Setup	35
4.2	Measurements of Si(111)	44
4.2.1	Introduction	44
4.2.2	Experimental Details	55
4.2.3	Results	60
4.2.4	Conclusions	69
4.3	Understanding the Measurements of Si(111) Surfaces	70
4.3.1	Introduction	70
4.3.2	The Models	70
4.3.3	Results: Modeling the Conductance	81
4.4	Conclusion	88
5	Summary and outlook:	90
5.1	Overview of Present work	90
5.1.1	The Surface Geometric Structure	90
5.1.2	The Surface Electronic Structure	90
5.1.3	Transport Measurements	91
5.2	The Outlook	91
5.2.1	Novel Surfaces for Future Study	92
5.2.2	Instrumental Limitations	96
5.3	Conclusion	98
6	Acknowledgements	99
6.1	General Comments	99
6.2	Specific Acknowledgements	99
6.2.1	Chapter 2: The Surface Geometric Structure	100
6.2.2	Chapter 3: The Surface Electronic Structure	100
6.2.3	Chapter 4: Transport Measurements	100
6.2.4	Chapter 5: Conclusions and Outlook	100
	List of Abbreviations	101
	Bibliography	103

Chapter 1

Introduction

1.1 Motivation

Studying the physical properties of surfaces is fascinating for a number of reasons; not only are the chemical properties of a solid dictated by its surface, but also surfaces represent quasi two-dimensional systems which act as a testing ground for some interesting fundamental physical concepts. One field which remains largely unexplored is the transport properties of surfaces. This is surprising since electronic devices are already reaching the scale at which their surface properties are important. Perhaps the explanation for this lack of study is the practical difficulty associated with the measurements.

The transport properties of many surfaces have not been directly studied, however, from other measurements, some of the expected properties can be inferred. For example, by studying the electronic properties of surface states, a surface can be claimed to be "metallic" or "semiconducting" although in some cases, what this really means in terms of the expected conductivity has been the source of some confusion. However, it is clear that the electronic properties of a surface are expected to influence the transport properties, but a direct link remains elusive.

Although one would expect the electronic properties to strongly influence the transport properties, other factors are also significant. For example it is well known that electron-phonon interactions and electron-impurity interactions have a strong influence on the bulk transport properties, so one could expect the same to be true for surfaces.

The motivation for this work is to increase our understanding of the properties of surfaces, especially the surface conductivity and some of the factors which influence it. The current understanding - compared to the case of the bulk - is rather poor, despite the surface properties being of increasing applied interest as well as of fundamental interest.

1.2 The Contents and Layout of this Work

This thesis is divided into three main sections; investigations of geometric structure (chapter 2), electronic structure (chapter 3) and transport properties (chapter 4). Finally, in chapter 5, some preliminary measurements on other interesting materials are presented and the future possibilities and limitations are discussed.

The techniques and theory for investigating the geometric properties are already well established, therefore chapter 2 is a brief summary of the application of these techniques to the interesting (111) surface of bismuth.

The investigation of electronic structure of the Bi(111) surface in chapter 3 also uses well established techniques. However, in order to understand the electron-phonon coupling strength, and how the spin split nature of the surface prohibits the formation of a charge density wave, a more in-depth look at the theory and analysis is required.

In contrast to these investigations, the study of the transport properties of surfaces in chapter 4 requires a much more in-depth look at theory and practical issues. Since the technique used is much less established, the majority of this thesis (and indeed the majority of the practical work in this project) is concentrated on the development of the technique, and in ensuring the correct interpretation of the measurements.

Throughout this work the investigations are primarily focussed on two materials; a typical semiconductor (silicon), and a typical semi-metal (bismuth):

Over the last 50 years silicon has been extensively studied. However, some mysteries still remain. Surprisingly, the nature of the Si(111) surface with the characteristic (7×7) reconstruction still remains the subject of controversy. Whilst recent measurements of the electronic structure have been interpreted as evidence of a metallic surface, the limited measurements available of the surface conductivity are spread over several orders of magnitude. Other reports indicate that the surface may be close to a metal-insulator transition.

In this study, the Si(111) (7×7) surface is chosen for a number of reasons; the electronic and geometric structure have been extensively studied, and thus there is no need to continue this - instead an investigation of the surface transport properties can be focussed upon. Also, the controversy over the nature of this surface gives rise to the challenge of providing a conclusive answer.

One of the advantages of studying the transport properties in the surface of a well known semiconductor is that the bulk properties can be "selected". By comparing samples with a different bulk doping, the surface and bulk influences upon the measurements can be separated. Similarly, the surface

can be modified - for example by the deposition of silver - thus providing another way to make the same distinction between surface and bulk.

The main disadvantage of using a semiconducting bulk is that the bending of the bulk bands close to the surface gives rise to a space charge region which can somewhat complicate the interpretation of the measurements. Thus, understanding the behaviour of the space charge region is important.

The (111) surface of the semi-metal bismuth has also been studied. This is an interesting system since the bulk is known to be poorly conducting (relative to other metals), but the electronic structure of the surface states indicates that the surface may be a significantly better metal.

Some previous measurements of the electronic and geometric structure of this surface have been reported, however some apparent contradictions remain; for example experimental evidence of the seemingly prohibited charge density wave, the unusual surface relaxation and the unusually high electron-phonon coupling strength which have been reported are worthy of further study. Therefore, in this work measurements of the electronic and geometric structure of Bi(111) are performed.

1.2.1 Publications

Much of the work contained in this thesis has also been published elsewhere. This section contains a summary of my relevant publications, and their connection with this thesis. The contributions made by my many co-authors are acknowledged in chapter 6.

1.2.1.1 Chapter 2; The surface geometric structure

The contents of this chapter, along with further details of the calculations, have been published as reference [1][I].

1.2.1.2 Chapter 3; The surface electronic structure

Most of the contents of this chapter have been published as references [2][II] and [3][III]. The deconvolution process - which is mentioned briefly in section 3.3.1 is discussed in more detail in reference [4][IV].

1.2.1.3 Chapter 4; Transport measurements

The measurements performed in the latter part of this chapter are currently under submission [5][V].

1.2.1.4 Chapter 5; Conclusions and outlook

This chapter draws on a number of publications: The K_3C_{60} measurements are currently in preparation [6][VI], whilst some of the measurements on K_6C_{60} are published as reference [7][VII]. The measurements on organic semiconductors can be found in references [8][VIII], [9][IX], [10][X] and [11][XI].

Chapter 2

The Surface Geometric Structure: Bi(111)

2.1 Introduction

Bi(111) is by far the most important of the bismuth surfaces for practical applications since it is the natural cleavage plane, and also the preferred direction of epitaxial growth. This is explained by the unusual bilayer structure of the bulk; parallel to the (111) plane, the crystal structure consists of closely separated pairs of layers, or bilayers, with 3 *intra*-bilayer covalent bonds per unit cell. These bilayers are relatively weakly bonded together, similar to the interlayer bonding of graphite. It is therefore not surprising that the natural cleavage plane is in the (111) direction. Furthermore, since the interaction between bilayers is weak, one would expect the surface relaxations to be small.

For such an interesting material, it is surprising to find that there is a very limited amount of structural information available: From the pioneering work of Jona [12], a hexagonal (1×1) Low Energy Electron Diffraction (LEED) pattern was found for this surface, and thus the surface was assumed to be terminated with an intact bilayer. This assumption was supported later by a Scanning Tunneling Microscopy (STM) study by Édel'man *et al.* [13], in which only double layer steps were found.

In the work of Ast and Höchst [14], the geometric structure is estimated from measurements of surface state dispersion and from tight binding calculations. Whilst this work supports the supposition that the surface is terminated by an intact bilayer, they estimate the first *intra*-bilayer relaxation to be unusually large; so large, in fact, that the first *intra*-bilayer spacing becomes larger than the *inter*-bilayer spacing thus implying an entirely different bonding scheme.

This work highlights that the surface geometric structure is not well un-

derstood and is worthy of further study; in this chapter, the structure of the Bi(111) surface is studied using LEED Intensity versus Voltage (LEED-IV) analysis and first-principle calculations in order to definitively resolve the geometric structure.

2.2 Method

The experiment was performed in a μ -metal chamber with a base pressure of $< 1 \times 10^{-10}$ torr. The basic experimental setup is described in references [1, 15, 16][I], however a few small modifications were made to the chamber for these experiments:

The gas lines were rebuilt to incorporate greater flexibility; a tap board was constructed with valved connections to the rotary pump, turbo pump, main chamber, auxiliary ion pump, argon gas cylinder, liquid N₂ vent and sputter gun. This resulted in a number of improvements, the most important being that a much better base pressure could be achieved in the sputter gas line thereby reducing the contamination of the sputter gas. The chamber and pumping sections could be vented using liquid N₂; this reduces the influx of water during venting and thus allows the baking time to be shortened. Also, the chamber and pumping sections could be vented independently, removing the need to bake the entire chamber. In fact, for preliminary experiments, it was not necessary to bake the system at all, since pressures of $< 5 \times 10^{-10}$ torr could be achieved without baking.

The Bi(111) crystal was mounted on the manipulator, and a K-type thermocouple was attached to the back of the sample in the usual way (see ref [16] for details). The sample was cleaned by repeated cycles of Ar⁺ sputtering and annealing to 150 °C.

Sputtering was carried out at an incidence angle of 45 ° relative to the sample normal, using an argon pressure of $\approx 5 \times 10^{-6}$ torr and an accelerating potential of 1 kV. This corresponded to a sputter current of $\approx 2\mu\text{A}$.

In order to align the sample with the ion beam all light sources (such as the ion gauge) were switched off and the argon pressure and accelerating potential were increased so that the ion beam could be seen. A photograph of the ion beam and sample manipulator is shown in figure 2.1.

The surface cleanliness was checked using Auger Electron Spectroscopy (AES). After three cycles of sputtering and annealing no contamination was observable. Thus, the maximum oxygen contamination is estimated as < 0.02 monolayers.

The LEED measurements were made using a simple PC controlled LEED unit and 16-bit Peltier cooled CCD camera. The PC software enabled a

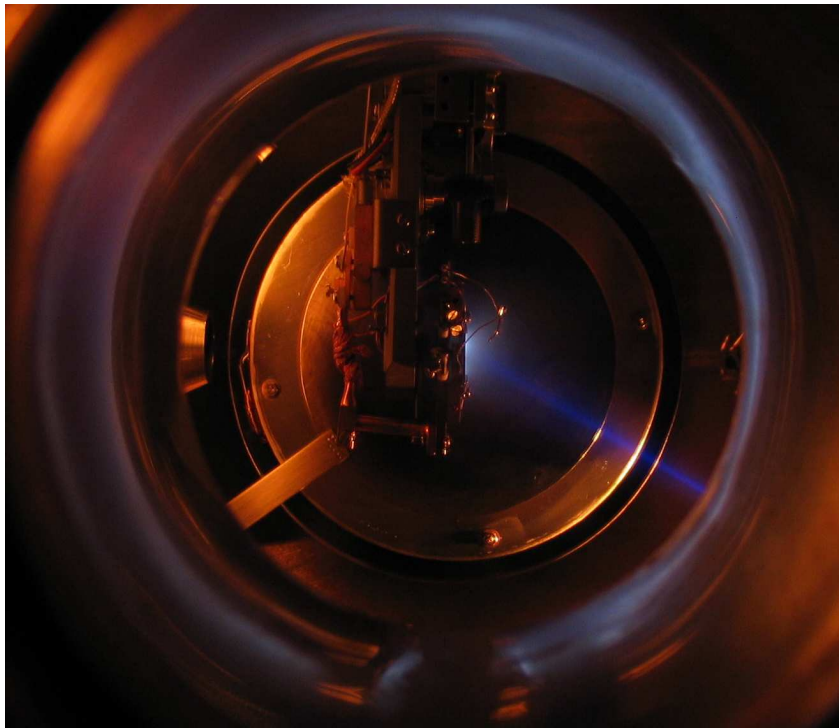


Figure 2.1: Photograph through a viewport of the LEED chamber. The Ar^+ beam and its incidence with the sample manipulator can be seen. The covered LEED screen can be seen in the background.

series of photographs to be taken whilst the electron energy was increased. The back-illuminated, Peltier cooled CCD chip guaranteed an extraordinarily high quantum efficiency.

Although the measurements were in principle very simple, it was found that the quality of the results was strongly dependent on the accuracy of the alignment. Positioning the sample precisely in front of the LEED screen involved careful control of the many degrees of freedom provided by the sample manipulator (including 3 linear drives, two rotational controls and tilt adjustment). Aligning the camera precisely with the LEED screen was similarly complex. Approximate alignment could be achieved by careful measurements of the geometry. For fine-tuning it was necessary to measure the energy dependent intensity and position of the LEED spots which are known to be symmetry-equivalent, and then make adjustments so that they were indeed measured to be symmetry-equivalent.

Photographs were taken at 1 eV intervals in the energy range 30 eV to 350 eV, and the integrated intensity of every diffracted beam was extracted. The measurements were repeated over the temperature range 140 K to 313 K.

2.3 LEED calculations

The dynamic LEED calculations were performed using the computer code of Adams [16, 17] which was developed from the programs of Pendry [18], Van Hove and Tong [19]. For further details, see reference [1][I].

Self consistent *ab initio* calculations of the surface crystal structure of Bi(111) were also performed. The evaluation of the surface relaxation was carried out for a symmetric 14-layer film, both with and without the inclusion of a spin orbit coupling term. Further details of these calculation can also be found in reference [1][I].

2.4 Results: Structural Determination

After some initial tests, models involving a split bilayer termination could be discounted on the grounds of the poor agreement with the experimental data. This is not surprising since such a termination involves breaking the three covalent bonds per unit cell which hold the bilayer together, instead of separating the weakly bonded bilayers. This is also consistent with the bulk mechanical observation that bismuth cleaves easily along the (111) plane.

The models involving an intact bilayer termination showed good agreement with experimental data. The structural and non-structural parameters were

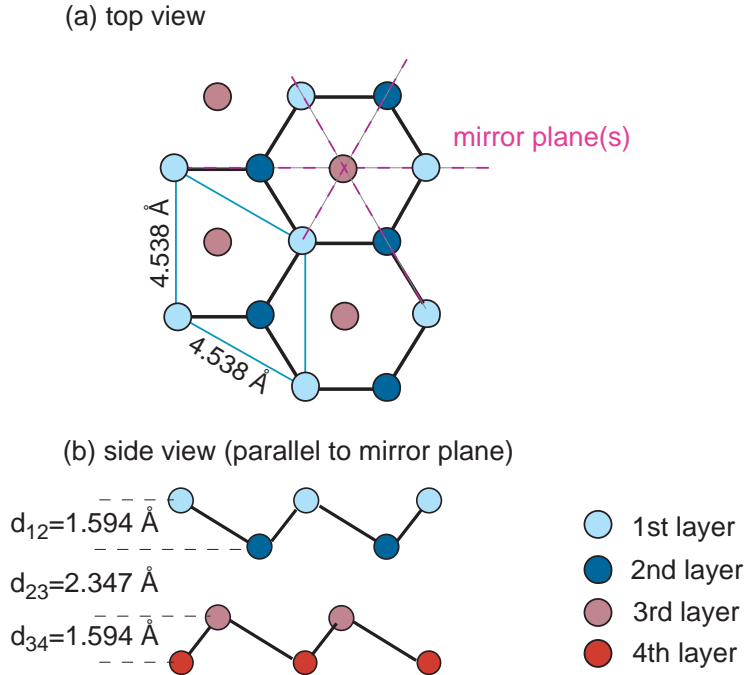


Figure 2.2: Truncated bulk structure of Bi(111). The black solid lines indicate covalent bonds. a) A top view showing the first three atomic layers and b) a side view of the first four atomic layers along a mirror plane. The bilayer structure is evident.

initially taken to be that of the truncated bulk (illustrated in figure 2.2). These parameters could be refined using the procedure outlined in reference [1][I]. In this way, the relaxations of the surface layers (at 140 K) can be estimated as $d_{12}=1.602 \pm 0.002 \text{ \AA}$, $d_{23}=2.393 \pm 0.002 \text{ \AA}$ and $d_{34}=1.594 \pm 0.002 \text{ \AA}$. By comparison with the truncated bulk structure shown in figure 2.2, this represents relaxations of $(+0.5 \pm 1.1) \%$, $(+1.9 \pm 0.8) \%$ and $(0.0 \pm 1.1) \%$, respectively.

Both the measured and calculated LEED IV curves are plotted in figure 2.3. The figure shows the plots of 10 symmetry in-equivalent beams (the average of the symmetry equivalent beams are plotted in each case). Thus a total energy range of over 2000 eV is used. The calculations show very good agreement with the measured data.

Additionally, the LEED IV measurements contain information on the atomic vibrational amplitudes, and thus also the Debye temperature. This is because the atomic vibrations lead to a damping of the diffracted intensities via a Debye-Waller factor. From the "Root Mean Square" (RMS) vibrational amplitudes, the Debye temperature can be calculated; see references [1, 18][I]

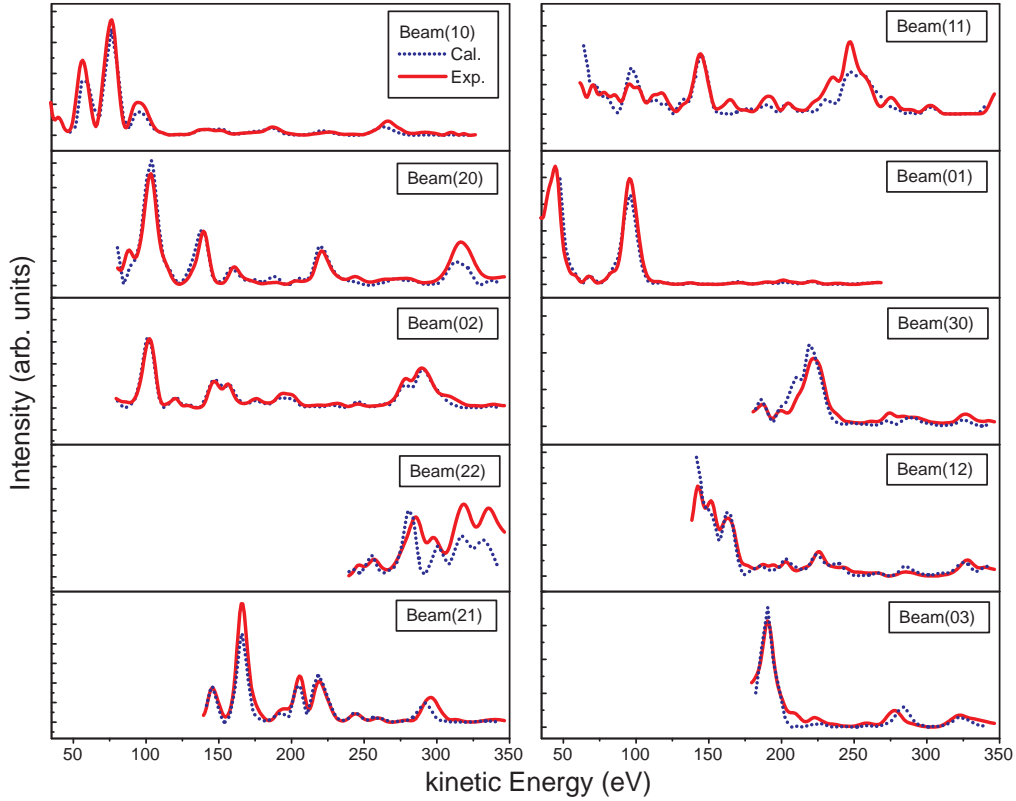


Figure 2.3: Comparison of experimental (solid lines) and calculated (dotted lines) LEED Intensity-versus-voltage plots for the symmetry inequivalent beam of Bi(111) at normal incidence and at 140 K. The intensities of symmetry-equivalent beams have been averaged. The total energy range is 2079 eV, and the Pendry R-factor is 0.075.

for details. Using this method, the Debye temperatures of the first and second layers are estimated as 71 ± 6 K and 77 ± 8 K respectively; this is significantly less than the bulk value of 120 K reported in reference [20]. The reduction of the Debye temperature at surfaces is a common phenomena [21], and these results are in good agreement with earlier findings [22].

So far, this discussion has been based only on the lowest temperature (140 K) measurements. Since the measurements were repeated at a range of temperatures up to 313 K, the temperature dependence of these parameters can also be discussed. The complete set of optimised parameters are given in table 2.1. The method by which the uncertainties are estimated is described in reference [1][I].

T (K)	No. of beams	ΔE (eV)	$\frac{\Delta d_{12}}{d_{12}^b}$ (%)	$\frac{\Delta d_{23}}{d_{23}^b}$ (%)	u_1 (Å)	u_2 (Å)	Θ_{D1} (K)	Θ_{D2} (K)	R factor
140	10	2079	0.5 ± 1.1	1.9 ± 0.8	0.239 ± 0.019	0.222 ± 0.020	71^{+7}_{-5}	77^{+8}_{-7}	0.075
171	10	2068	0.0 ± 1.1	2.1 ± 0.8	0.256 ± 0.019	0.237 ± 0.020	74^{+6}_{-5}	80^{+7}_{-6}	0.084
218	9	1375	0.4 ± 1.3	2.0 ± 0.9	0.260 ± 0.023	0.248 ± 0.023	82^{+8}_{-7}	86^{+8}_{-5}	0.072
268	9	1207	0.4 ± 1.5	1.6 ± 1.1	0.284 ± 0.024	0.268 ± 0.024	83^{+8}_{-6}	88^{+8}_{-7}	0.069
313	7	555	0.4 ± 2.9	1.0 ± 1.9	0.289 ± 0.049	0.266 ± 0.049	88^{+18}_{-13}	96^{+12}_{-11}	0.043

Table 2.1: The optimised parameters at a range of temperatures from 140 K to 313 K. The table shows; the number of symmetry inequivalent beams used in the calculation, the total energy range (ΔE), the relaxations of the first two interlayer spacings relative to the truncated bulk, the R.M.S vibrational amplitudes of the first two layers (u_1 and u_2), the Debye temperatures of the first two layers (Θ_1 and Θ_2) and the Pendry R-factor.

From the table, it can be seen that the first interlayer spacing is approximately independent of temperature, whilst the second interlayer spacing gradually decreases with increasing temperature. By applying a linear fit to the relaxations, the relaxations at 0 K can be extrapolated. This gives $\Delta d_{12}/d_{12}^b = +(1.2 \pm 2.3) \%$ and $\Delta d_{23}/d_{23}^b = +(2.6 \pm 1.7) \%$ and these values are directly comparable to those from the first principles calculations in ref [1][I]: $\Delta d_{12}/d_{12}^b = +0.6 \%$ and $\Delta d_{23}/d_{23}^b = +6.2 \%$. It can be seen that the first interlayer distance is in agreement with the calculated value, and whilst the second interlayer distance lies outside of the estimated experimental uncertainty, the agreement is still reasonable in view of the remaining

uncertainties in the theory [1][I].

The Debye temperatures for the atoms in the first and second layers are found to be temperature dependent. Although this seems counter-intuitive, it is also observed for the bulk Debye temperature [20], and is explained as being due to the simple approximations on which the Debye model is based.

2.5 Conclusion

In conclusion, it would appear that the geometric structure of the Bi(111) surface has now been resolved. The measurements and calculations consistently point to a surface structure similar to that of a simple truncated bulk. The surface appears to be terminated, not surprisingly, with an intact bilayer. The *intra*layer relaxation of this bilayer is very small, and the relaxation of the first two bilayers is a little larger.

The measurements and calculations not only compliment each other, but also compliment the intuitive understanding of the surface described in the introduction. However, these findings are not consistent with those of Ast and Höchst who, in reference [14], report a first layer relaxation of $\Delta d_{12}/d_{12}^b = +71\%$ from measurements of surface state dispersion and from tight binding calculations. The most incredible effect of such a relaxation is that this makes the *intra*-bilayer spacing larger than the *inter*-bilayer spacing, and thus would require an entirely different arrangement of the near-surface bonds.

A closer inspection of reference [14] reveals that there are several possible reasons for this discrepancy. In particular, the method used by Ast and Höchst relies on a complex fit of the measured electronic structure to that estimated using a simple tight binding approximation. This is basically a fit of many free parameters to a rather approximate model, and therefore it is not surprising that it can yield physically unrealistic values.

On the other hand, the analysis of the LEED-IV measurements presented in this chapter, and the comparison with first principles calculations yields the geometric structure more directly. Although the spin-orbit coupling has been included, this approach also gives realistic relaxations when it is excluded. This is discussed in more detail in reference [1][I].

The question of the spin orbit interaction in the Bi(111) surface is of great significance. In chapter 3 the importance of spin-orbit coupling in the understanding of the electronic structure also becomes evident.

Chapter 3

The Surface Electronic Structure: Bi(111)

3.1 Introduction

Bulk bismuth displays typical semi-metallic behaviour. The limited studies available of the Bi(111) surface indicate that it is metallic. However, the surface is still not completely understood. Perhaps one of the reasons for the lack of understanding of this surface is that the measurements are challenging to perform.

Recent studies by Ast and Höchst illustrate this: Their report of a Charge Density Wave (CDW) [23] and the unusually high value of the electron-phonon mass enhancement parameter [24] are somewhat surprising, and are therefore worthy of further study.

In this chapter, the technique of Angle Resolved Ultra Violet Photoemission Spectroscopy (ARUPS), which is used for investigating the electronic properties, is introduced. The results of measurements on Bi(111) are then presented and discussed.

3.2 The Bulk and Surfaces of Bismuth

Many of the interesting bulk properties of bismuth are due to its bulk electronic structure; such as its classification as a semimetal. A theoretical description of the bulk structure has been the focus of some attention; perhaps the most notable are the tight binding calculations of Liu and Allen [25], which show good agreement with the experimental measurements, however this is not surprising since the tight binding parameters were optimised such that the calculations reproduced the measured Fermi surface. Also, Gonze *et al.*

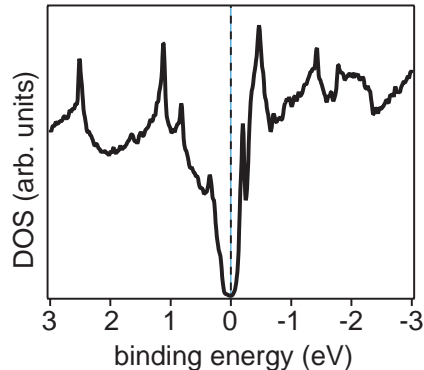


Figure 3.1: The bulk density of states close to the Fermi level (from reference [34]). Calculated from the tight binding parameters of Liu and Allen. The semi-metallic nature of bulk bismuth is apparent. [25].

[26] have performed the *ab initio* calculations which, despite the difficulties associated with the small energy scales involved, have been quite successful.

Studies of the dispersion of the bulk states away from the Fermi level have been carried out by ARUPS [27–33], and the results are generally quite consistent with calculations.

From reference [34], it is clear that the bulk density of states at the Fermi level is reduced by several orders of magnitude relative to the density of states away from the Fermi level (as illustrated in figure 3.1). The carrier density is found to be very low, around $3 \times 10^{17} \text{ cm}^{-3}$, and the effective mass of the carriers is also found to be very small (around $0.003m_e$ for electrons along the trigonal axis) [25].

Thus, the bulk electronic structure of bismuth shows all the typical indications that it is a poor metal, and indeed it is found experimentally that the bulk conductivity is 2 orders of magnitude less than for a "good metal" such as copper [35].

Measurements of the surface electronic structure of Bi(111) have been performed by several groups. The first experiments were performed by Jezequel *et al.* [27–29], whilst experiments on thin films were performed by Tanaka *et al.* [31, 32]. The most important result of this early work was that the Bi(111) surface supports a surface state. Later work by Patthey *et al.* using higher energy resolution [36] confirms this, and shows that the surface state contains several components.

An important result of the work by Patthey *et al.* is that a high photoemission intensity at the Fermi level was observed, and this is not expected for a semi-metal such as bismuth. An even higher resolution study by Hengsberger *et al.* [30] was interpreted in terms of a modified bulk Fermi surface. The fi-

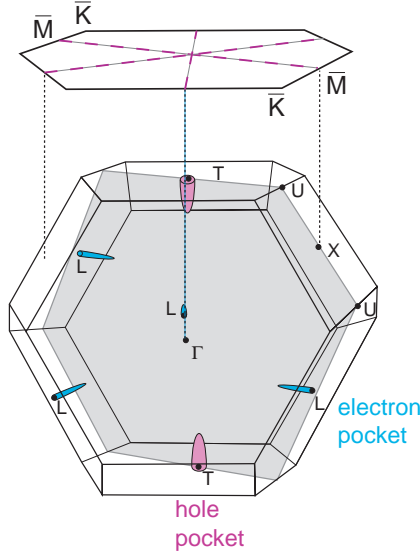


Figure 3.2: The bulk Brillouin zone of bismuth, and the projection on the (111) surface. The main features of the bulk Fermi surface are depicted (not to scale). The three mirror lines of the Bi(111) surface Brillouin zone are depicted by dashed pink lines.

nal clarification came from Ast and Höchst [24, 37]; the surface Fermi surface around $\bar{\Gamma}$ was found to consist of a hexagonal ring plus six narrow lobes, and a detailed study of the dispersion of these states reveals that the hexagonal ring encloses filled states whilst the lobes enclose empty states, termed electron and hole pockets respectively. By probing these states over a range of photon energies, both the electron and hole pockets were found to be surface states, and the Fermi velocities were estimated and found to be unusually high. The conclusion of this work is that the number of surface carriers, relative to that of the projected bulk, is high. This has important implications since it means that the surface is a better metal than the bulk.

The bulk Brillouin zone of bismuth, and the projection onto the (111) surface, are shown in figure 3.2. Normal emission corresponds to sampling in the $\Gamma - T$ direction. The bulk Fermi surface elements are projected onto the surface Brillouin zone and the electron pockets are found close to the \bar{M} points whilst a hole pocket is found close to $\bar{\Gamma}$. Nowhere else can there be bulk states close to the Fermi level.

Perhaps one of the reasons for the lack of understanding of this surface is that the measurements are challenging to perform; the small energy scales and low effective masses require high energy- and momentum- resolutions and the low Debye temperature results in final state broadening by phonon assisted transitions.

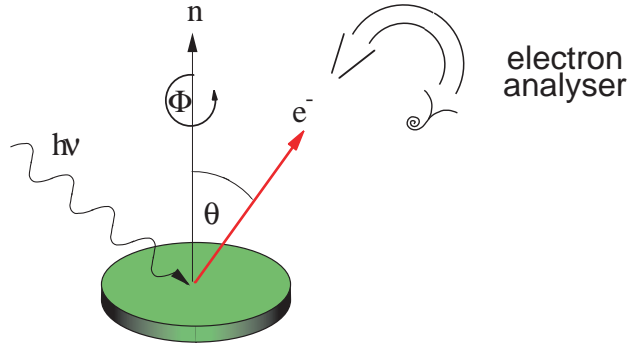


Figure 3.3: Figure to illustrate the principle of ARUPS. A photon with energy $h\nu$ is incident with the sample, and the emitted electron is detected with an angle- and energy-sensitive detector.

3.3 Investigating the Electronic Structure

A variety of techniques are available which allow the electronic structure to be probed. Such techniques include; Inverse Photo-Emission Spectroscopy (IPES) which principally provides information on the unoccupied states, scanning probe methods such as scanning tunneling spectroscopy (STS), which can provide localised information on both the occupied and unoccupied states, and a wide range of optical techniques.

In this study, ARUPS is the technique of choice. ARUPS can provide a wealth of information about the occupied states of the system, but correctly extracting the required information can be rather complex. This is discussed in more detail in the following sections.

3.3.1 Measuring the Electron-Phonon Mass Enhancement

Many thorough reviews exist on the principles of photoemission in general [38] and of ARUPS in particular [39–43]. A useful overview is provided in the Ph.D thesis of Ch. Søndergaard [44]. The extraction of the mass enhancement parameter using ARUPS can also be found in more detail elsewhere [2, 45][II].

The principle of ARUPS is depicted in figure 3.3. It is basically a refinement of the photoelectric effect. A photon with sufficient energy $h\nu$ is incident with the sample, and this excites an electron such that it is emitted from the sample. The electron is detected by an angle- and energy-resolving detector.

By counting the electrons emitted from the sample as a function of energy and angle (both azimuthal and polar), detailed information about the occupied and unoccupied parts of the electronic structure can be obtained.

However, the measured function will be broadened by the finite resolutions of the photon source and detector.

In the past, the instrumental resolutions have been such that this technique could only be used to map the initial-state, and to some extent the final-state, band structure of crystalline solids. However, recent improvements in the instrumental resolutions have allowed the intrinsic lineshapes of photoemission spectra to be studied, an approach pioneered by Kevan *et al.* [40]. This has proven to be of great interest since the intrinsic linewidth contains information on the many-body effects of the solid.

Several thorough treatments of ARUPS [38, 41, 46] and the relationship with the spectral function exist [2, 43, 45, 47–50][II]. The spectral function basically describes the probability of finding an electron at a given energy and angle. From these reports, it can be shown that ARUPS of a quasi two-dimensional system yields the initial state spectral function convoluted with the detector and source resolution functions. The spectral function (\mathcal{A}) is given by:

$$\mathcal{A}(\omega, \vec{k}, T) = \frac{\pi^{-1} |\Sigma''(\omega, T)|}{[\hbar\omega - \epsilon(\vec{k}) - \Sigma'(\omega, T)]^2 + \Sigma''(\omega, T)^2}. \quad (3.1)$$

where $\hbar\omega$ is the energy, \vec{k} is the two-dimensional crystal momentum vector, T is the temperature and $\epsilon(\vec{k})$ is the single-particle dispersion. Σ' and Σ'' are the real and imaginary parts of the self-energy, respectively. The self-energy is assumed to be independent of \vec{k} [45]. The spectral function is fully described by the single-particle dispersion and the self-energy. Since the self-energy contains information on the many-body interactions, it is this quantity which we wish to extract from the measurement.

In order to separate the spectral function from the instrumental resolution functions, two possible approaches can be used: Either the instrumental functions can be deconvolved from the measured spectra [4][IV], or more commonly, the instrumental resolutions can be minimised such that they can be considered to be negligible.

In order to measure the spectral function, two common measurement modes are used. A Momentum Distribution Curve (MDC) is a measurement performed at constant kinetic energy whilst the emission angle, and therefore \vec{k} is scanned. Alternatively, an Energy Distribution Curve (EDC) is a measurement performed at constant emission angle, whilst the kinetic energy is scanned. Whilst it is tempting to say that an EDC is measured at constant \vec{k} , this is not strictly correct since \vec{k} also depends on the energy, although under certain conditions this distinction can be neglected [45, 51–53].

EDC measurements of the spectral function present several problems. If one ignores the problem of \vec{k} not being constant throughout the measurement,

and if one assumes that the real part of the self energy is zero and that the imaginary part does not depend on ω , then the spectral function takes the following simplified form:

$$\mathcal{A}(\omega, \vec{k}, T) = \frac{\pi^{-1} |\Sigma''(T)|}{[\hbar\omega - \epsilon(\vec{k})]^2 + \Sigma''(T)^2} \quad (3.2)$$

This is simply a Lorentzian with a Full Width Half Maximum (FWHM) of $2|\Sigma''(T)|$, centred at $\epsilon(\vec{k})$. However, when $\epsilon(\vec{k})$ is small (relative to the FWHM), then the lineshape is also affected by the Fermi-level cut-off - which is, of course, temperature dependent.

MDC measurements, on the other hand, are somewhat simpler to interpret. Considering only one direction in \vec{k} space, the spectral function is simply a Lorentzian of FWHM = $2|\Sigma''(\omega)/v|$ with the maximum at $k_{\max} = (1/v)(\hbar\omega - \Sigma'(\omega))$. v is the local velocity, and the origin of the coordinate system is the Fermi-level crossing.

A simulation of the spectral function (from reference [2][II]) is shown in figure 3.4. The simulation shows that it is difficult to extract the self-energy from the complex EDC curve shape, whereas for the MDC it is comparatively simple.

It is now possible to extract information on the self energy from EDC and MDC measurements. Since the self energy contains information on the processes which limit the hole lifetime, it should also be possible to extract information on such processes, including the electron-phonon coupling.

In a crystalline solid, the three main processes which limit the hole lifetime are electron-electron, electron-impurity and electron-phonon interactions. For the time being, the former two processes will be ignored, and it will be assumed that the only significant interaction is the electron-phonon interaction (the validity of this assumption will be reassessed at the end of this section). Thus, considering only the electron-phonon contribution, the imaginary part of the self energy can be expressed as:

$$|\Sigma''(\omega, T)| = \pi\hbar \int_0^{\omega_m} d\omega' \alpha^2 F(\omega') [1 - f(\omega - \omega') + 2n(\omega') + f(\omega + \omega')] \quad (3.3)$$

where $\alpha^2 F(\omega)$ is the so-called Eliashberg coupling function, ω_m is the highest phonon frequency, n and f are the Bose and Fermi distributions, respectively [45].

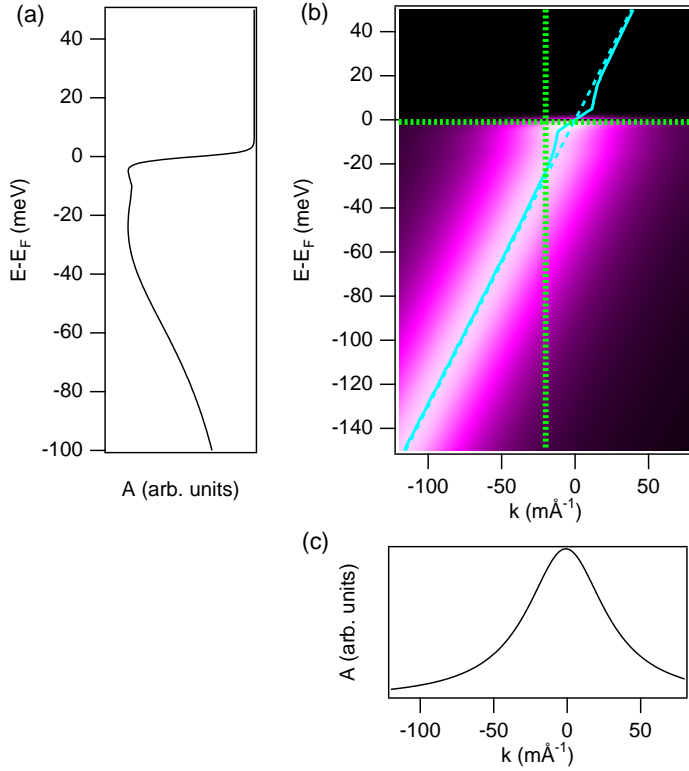


Figure 3.4: (a) An EDC taken at $k = -20 \text{ m}\text{\AA}^{-1}$ from (b); the simulated spectral function near the Fermi level crossing for a state with a linear dispersion with $\lambda = 2.4$. The blue dashed line is the bare dispersion and the blue solid line the renormalised dispersion. (c) An MDC taken from (b) at the Fermi energy. The position of the MDC and EDC are marked in panel (b) by green dotted lines.

In general, the electron-phonon mass enhancement parameter (λ) can be evaluated from the Eliashberg coupling function by means of the following relationship:

$$\lambda = 2 \int_0^{\omega_m} d\omega' \alpha^2 F(\omega') / \omega'. \quad (3.4)$$

Thus, in order to extract λ , the imaginary part of the self energy has to be determined and fitted to equation 3.3. In order to do this, a model for the Eliashberg coupling function is required. One such model is the Debye model, although other models have also been applied [47].

Since this fitting procedure requires several free parameters, it is difficult to accurately extract λ . This is especially true when the uncertainty in the measurement of the imaginary part of the self energy is significant, and this can easily be the case when it is estimated from EDC linewidths close to the Fermi level.

Fortunately, a simpler approach also exists; in the high temperature limit (i.e. $kT \gg \hbar\omega_{max}$), equation 3.3 takes an especially simple form:

$$\Sigma'' = \pi\lambda k_B T. \quad (3.5)$$

This limit is particularly useful since it no longer depends on the nature of the phonon model.

So far, this discussion has been limited to the electron-phonon interactions. However, in a real system, the electron-electron and electron-impurity interactions may also be significant. Fortunately, in most cases, the temperature dependence of these interactions is insignificant in comparison to the electron-phonon interaction, and thus can be treated as being temperature independent. Therefore, the MDC linewidth in the high temperature limit becomes:

$$\text{FWHM} = \frac{2(\pi\lambda k_B T + W_0)}{v} \quad (3.6)$$

where W_0 is a constant offset. Thus λ can now be extracted from the temperature dependence of the MDC linewidth.

For bismuth surfaces, the electron-phonon mass enhancement parameter has been studied little. For the Bi(100) surface, Gayone *et al.* have estimated λ from the temperature dependent linewidth of the surface state at a range of binding energies [54]. λ is shown to lie within the range 0.2 to 0.7 and to be dependent on the binding energy.

For the (111) surface, Ast and Höchst have estimated λ from the real part of the self energy [24]. In this work, λ is estimated as 2.3 ± 0.2 assuming a

surface Debye energy of 5 meV. This value of λ is exceptionally high, especially when compared to the (100) surface.

3.3.2 Spin Orbit Coupling and its Consequences

From a theoretical standpoint, the dispersion of the surface states of Bi(111) can be calculated with and without the inclusion of spin orbit interaction. This has been carried out by Koroteev *et al.* using first principle calculations [55] and the results are shown in figure 3.5. The figure shows two possible band structures: When the spin-orbit interaction is ignored, the calculations produce one band (depicted in black) which is spin degenerate and thus includes two electrons per k -point. When the spin-orbit interaction is included, the calculations produce two separate bands containing one electron per band (depicted in red). These spin-split bands are only degenerate at high symmetry points, such as at $\bar{\Gamma}$.

From an experimental standpoint, the dispersion of the surface states can be measured using ARUPS (using the facility described in section 3.3.3). The results of the measurement are shown in figure 3.6, and the first principles calculations of Koroteev *et al.* which include the spin orbit coupling are superimposed on the experimental data.

By considering the excellent agreement between these calculations and the experimental data, there can be little doubt that the surface states are spin-split.

This means that each band contains only one spin direction, and thus a spin direction can be assigned to the features of the Fermi surface. Figure 3.7 shows an illustration of the spin directions for the hexagonal electron pocket.

The same is not true for bulk bismuth. In both the bulk and the surface, time-reversal symmetry dictates that there must be degeneracy between states with energy $E(\vec{k}, \uparrow)$ and $E(-\vec{k}, \downarrow)$. However, in the bulk, inversion symmetry dictates that there must also be degeneracy between states with energy $E(\vec{k}, \uparrow)$ and $E(-\vec{k}, \uparrow)$. The combination of these two conditions results in the bulk bands being spin-degenerate. However, the breaking of the symmetry at the surface results in the inversion symmetry condition being lost, thus it is expected that a \vec{k}_{\parallel} dependent splitting of the surface bands can occur.

Reduced dimension systems, for example this quasi 2-dimensional surface, are good candidates for instabilities such as CDWs [56]. Several such cases have been reported in recent years [57, 58]. In fact, the existence of a CDW has even been proposed for the Bi(111) surface [23]. One important consideration is the condition of "nesting", which the Bi(111) surface appears to support. Nesting occurs when the Fermi surface consists of parallel compo-

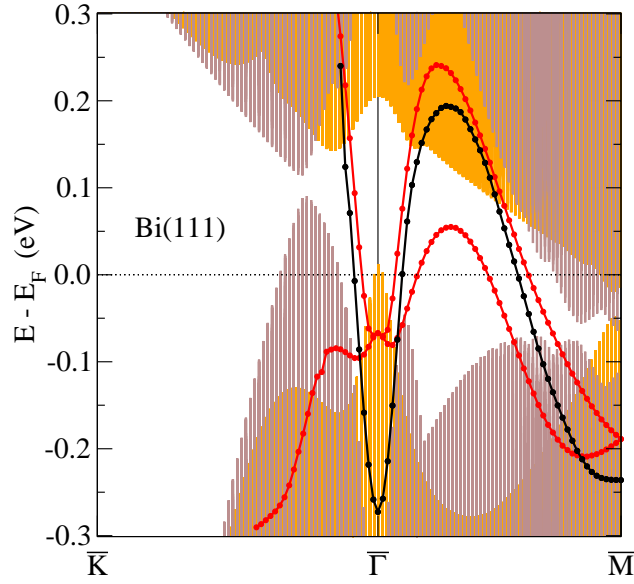


Figure 3.5: The calculated electronic structure of Bi(111). The surface states are shown both including (red lines) and excluding (black lines) the Spin Orbit Coupling (SOC) term. The shaded areas show the projected bulk bands both with (yellow) and without (violet) SOC.

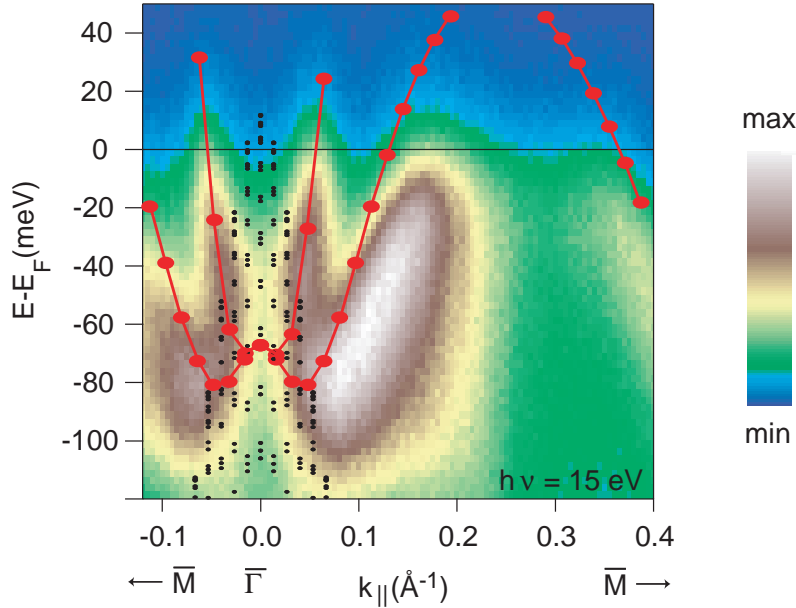


Figure 3.6: The measured photoemission intensity in the vicinity of the $\bar{\Gamma}$ high symmetry point for Bi(111). The projected bulk bands are depicted by small black dots (calculated using the tight binding parameters of Liu and Allen [25]). The red markers and lines depict the surface state band calculations (including the SOC term) from figure 3.5 and reference [55].

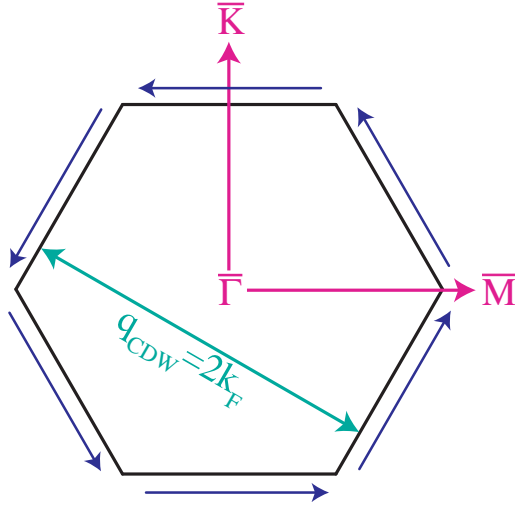


Figure 3.7: Depiction of the Fermi surface of Bi(111) around $\bar{\Gamma}$, showing the hexagonal electron pocket (black solid lines) and the spin directions (dark blue arrows). The "nesting vector" q_{CDW} is shown in blue-green.

nents on opposite sides of a high symmetry point; this allows a redistribution of the charge at a minimal energy cost and thus a charge density wave can be supported.

In this case, the Fermi surface of the electron pocket is hexagonal (see figures 3.7 and 3.8), and thus the above criterion appears to be fulfilled; two parallel sides of the hexagonal ring are separated by the so-called "nesting vector" $q_{CDW} = 2k_F = 0.106 \text{ \AA}^{-1}$ (according to Ast and Höchst [23]). The "nesting" condition is also apparent from considerations of the Lindhard susceptibility (χ): For a hexagonal Fermi surface, χ has a singularity at $q = 2k_F$, which is indicative of an instability.

Since the surface states are spin-split, the spin directions associated with a transition must also be considered. In this case, by considering time reversal symmetry, the opposite sides of the hexagon must have opposite spin. This means that a transition from one side of the hexagon to the other requires the spin direction to be reversed, and can thus be ruled out as a viable transition. This is illustrated in figure 3.7.

With this in mind, there is an apparent contradiction: Whilst Ast and Höchst report spectroscopic evidence of a CDW, it would appear that such a phase transition cannot occur for this surface because of the spin-split nature of the surface states, therefore a closer look at this discrepancy is called for.

In the work of Ast and Höchst [23], the principle evidence for the CDW is the temperature induced gap opening seen between 50 K and 75 K (see

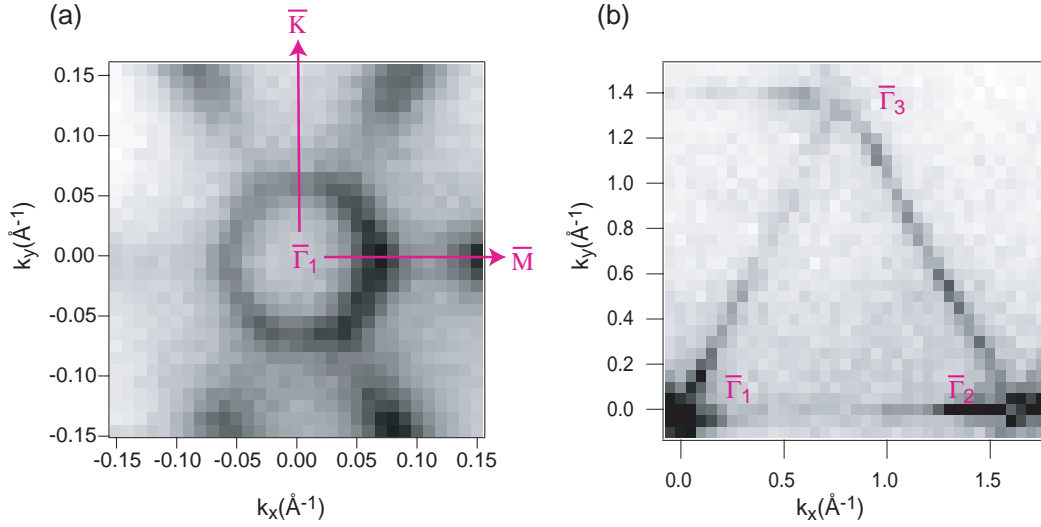


Figure 3.8: The photoemission intensity at the Fermi level (Fermi surface map) of the Bi(111) surface. (a) The distinctive hexagonal electron pocket around the $\bar{\Gamma}$ high symmetry point and the "lobes" of the hole pockets in the $\bar{\Gamma} - \bar{M}$ directions are observable [$h\nu = 15$ eV and $T = 30$ K]. (b) a large scale Fermi surface map to determine the sample orientation and workfunction [$h\nu = 25$ eV and $T = 30$ K].

figure 3 within reference [23]). The gap opening is relatively small (around 10 meV) and thus good energy resolution is required. More subtly, good angular resolution is also required since the state at the Fermi level crossing is relatively narrow (see figure 3.6). This also highlights the need for accurate angular positioning since a small change in the angle would shift the EDC away from the crossing and could thus be interpreted as an opening of the gap.

3.3.3 Experimental Setup

From the preceding section, one can see the need for high energy and momentum resolution measurements. This not only requires a high resolution electron analyser, but also a high resolution photon source. Since much intensity is lost achieving high resolution, the photon source must also have high intensity. There are also some further considerations; the light source must be well focused and stable, the system must be free of electrical noise and external fields, and the sample surface must be free from contamination for the duration of the measurements.

The photon source of choice is a synchrotron undulator, since this provides high brilliance light over a wide energy range. In this case, the SGM3 beamline

of ASTRID is used. The light is monochromated and focused by means of a spherical grating monochromator. In fact, three gratings are available so that the energy range of the monochromator can be extended. Details of the original beamline can be found in reference [59], although several modifications have been made since, such as upgrading the gratings. The position and focus of the beam was evaluated by using a luminescent sample, in this case SiC.

The electron spectrometer is an ARUPS-10 manufactured by VG Ltd. The energy resolution is variable, and at best it was found to be around 25 meV, and the angular resolution is also variable, and at best was found to be 0.2° . The energy resolution is practically limited by electrical noise, therefore the chamber is connected to a designated earth, and extra steps are taken to reduce the sources of noise.

The sample manipulator allows movements in the 3 linear directions as well as rotation around the vertical axis. The sample position is chosen using the intersection of two lasers, thus giving a positional accuracy better than 1 mm. The angular position is tested by reflecting a laser from the sample, and measuring the position of the reflection. This allows repeatable positioning within about 0.05° .

The sample can be heated or cooled during the measurement by means of a helium cryostat and a filament heater, with feedback provided by a K-type thermocouple, thus allowing temperatures in the range 28 K to over 600 K to be achieved. In order to minimise electrical noise, the thermocouple is optically decoupled from the temperature controller. Also, the heater is pulsed and the measurement is synchronised such that the measurement cannot be made whilst the heater is on. Typically, the heater is used for 0.15 seconds every 1.00 seconds, thus allowing measurements to be made during 85 % of the cycle.

The bismuth sample is prepared by cycles of annealing and argon ion bombardment by means of a simple sputter gun. The surface cleanliness and order can be checked by a range of techniques including AES and LEED.

The measurements are carried out in two conjoined vacuum chambers with a base pressure of around 7×10^{-11} mbar, thus giving a sample lifetime in the order of several hours (assuming a sticking coefficient close to unity).

Further details of the experimental setup can be found in reference [44].

3.4 Results

In the following section, the measurements made on the Bi(111) surface are reported. Temperature dependent MDC's are presented and from this, the electron-phonon mass enhancement parameter is extracted. Evidence against

the proposed CDW is then presented.

3.4.1 Estimating the Mass Enhancement Parameter

As discussed in section 3.3.1, ARUPS can be used to provide information on the electron-phonon coupling. In particular, the temperature dependent linewidth of MDCs taken close to the Fermi level can allow the imaginary part of the self energy to be estimated. From this, it is possible to estimate the mass enhancement parameter λ .

The measurements are shown in figure 3.9, along with an example of the fitting procedure used. The hole state indicated by a solid fit-line can be seen to broaden across the temperature range 48 to 298 K. From this broadening, the imaginary part of the self energy is extracted and this is plotted in part (b) of the same figure. A linear fit to this temperature dependence reveals the mass enhancement parameter to be $\lambda = 0.40 \pm 0.05$. The quality of the fit is seen to be very good. Since these measurements are made in the high temperature limit of equation 3.3, this result is independent of the parameters of the phonon model.

It is interesting to compare this result with that of Ast and Höchst [24] who have also studied the mass enhancement for the same hole state. Assuming a Debye energy of 5 meV (which is realistic for such a state [22], and is consistent with the value of 6.9 meV which can be extracted from Table 2.1), they find $\lambda = 2.3 \pm 0.2$, which clearly disagrees with our result.

There are several possible causes for this discrepancy. Firstly, in the work of Ast and Höchst, an incorrect expression is used for the renormalised dispersion. However, this is thought to have a small effect on the analysis. The more important difference is that Ast and Höchst estimate λ from the real part of the self energy as extracted from the renormalised dispersion close to the Fermi level. Since the change in linewidth when approaching the Fermi level is very small, the finite spectrometer resolution is significant, and thus makes this a rather problematic approach. This is discussed in more detail in reference [45].

3.4.2 Evidence Against a Charge Density Wave

The results of our measurements on Bi(111) are shown in figure 3.10. Figure 3.10(a) shows temperature dependent EDC measurements made at the Fermi level crossing, which are comparable with those of Ast and Höchst. From these measurements it is apparent that the 10 meV gap opening reported by Ast and Höchst [23] does not occur within the temperature range 44 to 103 K.

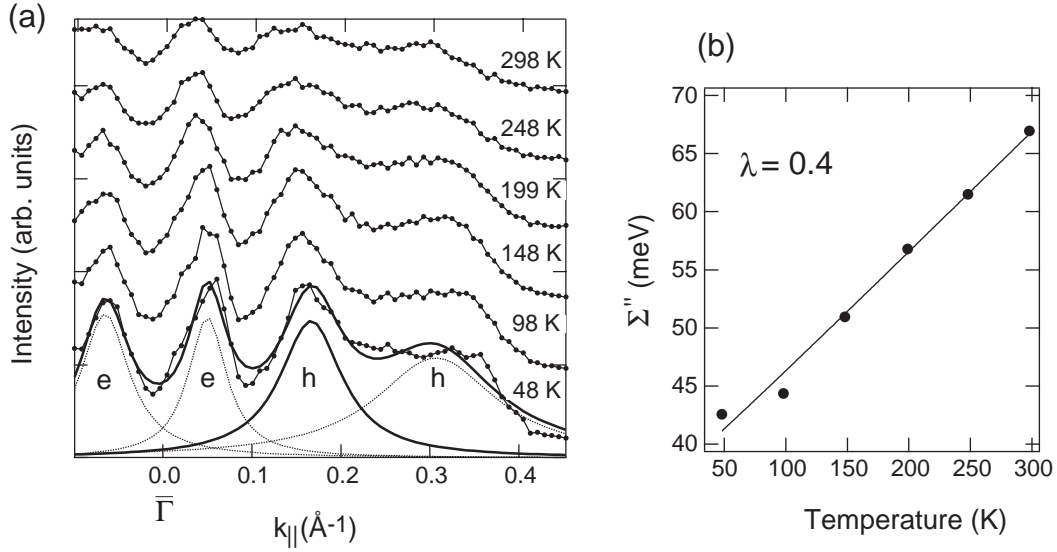


Figure 3.9: (a) Temperature dependent MDCs at a binding energy of 25 meV in the $\bar{\Gamma} - \bar{M}$ direction. For the lowest temperature, the fitted curve is also shown; it comprises 4 Lorentzian peaks, the component depicted by the solid line is the hole state of interest. From this the imaginary part of the self energy was extracted, and this is shown versus temperature in panel (b). A linear fit to this temperature dependence was made, and thus the mass enhancement parameter (λ) was estimated.

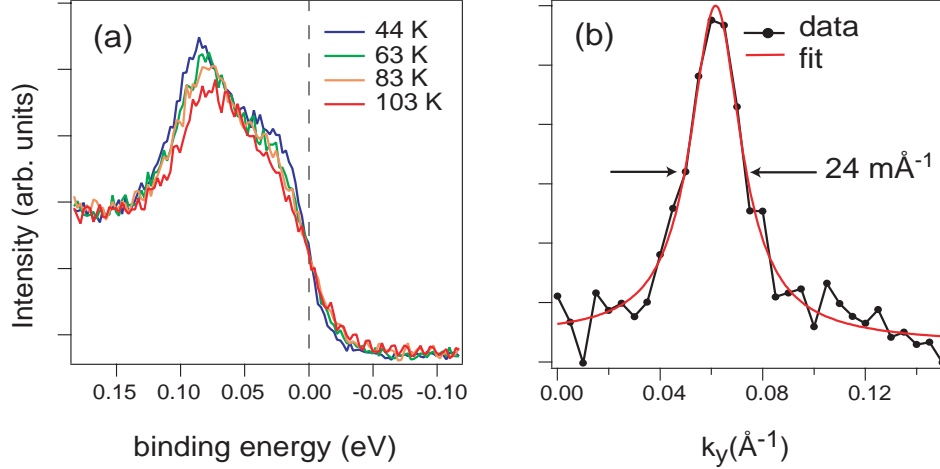


Figure 3.10: (a) EDCs taken at the Fermi level crossing in the $\bar{\Gamma} - \bar{K}$ direction as a function of temperature and (b) MDC at the same crossing (with Lorentzian fit) [$h\nu = 15 \text{ eV}$ and $T = 30 \text{ K}$].

Since the expected gap opening is quite small and since the state is very steep, good energy and momentum resolutions are required. From the measurements shown in figure 3.10(a), the energy resolution can be estimated as 26 meV, and from figure 3.10(b) the momentum resolution is estimated at $24 \text{ m}\text{\AA}^{-1}$. This is comparable to that of Ast and Höchst, and thus the gap opening reported by them in reference [23] should also be apparent in these measurements.

Perhaps the explanation for this discrepancy lies in the accuracy of the sample position. In our measurements, the angular position was constant within 0.02° , whilst in the work of Ast and Höchst, the angular accuracy is not specified. At the Fermi level crossing, the dispersion of the hole pocket is unusually steep, so the angular position is important. The measurements are made on relatively small crystals which are heated and cooled over a large temperature range during the experiment, thus small variations in the angular position are likely unless great care is taken to avoid them.

Further evidence against a CDW is provided by the ARUPS measurements made in Dresden by Kim *et al.* and from low temperature STM and Transition Electron Microscopy (TEM) studies in the same work [3][III].

3.5 Conclusion

ARUPS is a very powerful tool in surface science. Not only does it allow the bulk and surface electronic structure to be measured, it also allows interesting properties such as the electron-phonon coupling (which has important

implications for the surface conductivity) to be probed.

In this chapter, measurements of the Bi(111) surface were presented. From these measurements we can conclude:

By considering the spin-split nature of the surface, and by making careful measurements of the Fermi level crossing, it is possible to exclude the existence of the charge density wave which has been proposed [23] for this surface.

The electron-phonon mass enhancement parameter has been calculated. In the work of Ast and Höchst [24], this has not been straightforward to extract since they rely on being able to measure very small changes in the real part of the self energy close to the Fermi level. However, by considering the temperature dependent MDC linewidth, we estimate the mass enhancement parameter to be $\lambda = 0.40 \pm 0.05$. This is much smaller than the value of $\lambda = 2.3 \pm 0.2$ reported in reference [24].

Chapter 4

Transport Measurements

4.1 Multi-Point Probe Measurements

4.1.1 Introduction

As described previously, the transport properties, especially the conductivity, of surfaces and nano-structures are of increasing significance as device sizes are reduced. Also, the quasi two dimensional situation at the surface opens the possibility to study interesting fundamental physical concepts. Therefore, a need for surface sensitive conductivity measurements arises.

Although there is great interest in surface conductivity, there is a surprising lack of progress in this field. This is attributed to the practical difficulties associated with such measurements.

In this chapter, details of the 4 point probe instrument are discussed. This includes a discussion of the theory and practical details, as well the presentation of the measurements made on silicon surfaces and the models required for interpreting them.

4.1.2 Theory

4.1.2.1 Why Use Multi-Point Probes?

The conductivity of a material can be measured by passing a current through the surface and measuring the potential drop across the surface. Perhaps the simplest way to do this is with two probes connected to a multi-meter.

Although such a measurement is very simple, there is an inherent problem with contact resistances. For example, consider a metal probe in contact with a semiconductor surface; such a system may give rise to a Schottky barrier with a large, non-ohmic contact resistance. This contact resistance is commonly sufficiently large to dominate the measurement, and thus it is not possible to

accurately estimate the resistance of the sample. Furthermore, when probes with a small contact area are used, this problem is exacerbated. This problem also becomes apparent in measurements of superconducting materials.

In principle, it is still possible to use such an instrument, since the contact resistances can be estimated (for example by measuring between each probe and a large contact on the back of the substrate), but this is rarely successful in practice since the resulting uncertainty in the surface resistance can be very large.

A more satisfactory solution to this problem is to use more than 2 probes. For example, by using 4 probes, the potential can be measured through probes which do not carry any current, thus the measurement becomes independent of the contact resistances. This technique is explained briefly below, and in more detail by Smits and Valdes: [60, 61].

Although 4 point probes have not yet been used extensively in surface science, they have important uses elsewhere. Principally, they are used for measuring the properties of bulk semiconductors, but they are also used on a larger scale in earth science, for example for finding groundwater.

Consider 4 co-linear probes with a constant current passed through two of the probes (usually the outer two). This constant current is independent of the contact resistance. It causes a potential drop across the sample, and thus the middle two probes have a potential difference across them. If one can measure this potential difference without drawing any current, then there will be no potential drop across the contacts, and thus the measured potential is also independent of the contact resistances. This is illustrated in figure 4.1

It is possible to measure the potentials of the inner two probes without drawing any current by employing a "null" method - i.e. instead of connecting the inner probes to a voltmeter (as in the figure), they are instead connected to a variable potential source through an ammeter. The potential is then adjusted such that no current flows, and thus the supplied potential is equal to the potential drop across the surface. However, it is more usual to measure the potential drop across the inner two probes using a voltmeter with an impedance that is significantly higher than the sample and contact resistances, thus the potential drop over the contacts is insignificant.

In the above discussion, the term "sample resistance" is used. This is a rather general term since it depends on both the surface and bulk resistivities. This is quite a complex issue and it will be dealt with more fully in a later section. However, a simplified approach is shown below for two extreme cases; that is a) when only an isotropic, homogenous bulk resistivity is considered, and b) when only an isotropic, homogenous surface resistivity is considered. These two situations are important to consider because com-

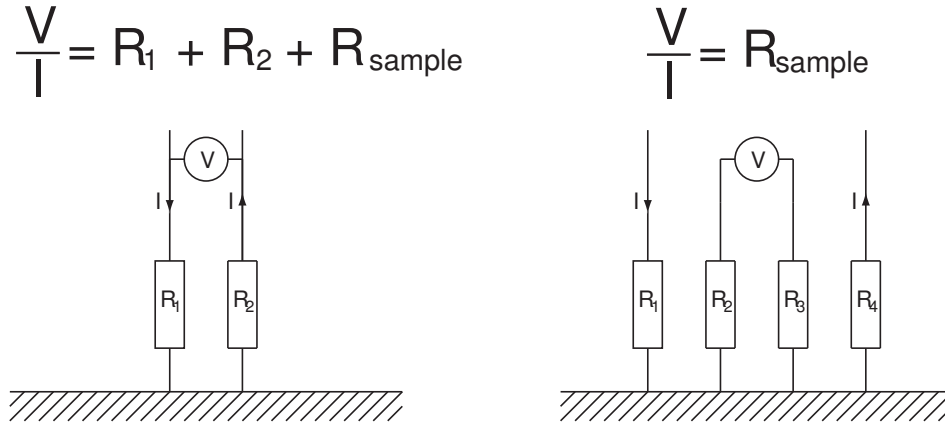


Figure 4.1: Figure to illustrate the need for four point probes. Using a two point probe (left-hand side), it is impossible to separate the sample resistance from the contact resistances R_1 and R_2 . However, using a four point probe (right-hand side), the potential can be measured across probes which do not carry any current, thus the measurement is independent of the contact resistances R_1 to R_4 . This is especially important on semiconductor surfaces since the contact resistances are large and non-ohmic.

monly the measured resistance is dominated by one term only, and thus these approximations can be used, furthermore, they represent situations for which analytical solutions exist. In most "real" situations, a numerical solution is required.

4.1.2.2 The Surface Solution

First, consider the case of an infinite 2 dimensional sheet. The electrostatic potential is given by Laplace's equation:

$$\nabla \left(\frac{1}{\rho} \cdot \nabla \Phi \right) = 0, \quad (4.1)$$

where Φ is the potential and ρ is the resistivity. Since the resistivity is the same across the entire sheet, or, in other words, since $\nabla \rho = 0$, the resistance can be removed from equation 4.1. Thus it can be expressed, in circular coordinates, as:

$$\frac{1}{r} \frac{\partial}{\partial r} \left(r \frac{\partial \Phi}{\partial r} \right) + \frac{1}{r^2} \frac{\partial^2 \Phi}{\partial \theta^2} = 0, \quad (4.2)$$

For a single point source there is no angular dependence, and thus the two dimensional solution is:

$$\Phi(\mathbf{r}) = -A \ln(|\mathbf{r} - \mathbf{r}_0|) \quad (4.3)$$

The constant A can be found from the boundary condition:

$$\oint \mathbf{n} \bullet \left(\frac{\nabla \Phi}{\rho_s} \right) dl = I, \quad (4.4)$$

where ρ_s is the surface resistivity and \mathbf{n} is the unit vector normal to the path. By evaluating this integral along a circular path centred on the source, the constant is found to be:

$$A = \frac{I\rho_s}{2\pi}. \quad (4.5)$$

and thus the potential can be written as:

$$\Phi(\mathbf{r}) = \frac{-I}{2\pi\sigma_s} \ln(|\mathbf{r} - \mathbf{r}_0|). \quad (4.6)$$

where σ_s is the sheet conductivity.

In a real measurement, both of the current carrying probes give rise to a similar potential. Using the principle of superposition, the measured potential at the inner probe positions is found to be simply the sum of the two individual solutions.

Therefore, in a normal 4 point probe measurement (in which a current is passed through the outer two probes and the potential drop across the inner two probes is measured) the four point probe resistance due to the surface is given as:

$$R^{4pp} = \frac{V}{I} = \frac{\ln 2}{\pi} \rho_s = \frac{\ln 2}{\pi\sigma_s} \quad (4.7)$$

for an infinite sheet with sheet resistivity ρ_s , or sheet conductivity σ_s .

4.1.2.3 The Bulk Solution

For a semi-infinite bulk of homogenous resistivity ρ_b , equation 4.1 can be written as:

$$\frac{1}{r} \frac{\partial}{\partial r} \left(r \frac{\partial \Phi}{\partial r} \right) + \frac{1}{r^2} \frac{\partial^2 \Phi}{\partial \theta^2} + \frac{\partial^2 \Phi}{\partial z^2} = 0, \quad (4.8)$$

Which can be solved for a point source to yield the following expression for the potential:

$$\Phi(\mathbf{r}) = \frac{I\rho}{2\pi} \frac{1}{|\mathbf{r} - \mathbf{r}_0|} \quad (4.9)$$

Thus for the standard 4 point probe measurement, the component of the resistance due to the bulk becomes:

$$R^{4pp} = \frac{1}{2\pi} \rho_b \frac{1}{s} = \frac{1}{2\pi s \sigma_b} \quad (4.10)$$

where s is the spacing between adjacent probes and σ_b is the bulk conductivity.

Many real systems cannot be simply approximated by an isotropic infinite sheet or a semi-infinite bulk, and therefore a more complex model is required. However, the above simplifications are still of much use, for example in determining suitable probe spacings (see following section).

4.1.2.4 Selecting an appropriate probe spacing

From the previous sections, it can be seen that in the simple 2D case, the measured 4 point probe resistance is independent of the probe spacing (s), and in the 3D case, the measured resistance is inversely proportional to the probe spacing. These results may seem a little surprising at first, but they can easily be understood intuitively by considering the path that the current takes between the outer two probes. One could suppose that the current primarily takes the shortest path, and that there is some "spreading" relative to this path. One could also suppose that this spreading is proportional to the path length, thus both the path length and "width" are proportional to the probe spacing s . Therefore in the 2D case,

$$R(4pp) \propto \text{length/width} \propto s/s \propto \text{constant}, \quad (4.11)$$

whereas in the 3D case

$$R(4pp) \propto \text{length/area} \propto s/s^2 \propto 1/s. \quad (4.12)$$

This supposition can be taken a step further; consider now that the sample consists of a 2D infinite surface on top of a 3D semi-infinite bulk. The current will predominantly take the path of least resistance, thus with larger spacings, the $1/s$ dependence of the bulk resistance will cause the current to prefer the path through the bulk whereas with small probe spacings the bulk resistance becomes too high and the current is confined to the surface. The "critical spacing" (i.e. the spacing at which the surface and bulk appear equally resistant) can then be found from considering the equality of equations 4.7 and 4.10:

$$s_{critical} = \frac{\rho_b}{2\rho_s \ln 2} \quad (4.13)$$

where ρ_b and ρ_s are the bulk and surface resistivities respectively. Since the surface resistivity may not be known, it is advantageous to be able to change the probe spacing.

Perhaps the ultimate solution is to have probes which can be independently positioned on the surface, such as the commercial system made by Omicron GmbH, which is based of 4 independent STM systems. Using a 4-STM system, Shiraki *et al.* [62] measured the resistance of a Si(111)(7×7) sample, and found that for probe spacings greater then 10 μm , the measurement agrees with the predicted bulk resistivity, whereas at smaller spacings a higher resistance is measured (see figure 4.2).

Although the 4-STM has the clear advantage of variable probe spacing, it has some limitations. Reliability is certainly an issue since it is necessary to have 4 fully functional STM in the same chamber in order to make a measurement. Also, there are some limitations on the probe spacing; in figure 4.2, the smallest achievable spacing is 1 μm and this makes it impossible to judge whether the conduction is purely through the surface or not.

It should be noted that the previous discussion was based on the assumption that the sample can be modeled as the combination of an infinite 2D sheet and a semi-infinite 3D bulk. For semiconductor surfaces, this assumption no longer holds since one also has to consider the affect of the space charge layer (this is discussed in more detail in section 4.3.2.2).

To summarise, the required probe spacing for a surface sensitive four point probe measurement depends on the ratio of the surface and bulk conductivities. For a simple 2D/3D system, the required probe spacing can be estimated from equation 4.13, however in many cases, the surface resistivity is not known, and the simple 2D/3D model may not apply, therefore it is advantageous to be able to change the probe spacing.

4.1.3 Experimental Setup

The initial experimental setup was constructed at the Technical University of Denmark by T.M. Hansen. A detailed description of the setup can be found in ref [63]. The system basically consists of a platform inside a UHV chamber. A sample stage is mounted on the platform which can be cooled using a Helium or Nitrogen cryostat. The probe is mounted on a cantilever arm above the sample which can be maneuvered using 3 piezo motors. The setup is illustrated in figure 4.3

Many major changes have been made to the setup during this project. The most significant changes are described in the following sections.

4.1.3.1 Minimising the "Downtime"

Since the 4 point probe system is constantly under development it is necessary to vent and open the chamber quite frequently, therefore it was considered

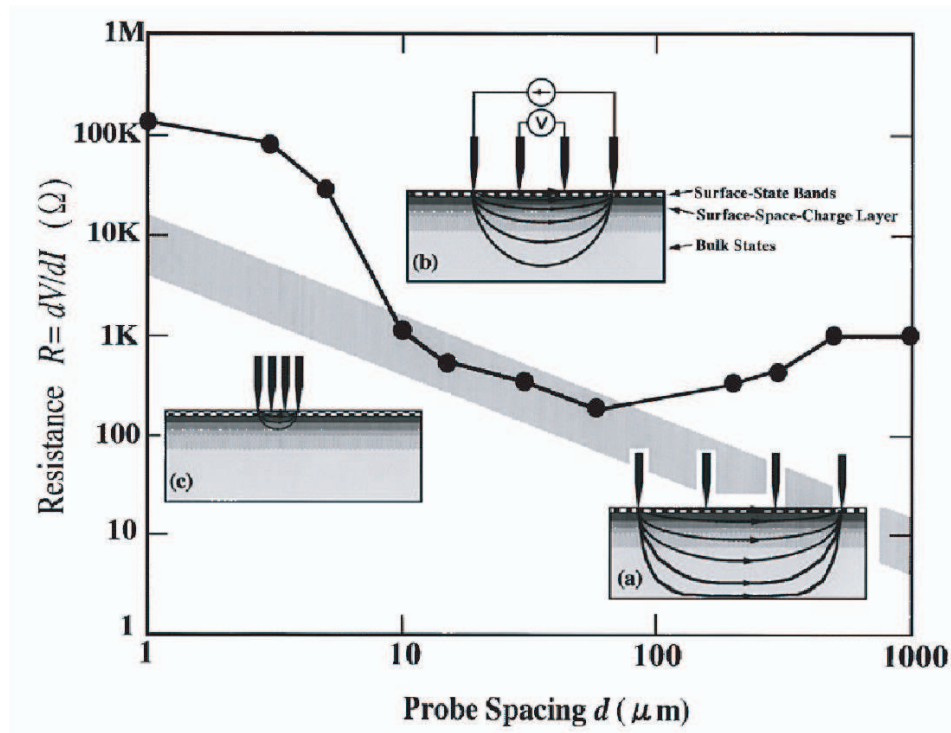


Figure 4.2: Room temperature 4 point probe measurements of the Si(111)(7 \times 7) surface. The measurements (depicted by markers and a solid line) are made using a 4 point probe with variable spacing. For intermediate spacings, the measured resistance agrees well with the expected bulk component (shaded area) but for smaller spacings, this is not the case (from ref: [62]). The insets show the path of the current for (a) large, (b) intermediate and (c) small probe spacings.

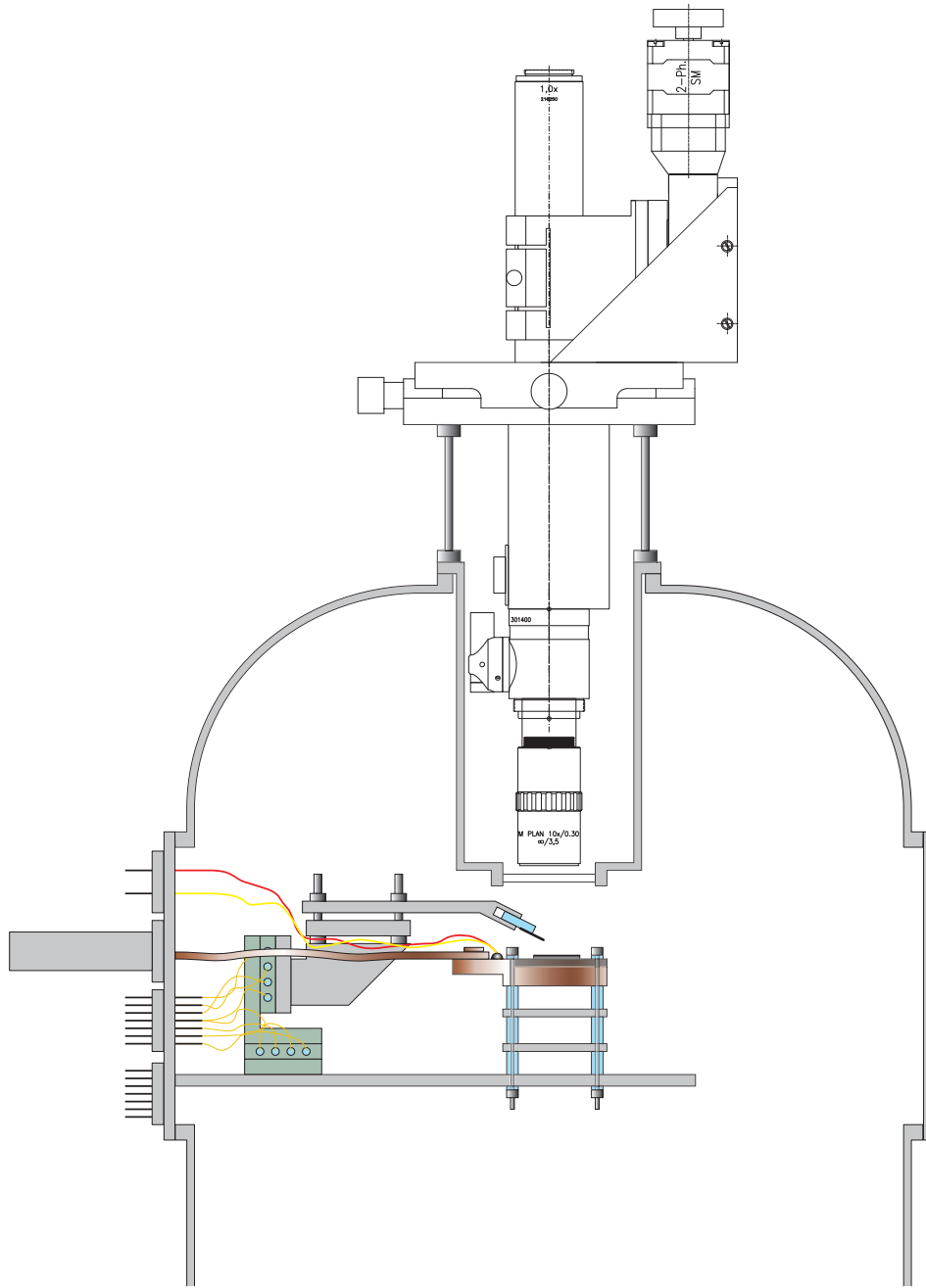


Figure 4.3: Schematic figure depicting the current experimental setup. An optical microscope mounted in a recessed viewport allows the probe and sample surface to be seen. The probe is supported by a cantilever arm which can be moved in 3 axes with nanometer precision by means of piezo motors.

important to minimise the downtime of the system:

Firstly, the pumping efficiency was improved; the turbo-molecular pump was mounted directly onto the chamber through a maximum diameter CF40 gate-valve, instead of via a long bellows and a standard 90° valve. Whilst this affords a greater pumping efficiency, the disadvantage is that vibrations from the turbo pump are transmitted to the chamber, thus it is necessary to switch off the turbo pump whilst measuring. A larger capacity rotary pump was used to improve the backing vacuum for the turbo pump. A valve and a Pirani vacuum gauge were added between the rotary and turbo pumps. The gauge allows the backing pressure to be monitored, and the valve allows the rotary pump to be isolated from the turbo so that it can be switched off without venting (this also required a manual override of the automatic vent valve).

An additional valve that could be connected to a liquid nitrogen suck-up tube was also added which allows the chamber to be vented with a minimal intake of water vapour.

A set of new filaments was added to the titanium sublimation pump (TSP). In addition to this, a problem was discovered with the TSP controller; poor connections to the high current terminals had resulted in severe oxidation to the terminals and the controller was unable to supply sufficient current to the titanium filaments. The controller was repaired by replacing the terminals with brass bolts, and in combination with the new filaments, a noticeably increased pumping efficiency was achieved.

The ion-pump controller was found to suffer with an intermittent fault, whilst this was being investigated, a temporary system was set-up to allow a standard Varian ion-pump controller to be used instead.

The bake-out system was also improved; a permanent frame was built over the chamber. The frame supports two 1800 W infra-red heaters as well as the bakeout tent. The roof of the tent is permanently kept in position, whilst the sides are lowered only when required. The power of the heater was selected such that they heat the chamber to ≈ 120 °C, thus eliminating the need for a control feedback. However, several thermocouples are connected to the chamber (both inside and outside) to allow the temperature to be checked. The temperatures recorded by the thermocouples can be monitored and the bakeout heater can be controlled remotely.

Finally, all of the connections to the probe, motors, sample and preparations stages were made using a single CF150 flange, and a mechanical mounting guide was constructed. This allows the entire system to be easily removed and replaced for repairs and maintenance.

4.1.3.2 Sample Cooling

Another major development has been the sample cooling. In the original setup, the sample temperature was never directly measured, but was instead estimated from considerations of cryostat power, thermal losses and so forth.

In order to confirm this estimate, a thermocouple was attached directly to the sample stage, and it was discovered that the sample temperature estimate was rather inaccurate. According to ref. [63], the lowest achievable temperature was around 90 K. In fact it was measured to be 175 K.

After much investigation, this discrepancy was found to be due to a number of reasons; the elaborate thermal shield was not working effectively, the sample stage was not sufficiently well insulated from the surroundings, and the sample stage itself was not conducting as well as expected. In order to solve these problems, the sample stage was redesigned, and manufactured from oxygen free copper. Similarly, the copper braid was replaced with more substantial braids, also of oxygen free copper. The sample insulation was improved and the thermal shield was removed. After making these modifications, sample temperatures of 95 K could be reached using liquid nitrogen.

4.1.3.3 Sample Stability

Whilst improving the sample cooling, it became apparent that thermal expansions within the sample and sample stage could be significant. The sample stage is made of copper which has a thermal expansion coefficient of $16.5 \times 10^{-6} \text{ K}^{-1}$ [64], therefore, a sample stage that is 10 mm thick will contract by 50 μm when cooled by 200 K. Since the probes used have a typical length of 10 μm , this presents quite a problem. A more subtle problem also exists; if the sample stage is heated or cooled unevenly, then uneven thermal expansion can result in a horizontal movement of the sample.

Several steps were taken to reduce these problems; the sample stage is supported at the same height as the sample surface, thus if the sample stage cools evenly there will be no change in sample height due to expansions within the sample stage. Also, the sample stage is supported by 4 legs which are insulated in 3 stages in an attempt to make them insulate equally. However, when using smaller probes, it was found that the sample position was not sufficiently stable thus the probe had to be moved to a safe height above the surface until thermal equilibrium was reached.

Whilst measuring, vibrational stability is also important. The sample measuring stage is mounted to the feedthrough as rigidly as possible, and the chamber is mounted on pneumatic supports to reduce the transmission of vibrations from the surroundings. However, this does not eliminate vibrations

from equipment that is in physical contact with the chamber, for example the mechanical pumps. Therefore, during measurements, the rotary and turbo pumps are switched off, as well as the cooling fans for the pumps. The cryostat pump is also a source of vibrations, but this cannot be switched off during low-temperature measurements - therefore the pump is connected to the nitrogen reservoir through a long flexible pipe.

4.1.3.4 The Sample Stages and Transfer

It is necessary to be able to transfer samples between several stages in the chamber. The stages include the measuring stage, the cleaning stage, the LEED measuring stage and an additional storage stage.

In order to transfer samples, some sort of sample holder and transfer mechanism is required. In the initial setup, only semiconductor samples were used. Such samples were cleaned simply by passing a current through the sample. In the case of silicon, a temperature of around 1250 °C is required, and this typically requires ≈ 10 A. Therefore, the sample is held in the sample holder such that one end of the sample is grounded whilst the other end it attached by means of a sliding contact to a high current electrical feedthrough. The sample cleaning stage is mounted in front of a clean CF40 viewport so that the sample temperature can be estimated using a pyrometer. In order to measure on other samples - such as bismuth - not only does the sample holder have to be physically different in order to accommodate the crystal, but also the sample cannot be heated with a direct current, so instead a filament heater is used. Therefore an entirely different sample holder and sample cleaning stage is used; the sample cleaning stage is attached with just two bolts so that it is a relatively simple operation to swap between the direct current heating and filament heating stages. Additionally, the filament heater stage has a K-type thermocouple connector so that a thermocouple mounted on the sample is connected to a feedthrough when the sample is in place. A sputter gun is mounted such that samples can be sputtered when in the sample heating stage.

The LEED sample stage is significantly simpler. It is permanently grounded and at the same height as the LEED electron gun. However, the horizontal distance and angle need to be adjustable since the required LEED position is out of reach of the sample manipulator. In order to achieve this, the LEED sample stage is loosely attached to its support through an elongated hole. The manipulator can then be used to change the position and angle of the sample stage. Since two different sample holder designs are used, two different LEED sample stages are required. As with the cleaning stages, it is a relatively simple operation to swap between them.

The storage stage is simply a copy of the LEED stage mounted horizontally. Its only purpose is to hold a sample whilst it is not in use. Again, there are two versions of the sample holder stage to accommodate the two different sample holder types, but it is possible to use either sample holder in each stage (although a mismatching sample holder is held less securely).

The measuring stage consists of a copper block which is attached with a copper braid to the cryostat. It also houses a thermocouple so that the sample temperature can be measured. Since vibrations of the sample would cause damage to the probe, it is necessary that the sample holders are securely held in the measuring stage. This is achieved by milling two slots in the copper block to receive the sample holders; the slots are milled to be slightly oversized and then fitted with molybdenum springs which act to firmly push the sample holder against the upper edge of the slots. These slots are milled with sufficient tolerance for either sample holder type to be accommodated.

The original sample manipulator has been replaced since it was damaged and difficult to operate. A new manipulator was custom made and incorporated some improvements in the design: It has a magnetic coupling which allows improved force feedback, and has jaws which are designed to grab the sample such that it can move by $\pm 5^\circ$ in both planes. It has a longer reach and smaller angular range; thus it is mounted further from the sample stages and makes the sample transfer easier. After some initial difficulties with the jaw mechanism, the new manipulator was found to be a great improvement.

4.1.3.5 Probe Handling

The system has been set-up to allow a range of probe spacings to be handled. The initial setup was limited to probe spacings larger than $\approx 10 \mu\text{m}$, but this has now been improved so that probes as small as $1 \mu\text{m}$ can be used. The system has also been upgraded to allow 12 point probes to be accommodated.

The major limitation in the original setup was the optical microscope, so a higher performance microscope was acquired. The new microscope has a resolution of around 500 nm at a distance of 35 mm from the objective lens. This objective distance is significantly shorter than the original microscope, and thus the recessed microscope viewport had to be modified to accommodate the new microscope. One of the consequences of this modification was that the height between the sample and the microscope window inside the chamber was reduced, thus the cantilever arm which holds the probe had to be rebuilt so that it required less vertical space. The result was that the new microscope could be accommodated, but with very little spare space; the objective lens is approximately 0.3 mm from the viewport glass, and the probe cantilever arm has about 1.0 mm adjustment between touching the window and touching the

sample.

The new microscope required the window recess to be machined out to a larger diameter and the microscope was custom made to require the minimum dimensions. Thus, the microscope has ≈ 3 mm of lateral adjustment.

The lateral and vertical positioning of the microscope was modified to be more repeatable since the original setup was time consuming to align. This was achieved by constructing a microscope support that could be attached to the chamber in a repeatable manner and would support an x- and y- translation table. Zoom and focus positioning was achieved by encoded stepper motors and a limit switch was also set to stop the objective lens colliding with the window. The microscope camera and motors were controlled using custom made software.

In order to accommodate 12 point probes, a new probe holder and additional electrical connections had to be constructed. Since no suitable flanges were available, multiple connections were made through one CF16 flange, by means of a custom made adaptor.

The original 4 point probe holder was machined from "Macor" and aluminium which are both vacuum compatible. However, the electrical connections often failed so it was deemed impractical to extend the design to accommodate 12 connections. Instead, the commercial 12 point probe holders developed by Capres A/S for use in air were used. Since they are made of unknown materials, their vacuum compatibility was tested by placing one in the vacuum chamber with a Residual Gas Analyser (RGA). The total pressure at room temperature was normal, but increased drastically during baking. However, after gentle baking at ≈ 100 °C vacuum of $\approx 5 \times 10^{-10}$ torr was achieved with no abnormal gas residuals. The electrical connections to the probe holder were made by flux free soldering (performed by GPV A/S). A new cantilever arm had to be fabricated to accommodate the new probe holder.

Another concern with 12 point probes, and the smaller 4 point probes is that since the probe length is disproportionately reduced compared with the probe spacing, the probes are only able to tolerate a small angular misalignment. Since it is difficult to mount small samples accurately, some sort of angular adjustment is needed. In the present setup, this adjustment is made when the probe chamber is opened to air, but it would be advantageous to be able to make adjustments under vacuum.

4.1.3.6 Data Acquisition and Analysis

In the initial setup, a LabView program was used to control the cryostat and 4 point probe measurement. The Digital to Analogue Converter (DAC) provides a linearly ramped potential to the electronics, this is then converted

into a linear current ramp by a programmable-gain amplifier. Currents from <1 nA to $100 \mu\text{A}$ can be produced. This current can then be supplied to any probe, or the sample substrate, by means of programmable multiplexers. Similarly, any two probes (or the substrate) can be connected by multiplexers through programmable-gain amplifiers to the Analogue to Digital Converter (ADC). This allows potentials from 0.1 mV to 10 V to be measured. All of the signals are passed through optical decouplers and the electronics use noiseless battery power.

The LabView software sends digital signals to program the multiplexers and amplifiers, as well as producing a ramped voltage to the current amplifier. It reads the potential from the ADC so that a current-versus-potential (a so called I-V) plot can be displayed. Also, the sampling number, a delay time and the number of repeat scans can be set such that the required signal to noise ratio can be achieved. After every positive current ramp, a negative ramp is produced and the measurement is repeated in the opposite sense, so that any charging of capacitative problems become apparent. The same LabView program can also control the cryostat.

Several modifications were made to the above system: For example, the software was modified so that the data analysis could be carried out more efficiently. The multiplexers were found to be unreliable, so a manually switched override and simple test systems were made. The switches were also extended for 12 point probes.

A more efficient cryostat control was also developed.

4.1.3.7 Repairs and Maintenance

During the course of this project, many repairs were required. Perhaps the most significant was the independent failure of the three piezo motors which control the position of the probe. The entire sample platform is built around the motor dimensions, and since these motors are no longer manufactured, replacing them would require much of the sample platform to be rebuilt. Fortunately, the motors could be reconditioned.

4.2 Measurements of Si(111)

4.2.1 Introduction

In this section, the initial measurements made with the micro 4 point probe are reported. Since this is a relatively new instrument, it seems logical to make initial measurements on a well studied surface. However, surface conductivity measurements are relatively rare, and thus those which have been made appear to create as many questions as they answer.

In particular, the Si(111)(7×7) surface is considered. This surface has been extensively studied in recent decades, but the question of whether or not it is "metallic" has still not been satisfactorily answered. What is meant by "metallic" is also the subject of some debate; whilst some authors define a metal as being a good conductor, other definite it as having $d\sigma/dT > 0$, another definition is from an optical standpoint; metals are reflective since they contain free electrons which can screen out incident electromagnetic radiation. A more formal definition is that a metal has a nonzero density of states at the Fermi level. This matter will be discussed in more detail in the following section, and is also discussed in terms of conducting polymers in reference [65].

Several previous attempts to measure the conductivity of this surface have also been made, therefore this surface is chosen for the initial measurements with our instrument. Not only are there existing conductivity measurements (both with micro 4 point probes and with other techniques) with which to make a comparison, it is also an interesting "unsolved" case.

As well as measurements of Si(111)(7×7) surfaces, measurements of Si(111)+Ag are reported as a comparison. Both measurements of the ordered Si(111)+($\sqrt{3} \times \sqrt{3}$)Ag and disordered Si(111)+Ag films are reported, as well as a brief study of stepped silicon surfaces.

4.2.1.1 Units and Definitions

The terms used in the following sections are sometimes the source of some confusion. Therefore a brief clarification is needed:

The *Conductance* (C) of the sample does not need much clarification. It is the quantity that is found from the gradient of the I-V measurements since $C = dI/dV$. In this work, it is quoted using the S.I. units of reciprocal ohms (Ω^{-1}). In other work it is sometimes quoted as amperes per volt (A/V) or siemens (S).

The relationship between the conductance and the *conductivity* (σ) depends on the dimensionality of the system. For a 3D system (such as the bulk

case), the relationship is:

$$C = \sigma_b \frac{A}{l} \quad (4.14)$$

where σ_b is the bulk conductivity, A is the cross sectional area and l is the length. Using the S.I. system, area has units of m^2 and length has the units of m , thus the conductivity has units of $\Omega^{-1}\text{m}^{-1}$.

For a 2D system (such as the surface case), the relationship is:

$$C = \sigma_s \frac{w}{l} \quad (4.15)$$

where σ_s is the surface conductivity, w is the sample width and l is the length. Since w and l both have units of m , σ_s simply has units of Ω^{-1} and thus the conductance and the surface conductivity have the same units. Since this can be a little confusing, it is common to see the surface conductivity written in units of $\Omega^{-1}\text{m}/\text{m}$ or " Ω^{-1} per square". In this work, the S.I. units of Ω^{-1} are adhered to.

Resistance is simply the reciprocal of *conductance*, and *resistivity* is simply the reciprocal of *conductivity*. Thus the 2D resistivity has the same units as resistance (Ω), whilst the 3D resistivity has S.I. units of Ωm . However, it is common to see the 3D resistivity quoted using the c.g.s units of Ωcm .

4.2.1.2 Si(111)(7×7)

Si(111)(7×7) is perhaps one of the most studied surfaces. Its unusual geometric structure has been studied by many techniques [66–73]. In short, the geometric structure is generally accepted to be that proposed by Takayanagi *et al.* [74]; a structure which leaves only 19 of the original 49 dangling bonds per (7×7) unit cell. The geometric structure is shown in figure 4.4.

The electronic structure has also been extensively studied: From a theoretical viewpoint, it is possible to calculate the electronic structure since the atomic arrangement is known. However, since this surface has a rather complex geometric structure, such a calculation is not a simple task. Thus calculations suggest a wide range of possibilities; from a localised orbital picture to a delocalised band picture [75–83].

Since the unit cell is accepted as having an uneven number of electrons, electron counting arguments all lead to the picture of at least one half filled band, and thus one would expect the surface to be "metallic", unless it is too highly correlated.

Indeed, from Takayanagi *et al.* [74] we see that most of the bonding electrons are placed in filled bands, and thus only 5 electrons per unit cell (located at the ad-atom sites) account for the electronic structure close to the

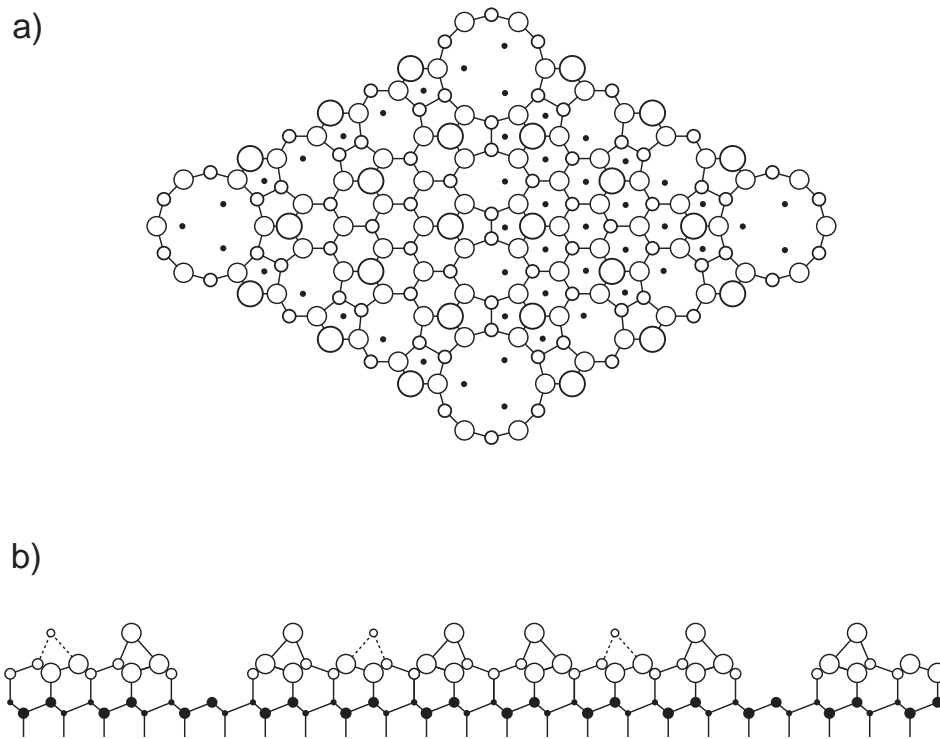


Figure 4.4: Model of the $\text{Si}(111)(7 \times 7)$ surface reconstruction from Ref. [74]. (a) Top view: Atoms at decreasing heights are indicated by circles of decreasing size. Filled circles represent atoms in the non-reconstructed layers, and empty circles represent the reconstructed atom positions. (b) Side view: Again, the filled circles show the non-reconstructed atom positions, and the empty circles show the reconstructed positions. Larger circle represent atoms on the $(\bar{1}01)$ plane and smaller circle represent atoms in the next (101) plane.

Fermi level and this gives rise to a "metallic" surface. However, it is plausible that the surface electronic structure is that of a correlated metal [84, 85] and if the correlations are sufficiently strong this would give rise to a Mott-Hubbard insulator transition [85].

From an experimental viewpoint, the situation is not so complex. Photoemission measurements show two weakly dispersing surface states at around 0.2 eV and 0.9 eV below the Fermi level and a back-bonded state at 1.8 eV below the Fermi level [86–97]. By scanning tunneling spectroscopy, the surface state at 0.2 eV is assigned to the adatoms, and the surface state at 0.9 eV is assigned to the rest atoms [98, 99]. The unoccupied states have been studied with IPES [100–102] and the transitions between the occupied and unoccupied states have been studied by Electron Energy Loss Spectroscopy (EELS) [103–105].

To summarise, experimental techniques such as Photoemission, IPES and EELS give indications that the Si(111)(7×7) surface is "metallic". Photoemission studies show intensity all the way up to the Fermi level and EELS measurements show an asymmetric loss line which is characteristic of the infinitesimal transitions that occur across a metallic Fermi level. At lower temperatures, the situation is not quite so clear; below 100 K, EELS measurements show a sharpening of the loss features which can be interpreted as a gap opening. Similarly, surface-sensitive Nuclear Magnetic Resonance (NMR) measurements [106, 107] are indicative of a Mott-Hubbard metal-insulator transition at low temperatures.

The conductivity of the Si(111)(7×7) surface has also been studied by a variety of techniques, and the results differ by many orders of magnitude: First, the AC conductivity can be estimated from EELS measurements; this gives the surface conductivity as being of the order of $10^{-5} \Omega^{-1}$ [108]. The conductivity can also be estimated by using a STM tip as a "Spreading Resistance Probe"; a simple picture of this technique is that the probe is contacted with the surface, and the resistance between the probe and the back of the sample can be measured. The probe is then dragged around on the surface to form a trench that encloses a small square. The probe is then contacted with the centre of the square, and the resistance measurement is repeated. It is assumed that the difference between in the measured resistances is due to the restriction of the surface currents in the latter measurement. Using this technique, the surface conductance of the Si(111)(7×7) surface is estimated as $8.7 \times 10^{-9} \Omega^{-1}$ [109]. Using a similar method, Y. Hasegawa *et al.* find values for the surface conductance in the range 10^{-6} to $10^{-10} \Omega^{-1}$ [110]. Perhaps the most elegant method - that of using 4 independent STMs to make a variable spacing 4 point probe measurement - suggests that the surface conductivity

is less than $10^{-5} \Omega^{-1}$ [62]. Macroscopic 4 point probes are used to measure the conductivity of a thin film of Si(111)(7×7) on an insulating substrate, and from this, the surface conductivity is estimated at $10^{-4} \Omega^{-1}$ [111]. Finally, micro 4 point probe measurements by S. Hasegawa *et al.* yield a surface conductivity of 10^{-5} to $10^{-7} \Omega^{-1}$ at room temperature, and surprisingly, it is found to depend on the bulk doping [112, 113]. The temperature dependence of the surface conductivity is described as "nonmetallic" [113].

Therefore, despite much effort and many significant contributions, the nature of the Si(111)(7×7) surface is still debated. Conductivity measurements are far from being consistent and yield values of the surface conductivity in the range $10^{-10} \Omega^{-1}$ to $10^{-4} \Omega^{-1}$. An attempt to finally solve this issue is needed.

Before presenting the results from our 4 point probe measurements, some possible reasons for the above discrepancies should be considered:

First, it is important to understand what is really meant by the term "metallic" in terms of the properties of a surface. In very general terms, a metal can be defined as "a lattice of positive ions surrounded by a cloud of delocalised electrons". More specifically, metals are often defined as having "a continuous density of states at the Fermi level", or as having "overlapping conductance and valence bands" [114]. Because of these properties, metals tend to have a high conductivity, and thus the term "metal" has become synonymous with having good conductive properties - although this need not always be the case. Now let us consider the properties of a surface; generally the above definitions of a metal can still be applied, but this does not implicitly mean that the surface will be a good conductor. This point is frequently overlooked, and thus when a poor surface conductivity is measured, it may be reported that the surface is "non-metallic". In fact, it is difficult to relate the electronic properties of the surface states with their expected transport properties since many other factors may play a more significant role than one finds in the bulk. In particular, the carrier mobility and density may be very different on the surface compared with the bulk. Another source of confusion is the temperature dependence of the conductivity; it is sometimes reported that a surface is "non-metallic" simply on the grounds that the conductivity increases with temperature [113], but, as it will be shown in section 4.3.3.1, the character of the surface cannot be so simply inferred.

Secondly, it is necessary to consider what is meant by "surface conductivity" and "surface state conductivity". In the case of semiconductors, it is possible for the pinning of the Fermi level at the surface to be significantly different from that of the bulk, and thus the possibility of a space charge layer close to the surface arises. The conductivity of the space charge layer may

differ significantly from the bulk and surface conductivities. It is therefore important to clarify whether the "surface" conductivity includes the conductivity of the space charge layer. If one refers only to the surface state conductivity, then one has to consider how this can be separated from conductivity of the space charge layer and the bulk.

The role of the space charge layer is not trivial since it depends on the bulk properties (such as the doping type and strength) as well as on environmental factors such as temperature and surface preparation. Therefore, in order to understand the role of the space charge layer, a model is required. This is described in detail in section 4.3.2.2. At this stage, it is sufficient to say that in the above reports, the "surface conductivity" is measured on a variety of substrates and with varying surface sensitivity, and the influence of the space charge layer is not always considered properly.

4.2.1.3 Si(111)($\sqrt{3} \times \sqrt{3}$)Ag

The Si(111)($\sqrt{3} \times \sqrt{3}$)Ag surface has also been extensively studied, and by all accounts is not nearly so controversial as that of Si(111)(7 \times 7). Some attempts at measuring the surface conductivity have also been made and therefore this surface is also an interesting test case for our instrument.

The geometric structure of the Si(111)($\sqrt{3} \times \sqrt{3}$)Ag surface has been studied by a large range of techniques over the last 30 years and is now quite well understood, although some controversy still remains. In early work, the "Honeycomb Chained Triangle" or HCT model was generally accepted; for example, see [115–117]. However, more recent studies suggest that the In-Equivalent Triangle or IET structure has a lower total energy [118, 119]. The IET and HCT structures are illustrated in figure 4.5. The existence of the IET structure has been confirmed experimentally by photoemission spectroscopy [120], X-ray diffraction [121] and Reflection High Energy Electron Diffraction (RHEED) [122]. However, some controversy remains since room temperature empty state STM images still resemble the HCT structure [123] whilst low temperature (6 K and 62 K) images are consistent with the IET structure [124]. There is more than one possible explanation for this apparent contradiction; whilst it has been suggested that displacive phase transition may occur [121], it is more generally believed that an order-disorder phase transition occurs. Thus, at higher temperatures a rapid switching between the two possible IET domains would result in slow techniques such as STM recording an averaged image that would closely resemble the HCT structure whereas at lower temperatures the IET fluctuations are frozen out. Although this dispute has not yet been settled, further evidence for the latter order-disorder transition is found by measuring with faster techniques such as photoemission, which shows the

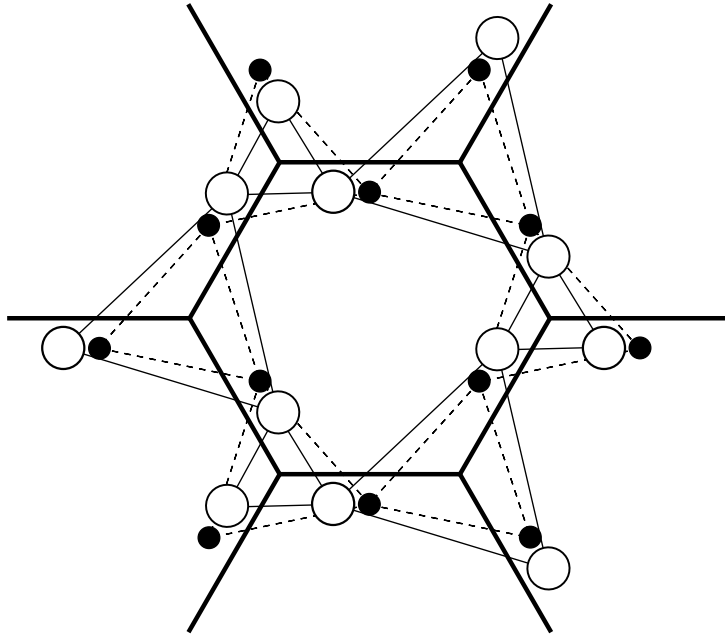


Figure 4.5: A comparison of the HCT structure (filled circles and dashed lines) and IET structure (empty circles and thin, solid lines). The thick, solid lines represent the unit cell boundaries. From ref. [119]

characteristic IET structure existing also at room temperature [125].

The electronic structure has also been well studied. Until recently, there has been some controversy over the nature of the $(\sqrt{3} \times \sqrt{3})\text{Ag}$ surface. Despite many photoemission and inverse-photoemission studies [126–133], STM [134–138] and optical [139] studies, the question of whether the surface is semiconducting or metallic was not conclusively answered. Furthermore, first principle calculations were also unable to provide an answer [140–142]. More recent photoelectron spectroscopy studies of the Fermi surface and silicon core levels indicate that exact monolayer coverages of $(\sqrt{3} \times \sqrt{3})\text{Ag}$ are semiconducting, but by increasing the Ag coverage by small fractions of a monolayer (Δ), the surface becomes metallic [143–145]. Thus, the pinning of the Fermi level at the surface also shows a strong dependence on the coverage [145].

Attempts have also been made to measure the conductivity of the $(\sqrt{3} \times \sqrt{3})\text{Ag}$ surface: Firstly, there is the macroscopic 4 point approach using the van der Pauw [146] method made by Schad *et al.* [147]. In their Rapid Communication, insufficient details are given to allow an actual value of the surface conductivity to be estimated, but this work does show that the conductivity is strongly dependent on the coverage, especially for coverages of $1 + \Delta$.

Nakajima *et al.* also attempted to measure the surface conductivity at similar coverages using a macroscopic 4 probe technique [131]. From this experiment, the conductivity is estimated as 1.5 to $2.3 \times 10^{-4} \Omega^{-1}$ for coverages of 1.00 to 1.09 monolayers. Finally, S. Hasegawa *et al.* measure the conductivity of a 1 monolayer coverage at room temperature using a micro 4 point probe, from this measurement, they estimate the conductivity to be $5 \times 10^{-4} \Omega^{-1}$ [148]

To summarise, the $(\sqrt{3} \times \sqrt{3})\text{Ag}$ surface is much less controversial than the clean (7×7) surface, and, the measured conductivity of the surface is less debated. However, this may simply be because fewer studies of the surface conductivity exist. Another consideration is that the conductivity is many orders of magnitude higher than the typical estimates for (7×7) , and thus it is easier to measure since it is less affected by other factors - such as the dynamics of the underlying space charge region. However, there are some additional sources for inconsistency that should be considered; for example it is accepted that the pinning of the Fermi level at the surface is strongly dependent on the Ag coverage, thus the conductivity of the space charge layer is also dependent on the coverage. This factor must also be considered when the coverage dependence of the conductivity is discussed, however it is neglected in reference [131]. Additionally, in a review of metal-semiconductor interfaces, Le Lay [149] reports that the $(\sqrt{3} \times \sqrt{3})\text{Ag}$ surface is very sensitive to the initial cleanliness of the Si(111) substrate, and to the Ag deposition. Finally, both a theoretical and an experimental study of the $(\sqrt{3} \times \sqrt{3})\text{Ag}$ surface proposes that the role of steps may also have a significant influence on the surface conductivity [150, 151].

4.2.1.4 Si(111) with Silver Islands

In the previous sections, the nature of the surfaces was the subject of some debate. Therefore, for the next test surface, an uncontroversial metallic surface is chosen; a disordered silver film.

The geometric arrangement of the surface is dependent on a number of factors: Principally, the temperature of the substrate during the growth and the film thickness, although the substrate preparation and step density could also be significant [152].

The growth of silver on silicon has been thoroughly studied. From such studies, a phase diagram has been constructed [153]. Photoelectron diffraction [154], RHEED [155, 156], STM studies [157–160] and optical studies [161] show that the room temperature growth mode is rather unique, but not dissimilar to Stranski-Krastanov growth: After the formation of a wetting layer, the silver nucleates into islands with a preferential height of around 5 monolayers.

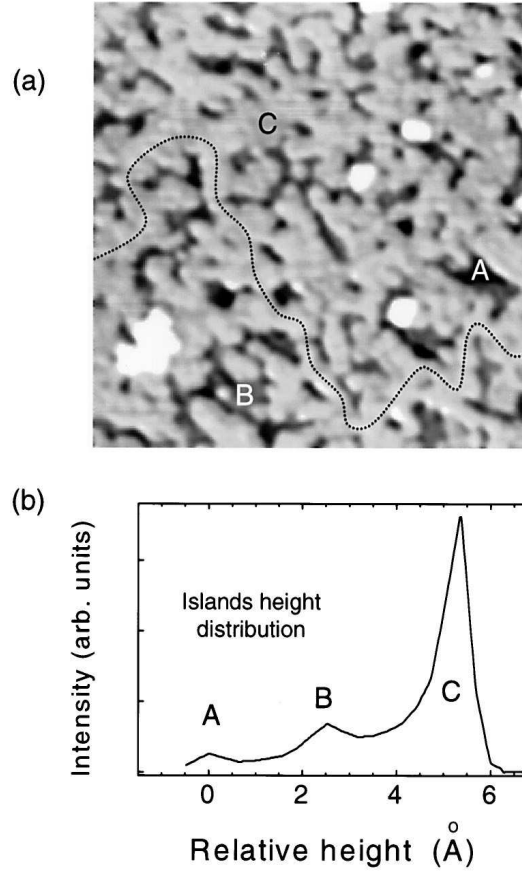


Figure 4.6: (a) A $100\text{ nm}\times 100\text{ nm}$ STM image of the Si(111) surface after the evaporation of a percolating network of Ag islands, and (b) the height distribution of the islands in the image showing the preferential heights (marked by A,B and C). From reference [158]

Further evaporation results in the islands spreading beyond the percolation threshold until a relatively uniform film is formed. Figure 4.6 shows an STM image and island height distribution of such a percolating network.

For very thin films and islands, the electronic properties are influenced by quantum size effects [147, 162–165]. Thicker films are expected to exhibit the properties of bulk silver [166].

The conductivity of such films has not been well studied. However, once the film has become thick enough to exhibit the bulk properties, it is straightforward to estimate the sheet conductivity of the film. For films of 1 monolayer and 2.2 monolayers, Gavioli *et al.* measure a significantly enhanced conductivity, relative to that of bulk silicon. However in their letter, insufficient detail is given to allow the sheet conductance to be estimated [158].

4.2.1.5 Vicinal Surfaces

From a practical viewpoint, it can be difficult to prepare large step-free domains on silicon surfaces. Therefore, it is probable that the measurements of surface conductance quoted in the previous subsections have been performed across steps. It is conceivable that surface steps could have a dramatic effect on the measured conductivity, and perhaps this could explain the enormous range of the reported surface conductivity of Si(111)(7×7). Therefore, it is of interest to measure the influence of steps on the conductivity of a surface.

The structure and growth of regular stepped silicon surfaces has recently become a subject of much interest. There are many reasons for this interest, but perhaps the most relevant to this work is that the regular terraces can be used as a template for growing 1 dimensional structures such a metallic nanowires, and thus allow some fundamental 1D concepts to be studied [167–170].

The geometric structure is dependent on the miscut angle. For larger angles (i.e. $\approx 1^\circ$ or more), the average step separation is relatively small; a miscut of 1° corresponds to an atomic step after every 60th surface atom. The length of the 7×7 unit cell (along its longest axis) is approximately 12 times the atomic spacing, so a 1° miscut corresponds to terraces with a width of around 5 unit cells. Thus one can see that the terraces may be forced to form with a periodicity that is commensurate with the surface reconstruction. An example of this is shown in figure 4.7; in this figure the miscut is approximately 3° and the terraces are seen to be commensurate with the 7×7 unit cell. When the angle of the miscut corresponds to an incommensurate periodicity, the terraces may become unequally spaced, or "bunched". In fact several other factors also affect the terrace size and step bunching; perhaps the most significant being the surface preparation [171, 172]. Structural techniques such as LEED allow the direction and size-distribution of steps to be estimated [173].

Some measurements of the conductivity of the vicinal Si(111)(7×7) surface are available; S. Hasegawa *et al.* report an increase of around a factor of 3 in the measured resistance of a vicinal Si(111)(7×7) surface when a micro 4 point probe is placed across large step bunches. A similar effect is seen on vicinal Si(111)($\sqrt{3} \times \sqrt{3}$)Ag in the same report [174].

A more comprehensive study of the conductivity of vicinal Si(111)($\sqrt{3} \times \sqrt{3}$)Ag has been made by Matsuda *et al.* using three different approaches [151]. In this work a micro 4 point probe in the van der Pauw geometry is contacted to the surface and the resistance as a function of the sample rotation is measured. From these measurements the 1D conductance of a step is estimated as $\approx 3 \times 10^3 \Omega^{-1} \text{ m}$. This is shown to be comparable to the expected conductance if one considers the step edges as barriers which the

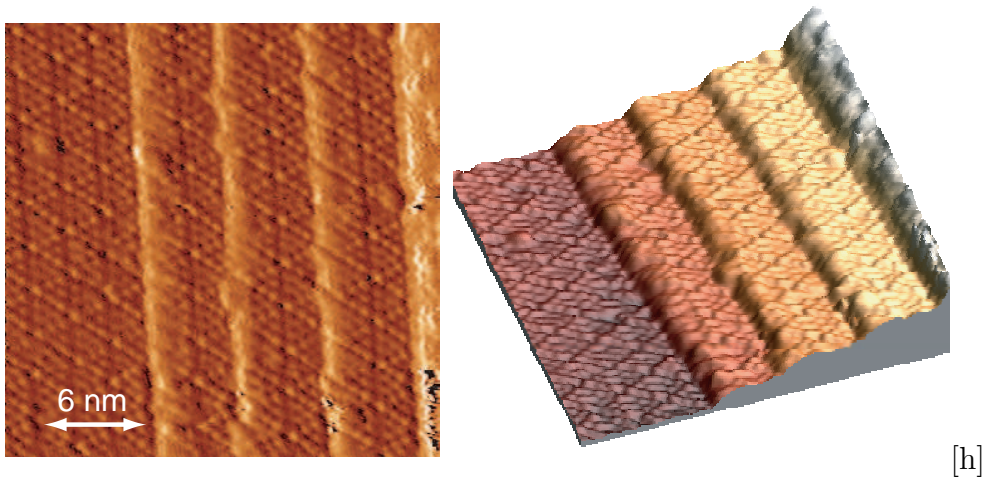


Figure 4.7: STM image of the monatomically stepped terraces of Si(111)(7×7) surface with a miscut of 3°. The step edges are parallel to the $[1\bar{1}0]$ surface vector (the measurement was made by Yu Suzuki [172]).

carriers can only cross by tunneling.

It should be noted that the analysis in reference [151] is not correct. In this work, the difference between the parallel and perpendicular resistances is assumed to be equal to the resistance of the steps between the probes. This is not the case since the existence has an effect on the measurements made in all orientations. This becomes apparent from the numerical solution of Poisson’s equation which is discussed in section 4.3. However, an intuitive approach to understanding this result is to consider the case of highly resistive steps and low resistance plateaus; it is clear that when the current is passed across the steps there will be an increased resistance, however it is increased by less than one may expect since the lateral spread of the current is greater than in the step-free case. More significantly, when the current flows parallel to the step edges, the resistance is also increased relative to a step-free surface since the lateral spread of the current is now restricted by the steps. By ignoring this, the step conductivity estimated by Matsuda *et al.* [151] is a significant overestimate (a model to illustrate the effect of steps on the measured conductance is presented in section 4.3).

A theoretical study of the resistance across an atomic step on Si(111)($\sqrt{3}\times\sqrt{3}$)Ag has been made [150]. The resistance of the step was found to be dependent on the geometry of the step edge; for example the adsorption of additional Ag atoms at the step edge could have a dramatic influence.

In conclusion, since silicon wafers often have a orientation tolerance of $\approx 1^\circ$, the issue of steps cannot be ignored. Although vicinally cut Si(111) is currently receiving a lot of interest, the effect of steps on the surface conductivity has not been conclusively studied. However, for both vicinal the Si(111)(7 \times 7) and Si(111)($\sqrt{3} \times \sqrt{3}$)Ag surfaces, it appears that the conductivity may be significantly influenced by steps.

4.2.2 Experimental Details

The sample preparation and measurements are made using the experimental setup described in chapter 4.1.3. In this section, the details of the surface preparation are reported.

4.2.2.1 Preparing Si(111)

6 mm by 4 mm samples were cut from 4" and 6" wafers (with the longer side perpendicular to the primary flat), and mounted on the sample holder such that each end was held by a clean tantalum foil. When placed in the cleaning stage, one clip touched against an electrical connection whilst the other was at ground potential. Thus a direct current could be passed through the sample, and the temperature increase could be read using a pyrometer. In order to calibrate the pyrometer, several samples were slowly heated to their evaporation temperature. This also ensured that the sample holders were fully degassed.

Preparation advice is widely available in the published literature, however the most reliable recipe was found to be that provided by T. Kampen [175]. This involved heating the sample to $\approx 650^\circ\text{C}$ until it was fully degassed (this usually required 12 to 24 hours), then to flash the sample to $\approx 1250^\circ\text{C}$ for 10 to 20 seconds. The sample was then cooled quickly to below $\approx 800^\circ\text{C}$, and then slowly back to room temperature. This recipe was found to reliably produce very sharp (7 \times 7) LEED patterns. Figure 4.8 shows such a (7 \times 7) reconstruction at an electron energy of 60 eV.

Occasionally, the surface preparation failed. The LEED pattern still showed 7x7 structure, but when the surface was examined optically, islands with a typical size of $\approx 5\mu\text{m}$ were visible across the surface. The source of this problem was not conclusively isolated, but perhaps the most probable source is that some carbon rich contaminant (such as pump oil) had been in contact with the surface, and that the high temperature anneal had caused the formation of islands of SiC which are commensurate with the surface. The formation of SiC structures by similar methods has been reported, for example by Wu *et al.* [176], and the SiC film grown by them shows a striking similarity with

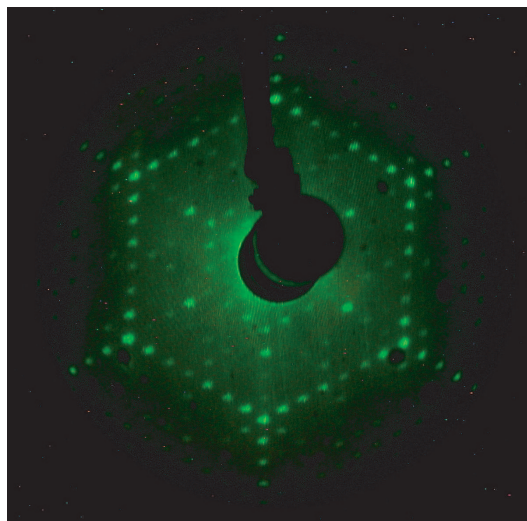


Figure 4.8: Photograph of the room temperature LEED pattern produced by the Si(111)(7×7) surface using a kinetic energy of 60 eV.

the photograph of our contaminated surface shown in figure 4.9. On these grounds, it was assumed that the observed surface contamination was due to carbon rich contaminants on the Si surface prior to annealing. Therefore, extra care was taken to keep the samples clean. This included rinsing the surface with iso-propanol and blowing the solvent off using clean N₂ gas.

4.2.2.2 Silver Deposition

The clean Si(111)(7×7) surface was prepared using the procedure described above. Silver was deposited onto the surface by means of a simple evaporator which was mounted such that LEED measurements could be made during deposition. Thus, the film thickness could be estimated from the LEED spot intensities. Evaporation could only be carried out at room temperature.

According to STM [157, 158, 160], optical [161] and photoelectron diffraction studies [154], room temperature deposition of Ag on the Si(111)(7×7) surface results in the formation of islands with a preferential height of ≈ 5 monolayers. During the deposition, the LEED spot intensity was measured, and the results compared with a simple model of the Ag growth. In short, the LEED spot analysis is consistent with the above reports, and from this analysis, a coverage of $\approx 3.0 \pm 0.5$ monolayers was repeatably produced. This is believed to correspond to a $\approx 60\%$ coverage of islands with a preferential height of 5 atomic layers. A description of the LEED analysis and model are given in section 4.3.2.1.

Since the $(\sqrt{3} \times \sqrt{3})\text{Ag}$ surface has been extensively studied, there is plenty

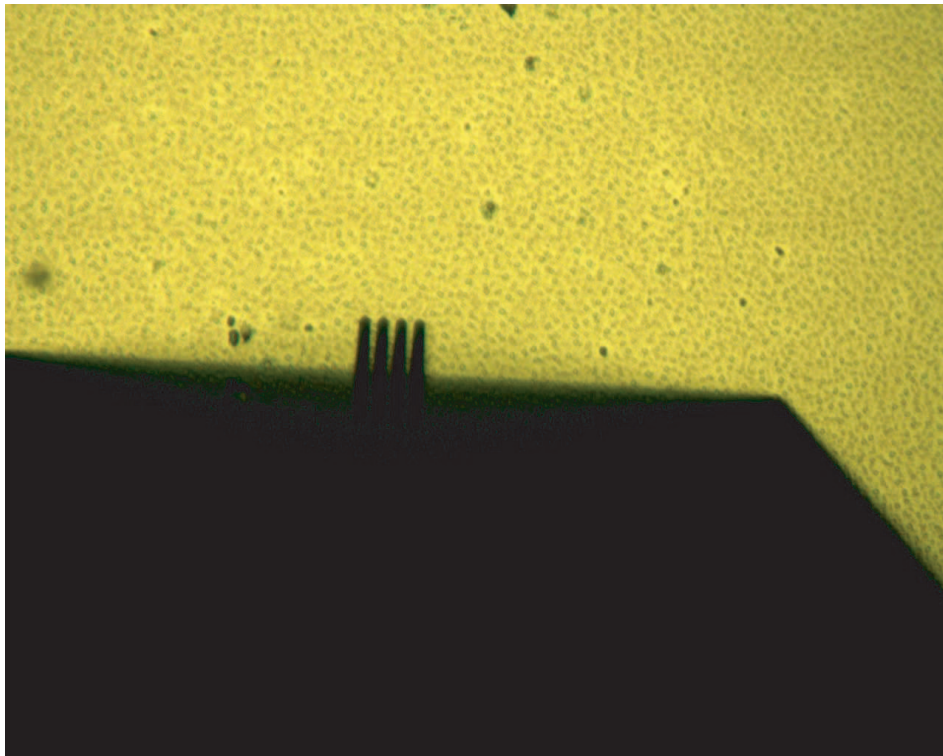


Figure 4.9: Optical image of the contaminated Si(111)(7×7) surface. The scale of the islands can be estimated from the 4 point probe which has a spacing of 10 μm . After comparison with figure 2 of ref [176], the contamination is thought to be SiC.

of advice on its preparation available [121, 122, 131, 132, 143–145, 154, 161]. This preparation advice can be categorised into a) deposition at elevated sample temperatures and b) deposition at room temperature, followed by an anneal. Since it is not possible to elevate the sample temperature without making complicated modifications to the experimental setup, the latter approach was employed. In the above references, the annealing temperature varies from 320 °C [154] to 600 °C [144, 145]. Therefore, a series of sample preparations was made in a similar temperature range. After each preparation, the surface order was checked by LEED, and the $(\sqrt{3} \times \sqrt{3})$ was observed, however the sharpest LEED patterns were observed in the temperature range 500 to 600 °C. According to Crain *et al.* [145] this is consistent with producing a 1 monolayer film instead of the $1+\Delta$ monolayer films that are observed after lower temperature anneals. Therefore, the measurements of the $(\sqrt{3} \times \sqrt{3})\text{Ag}$ reconstruction presented in subsection 4.2.3.3 are made on samples prepared at 550 ± 30 °C.

Note that for temperatures above ≈ 600 °C, the temperature was measured with a pyrometer. However, temperatures lower than this cannot be directly measured, so the temperature (T) was instead estimated from the power (P), assuming that:

$$P \propto T^4 \quad (4.16)$$

This assumption was checked, and the constant of proportionality is found by recording P and T throughout the temperature range of the pyrometer. This assumption was found to be a good approximation.

4.2.2.3 Preparing Vicinal Surfaces

It has been demonstrated that the surface structure of vicinal Si(111)(7×7) is sensitive to the preparation. Detailed STM studies [171, 172] shows that wafers with a slight miscut tend to produce monatomic steps, whilst for larger miscuts step bunching and multi-atomic steps occur, although this also depends on the surface preparation. In this experiment, monatomic steps are of greatest interest, therefore a small miscut is used.

The wafer used was supplied to Chemnitz Technical University by Silchem GmbH. The effect of the preparation on the surface structure was extensively studied by STM, and preparation recipes were found which reliably produced regular terraces with long range order. Samples of the same wafer were then prepared to the same recipes in our 4 point probe chamber. The wafer has a nominal miscut of 0.35 °, but was measured to have a miscut of 0.20 ° by STM. The wafer is phosphor doped and has a nominal resistivity of 7.5 Ω cm. The

samples used were 6 mm by 4 mm with the long side parallel to the primary flat. The sample was heated in vacuum by passing a current through the sample in the $[1\bar{1}0]$ direction (i.e. parallel to the step edges and parallel to the long axis of the sample).

From the STM study by Suzuki [172], it was shown that regular monatomic steps could be produced using preparation 1 below. An STM image of a surface produced using the same recipe is shown in figure 4.10.

Preparation 1:

Anneal to 650 °C for 3 days

6 cycles of;

flashing to 1250 °C for 30 seconds then back to 650 °C for 5 minutes

Cool to room temperature.

Additionally, it was shown that the steps could be dispersed using the following preparation:

Preparation 2:

Anneal to 650 °C for 1 day

Then increase the temperature to 900 °C for 1 hour

Cool to room temperature.

Several samples were prepared using both of the above preparation recipes. Some difficulties were encountered in making reliable contacts to the samples, and thus several samples were discarded because they could not be evenly heated. After some practice, samples could be reliably prepared. Similar preparation advice can be found in references [171, 177].

A LEED spot profile analysis was made after each surface preparation. After "preparation 1", the LEED spots were slightly streaked, and after "preparation 2", the LEED spots were noticeably sharpened. Figure 4.11 shows the profile of the 1st order LEED spots at 60 eV. The broadening of the spots is quite weak, but this is consistent with the expected terrace size; By fitting two gaussian components to each intensity profile, the terrace size for "preparation 1" could be estimated. The same fit was also applied to the "preparation 2" intensity profile. From this, it could be inferred that both preparations produced a distribution of terrace sizes from ≈ 10 nm to ≈ 60 nm, but that number of terraces after "preparation 1" was increased by $(83 \pm 6 \%)$ relative to "preparation 2".

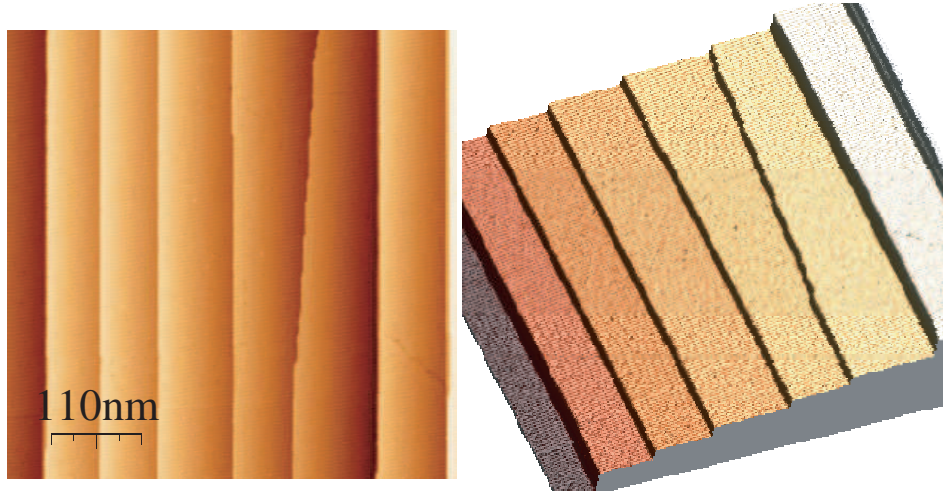


Figure 4.10: An STM image of the 0.2° miscut surface. Using the recipe for "preparation 1", regular monatomic steps could be produced. Similar STM images made several millimeters apart showed that such terraces extend across the entire surface.

4.2.3 Results

In the following subsections, the results of the measurements of Si surfaces are presented. In each case, the probes are made of Au coated SiO_2 and have a spacing of $10\ \mu\text{m}$. Each data series is made using more than one probe and more than one sample preparation. This is because the probes have a very short life - especially on cold surfaces. The probes are easily worn or broken by vibrations and thermal expansions (although every effort was made to minimise this). Also, at low temperatures, the Au coating is easily damaged. In order to replace the probe, it is necessary to vent and open the chamber, and thus a new surface has to be prepared.

When a new probe and/or sample is used, the highest and lowest temperatures are measured first, thus the repeatability of the measurements is always ensured.

Each measurement is made by measuring the potential drop (V) across the inner two probes whilst the current through the outer two probes is linearly ramped from $-I_0$ to $+I_0$ and then back to $-I_0$. A range of values of I_0 is used, from $50\ \text{nA}$ to $50\ \mu\text{A}$. Each measurement consists of many scans containing approximately 100 points, with 50 samples of V at each point. Since the signal to noise ratio depends on a number of factors (such as vibrational stability), the number of scans is chosen such to compensate this. The data are commonly linear for small currents, with some non-linearities above a threshold current, especially for the low temperature measurements of the

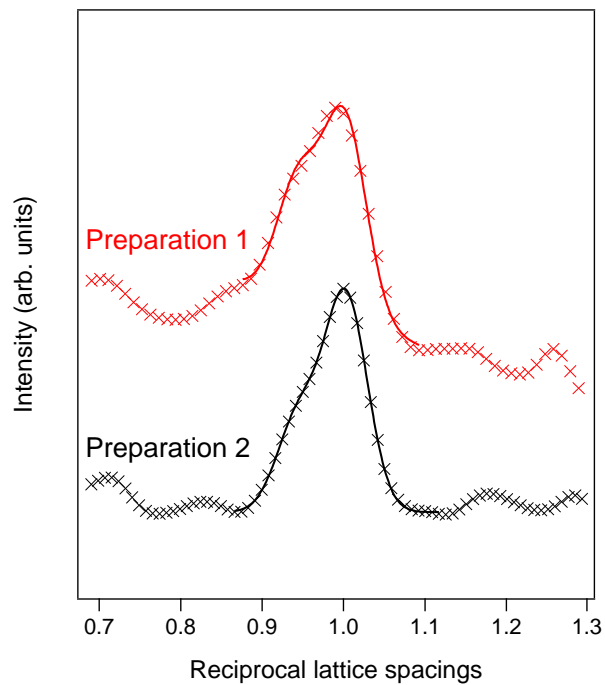


Figure 4.11: LEED spot intensity (\times markers) versus reciprocal distance (in the direction of the streaking) of the two surface preparations. The intensity plots were fitted by two Gaussian components (solid lines). From this fit, it was inferred that the surface consisted of a distribution of terrace sizes between 10 nm and 60 nm, and that the number of terraces was increased after "preparation 1" by $(83 \pm 6 \%)$ relative to "preparation 2".

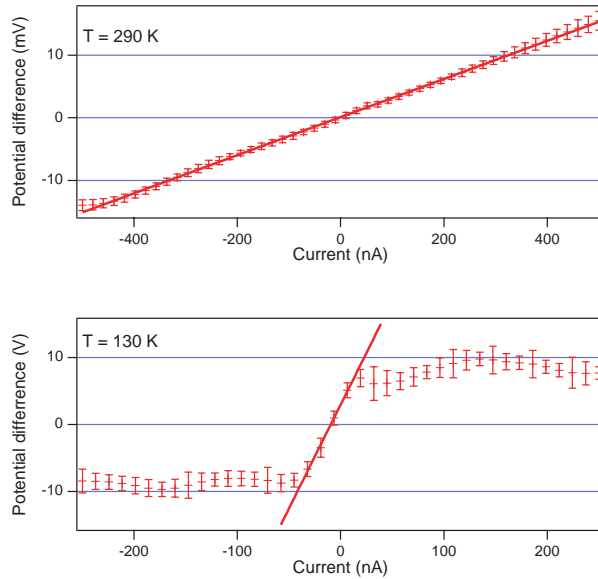


Figure 4.12: Typical Current versus Voltage (I-V) curves from "Sample A" with the Si(111)(7×7) surface reconstruction. Measurements at two temperatures are shown; 290 K (left panel) and 130 K (right). The linear fits to the measurements around $I = 0$ are also shown.

(7 × 7) surfaces. Therefore, the linear part of the measurement is used and the data in this region are fitted using a linear fit and the uncertainty is estimated from the statistical spread of the measured data.

The measurements are too numerous to show in full, so a representative selection from the measurements of "Sample A" (described in the following section) are shown in figure 4.12. It can be seen from the figure that at high temperatures (for example 290 K), the behaviour is ohmic across the entire current range, whereas at low temperatures (for example at 130 K), the behaviour is only ohmic for currents of less than ≈ 20 nA. It is interesting to consider what may cause the sudden change in dI/dV in the low temperature measurements. This is discussed in the following section.

4.2.3.1 Si(111)(7×7)

The results of the measurements on Si(111)(7×7) are shown in figure 4.13. Three different samples (named A to C) are compared; the samples are p -type with nominal resistivities of A; 190 Ω cm, B; 30 Ω cm and C; 1.3 Ω cm.

Samples A and C were measured using the modified 4 point probe chamber at the University of Aarhus, whilst sample B was measured together with T. Hansen using the original setup at the Technical University of Denmark,

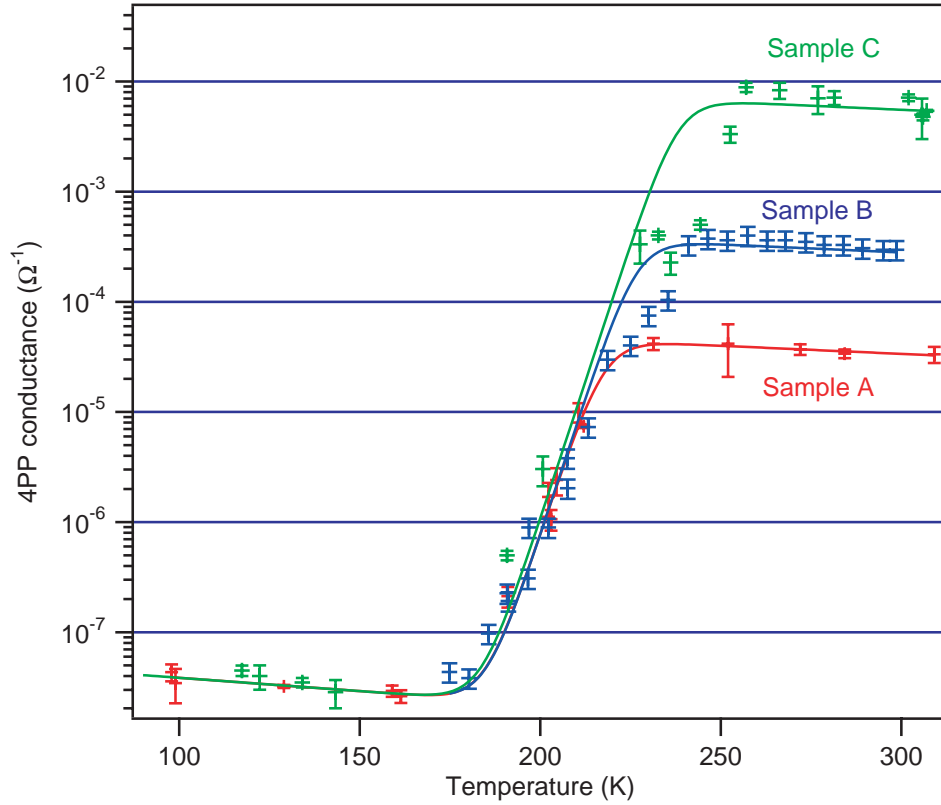


Figure 4.13: Results of the measurements on 3 different Si(111) samples, each with the (7×7) reconstructed surface. At low temperatures, the measurements show a common conductance which is attributed as being surface conductance whereas at higher temperatures, the measurements reflect the bulk conductivity.

Kgs. Lyngby. One of the major differences is that in the original setup, the sample temperature could only be estimated from the cryostat temperatures, whereas in the modified setup it could be measured directly using a K-type thermocouple mounted close to the sample. After mounting the thermocouple, the sample temperature was recorded as a function of the cryostat temperature was recorded. The original sample temperature estimation (as described in [63]) was found to be very inaccurate, but using this new information, a simple correction could be applied. Thus it should be noted that whilst samples A and C are plotted against *measured* temperature, sample B is plotted against *estimated* temperature.

The first feature which is apparent is the enormous change in the measured conductance at around 200 K. In the case of sample C, it is around 5 orders of magnitude in the temperature range ≈ 180 to 230 K. Another interesting feature is that the 3 samples reach a common low temperature saturation, whereas at higher temperatures the three measurement series saturate at different conductances. Finally, a closer inspection reveals that both the high and low temperature saturations have small negative gradients.

A qualitative understanding of these measurements is that the high temperature saturations occur because the measurement is dominated by the bulk conductivity; at higher temperatures, the conductivity of the space charge layer is higher, and thus the current can penetrate into the bulk. Conversely, at lower temperatures, the space charge layer becomes highly resistive, and thus the current is restricted to the surface. From this explanation, one would expect the measured room temperature conductance to be related to the bulk resistivity by equation 4.10, and indeed this is found to be the case. Similarly, one would expect the low temperature conductance to be related to the surface resistivity by equation 4.7. If this is indeed the case, then this measurement yields the surface resistivity to be $\approx 1.1 \times 10^8 \Omega$ (which corresponds to a surface conductivity of $\approx 9 \times 10^{-9} \Omega^{-1}$). This is consistent with the least conductive estimates reported elsewhere (see subsection 4.2.1.2).

This interpretation is also consistent with the I-V lineshapes shown in figure 4.12, in which the low temperature measurements are seen to only exhibit ohmic behaviour over a small current range. Although the reason for this cannot be given definitively, one could suppose that the maximum current that can be passed through the surface is much less than for the bulk, and thus only the surface dominated measurements display non-ohmic behaviour. Another interpretation could be that the mode of conductivity changes in the presence of a sufficiently strong field: The observed threshold current in figure 4.12 corresponds a potential of ≈ 15 V. Since this is applied over $10 \mu\text{m}$ of the surface, it produces a very strong field in this region of the surface and

thus it could be responsible for the observed change in conductance.

One way to classify the surface conductivity as metallic or non-metallic is to compare the absolute value of the conductivity to the minimum metallic conduction in two dimensions following the Ioffe-Regel criterion ($3.8 \times 10^{-5} \Omega^{-1}$) [111, 178]. According to this comparison, Si(111)(7x7) would be classified as a "bad metal". This would also be consistent with the NMR study conducted by Schillinger *et al.*, which suggested that the surface is close to a Mott-Hubbard metal-insulator transition [107].

In order to interpret our measurements further, it is necessary to have a better understanding of the temperature dependence of the space charge layer conductivity, and how this affects the measured conductance. Such an understanding requires a numerical model, and this is discussed in section 4.3.

The slight negative gradients in the high- and low-temperature saturations are attributed to the thermal decrease in carrier mobility due to increased phonon scattering. This is commonly seen in metals, but usually in a semiconductor, the thermal increase in the carrier density outweighs this effect. However, when the measurements are made in a temperature region in which there is no strong change in the bulk carrier density, the temperature dependence of the mobility dominates the gradient at saturation. This is also demonstrated using the model presented in section 4.3.

4.2.3.2 Si(111) with Silver Islands

The results of the measurements on an Ag film on Si(111) are shown in figure 4.14. The substrate used is *p*-type doped with a resistivity of $190 \Omega \text{ cm}$ (i.e. it is sample A from the previous section). As a comparison, the measurements of sample A with the clean (7x7) surface are also plotted.

The most apparent difference between these measurements is that the Ag island film does not show the strong temperature dependence that was apparent for the (7x7) surfaces. Also, a similar small negative gradient is observed.

Again, these measurements are not simple to understand without applying the model discussed in chapter 4.3. However, a qualitative understanding is that the small amount of Ag deposited onto the surface has increased the surface conductivity by around 5 orders of magnitude, and thus the measurement is always dominated by the surface conductivity.

4.2.3.3 Si(111)($\sqrt{3} \times \sqrt{3}$)Ag

The results of the measurements on the Si(111)($\sqrt{3} \times \sqrt{3}$)Ag surface are shown in figure 4.15. The measurements are carried out on sample A (i.e. *p*-type

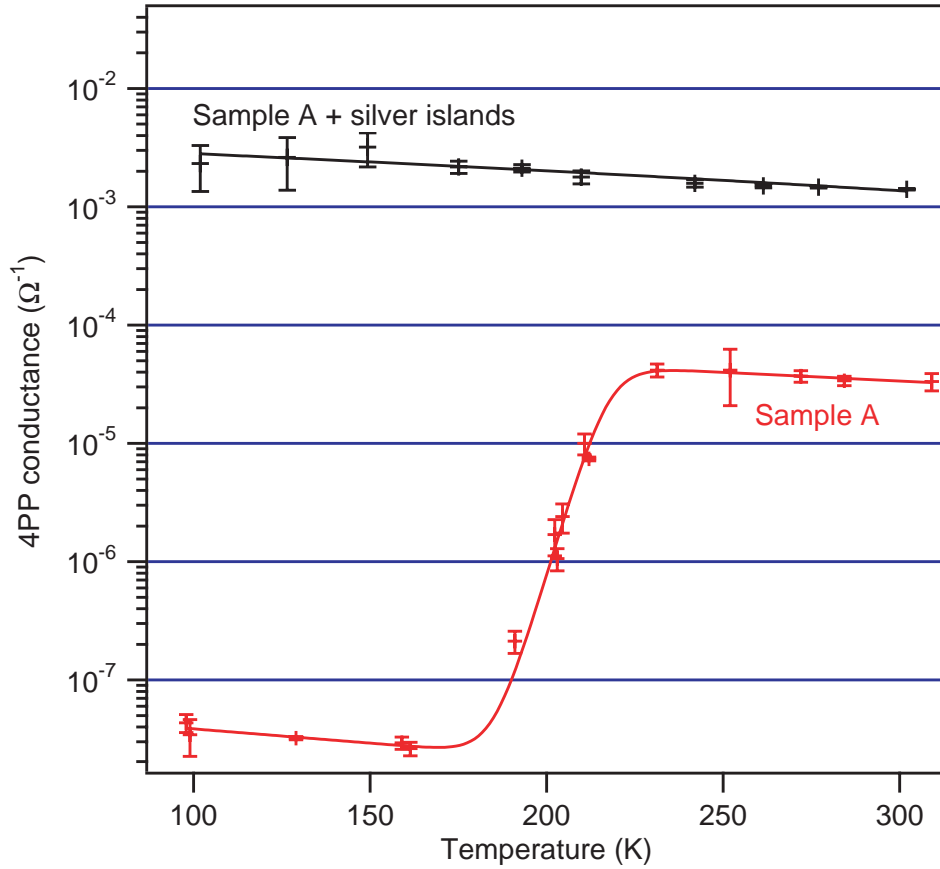


Figure 4.14: Results of the measurements on "sample A" after the deposition of silver. As a comparison, the measurements on the clean Si(111)(7×7) surface of "sample A" are also plotted. Whilst the clean surface shows an interesting transition at around 200 K, the measurements on the silver coverage show a gentle decrease in conductance with temperature.

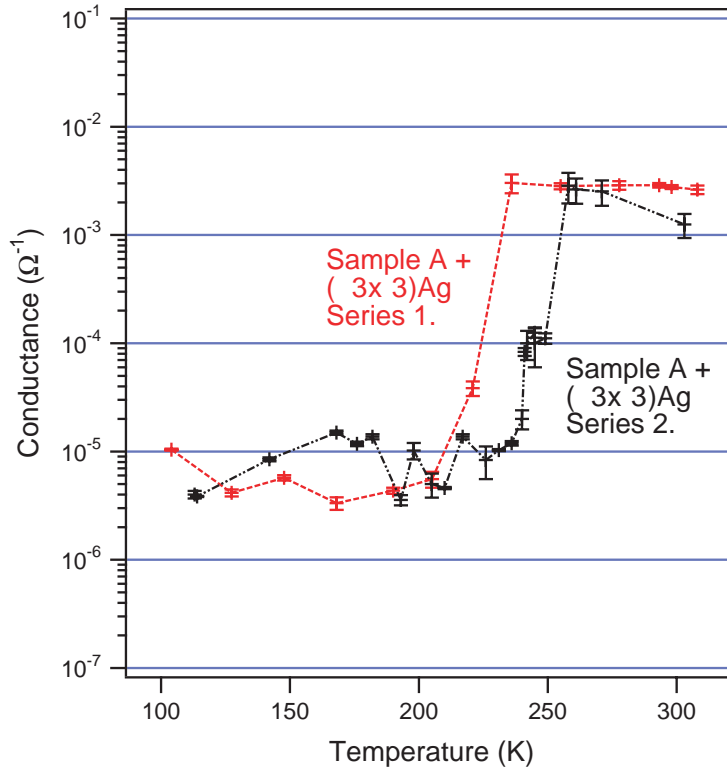


Figure 4.15: Measurements of the $\text{Si}(111)(\sqrt{3} \times \sqrt{3})\text{Ag}$ surface. Unlike the measurements on the other surfaces, the transition temperature and surface conductivity are not exactly reproducible, but the general trend of a sharp transition is always seen.

doped with a resistivity of $190 \Omega \text{ cm}$).

In figure 4.15 strong transitions, reminiscent of those seen in figure 4.13, are observable. However, a closer inspection reveals that neither saturation corresponds to the bulk resistivity, the transition is over a much smaller temperature range and the low temperature saturation does not have the characteristic small negative gradient that is seen in all of the other measurements. Therefore the observed transition on this surface cannot be understood in the same way as the (7×7) surface.

In this case, as with the Ag island deposition, the measured conductivity is thought to always be surface dominated. Therefore, it appears that the observed transition is due to a change in the surface conductivity caused by the surface phase transition discussed previously. The room temperature conductance corresponds to a surface conductivity of $(6.1 \pm 0.3) \times 10^{-4} \Omega^{-1}$ which is comparable to that found by Hasegawa *et al.* in reference [148]

Additionally, it is seen that these measurements, unlike the measurements

Preparation	Conductivity (Ω^{-1})	
	Lower limit	Upper limit
"Preparation 1"	2×10^{-7}	6×10^{-7}
"Preparation 2"	1.5×10^{-8}	3×10^{-8}
"Step free"	6×10^{-9}	1.1×10^{-8}

Table 4.1: Results of the measurements on stepped Si(111)(7×7) surfaces. The upper and lower limits of the surface conductivity in the temperature range 100 K to 160 K for each of the preparations

of other surfaces, are difficult to reproduce exactly. The actual value of the surface conductivity for each phase, and the temperature of the transition appears to be very sensitive to the surface preparation. Perhaps this can be attributed to the role of additional Ag adatoms, since it has been shown that the pinning of the Fermi level at the surface (and hence the band bending) depends on the number of extra adatoms, and, more directly, it has been proposed that the extra adatoms act to electron dope the surface.

4.2.3.4 Vicinal Surfaces

Low temperature (and therefore surface sensitive) measurements were made on vicinal Si(111)(7×7). The results are shown in table 4.1, and it can be seen that the surface conductivity after "preparation 1" (i.e with an enhanced step density) is increased by about an order of magnitude relative to "preparation 2". Similarly, the surface conductivity after "preparation 2" is increased by about ×2 relative to that of the nominally flat surface.

This indicates that the step edges have a higher conductivity than the terraces, although the effect is not especially strong since the observed increase in conductance of $\approx \times 10$ after "preparation 1" corresponds to a step density of ≈ 30 steps per μm . Thus, for a four point probe with a probe spacing of $10 \mu\text{m}$, this corresponds to ≈ 300 steps between adjacent probes.

In order to estimate the conductivity of a single step, a numerical model is required. This is described in section 4.3

No previous reports of the conductivity of monatomic Si(111)(7 × 7) steps could be found. However, a study of the conductivity of Si(111)($\sqrt{3} \times \sqrt{3}$)Ag steps [151] concludes that the step edges decrease the conductivity of the surface, and a study a large step bunch on Si(111)(7 × 7) by S. Hasegawa *et al.* [174] also concludes that the conductivity is reduced by steps, but neither of these studies can be fairly compared with our result.

For our surface, the conductivity in the absence of steps has been shown to

be very low. It is plausible that the additional dangling bonds expected at the step edges are a source of additional carriers and thus act to dope the surface. Therefore it is not especially surprising that the conductivity is improved.

4.2.4 Conclusions

In conclusion, the conductance measurements on the Si(111) surfaces show some interesting effects. Firstly, the (7×7) surface shows a transition from surface dominated to bulk dominated conductance as the temperature is increased. The $(\sqrt{3}\times\sqrt{3})\text{Ag}$ measurements are interpreted in terms of surface phase transition, and the percolated Ag island surface shows simple metallic surface conductance. Finally, measurements of vicinal surfaces show that the conductivity is enhanced by additional steps.

In order to understand the results quantitatively, a numerical simulation of the contribution from the space-charge layer and bulk is required. This is discussed in the following section.

4.3 Understanding the Measurements of Si(111) Surfaces

4.3.1 Introduction

In order to understand the experimental results, some modeling is required. Initially, the model of the growth of Ag on Si(111) is presented, along with a comparison to the experimental LEED pattern. Following this, models for the band-bending in Si(111) surfaces, and the resulting simulations of the measured conductivity are discussed.

4.3.2 The Models

4.3.2.1 Silver Islands on Si(111)(7×7)

The growth mode of Ag on Si(111) at room temperature is a little complex. Theoretical and experimental studies were discussed in section 4.2.1.4. In summary, it was found that Ag forms islands with a preferential height of ≈ 5 atomic layers which gradually increase in surface coverage beyond the percolation threshold until the entire surface is covered with 5 or more atomic layers. Although this growth mode has some apparent similarities to Stranski-Krastanov, it is significantly different.

The growth is modeled using an "atom by atom" approach. An initial contact site is selected using a Monte-Carlo approach, the atom can either a) stick at this site, b) desorb or c) diffuse to a neighbouring site and the selection is made on the grounds of a probability which is assigned according to the potential number of new bonds and the bond enthalpies. In case c), the atom moves to a neighbouring site and then the 3 possible options are re-assessed and the loop is repeated until the atom eventually sticks or desorbs. The direction of the diffusive motion is chosen randomly. A schematic diagram of this model is shown in figure 4.16.

The model requires several parameters to be known; the Ag-Ag bond enthalpy, the Ag-Si bond enthalpy and the diffusion coefficient. However, it was found that the growth mode was only sensitive to the ratio of the Ag-Ag to Ag-Si bond enthalpy, and this was estimated by comparing the outcome of the model with the available experimental measurements.

Figure 4.17 shows some results from the model. The left hand panels show simulated STM images for four coverages, and the lower right hand panel shows the distribution of island heights for each coverage. The nominal 3 monolayer coverage is slightly beyond the percolation threshold and is comparable to the measured surface of ref [158] which is shown in figure 4.6.

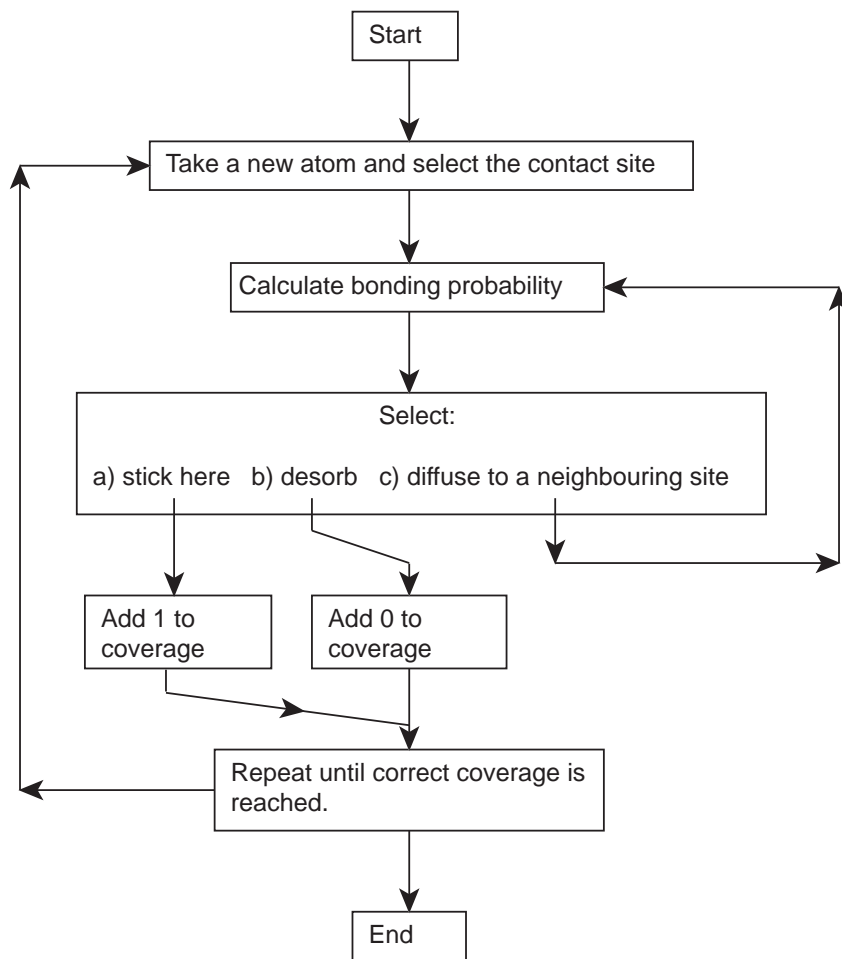


Figure 4.16: Schematic diagram of the Ag growth model. The number of atoms adsorbed at each site is recorded in a matrix and the loop is repeated until the desired coverage is reached.

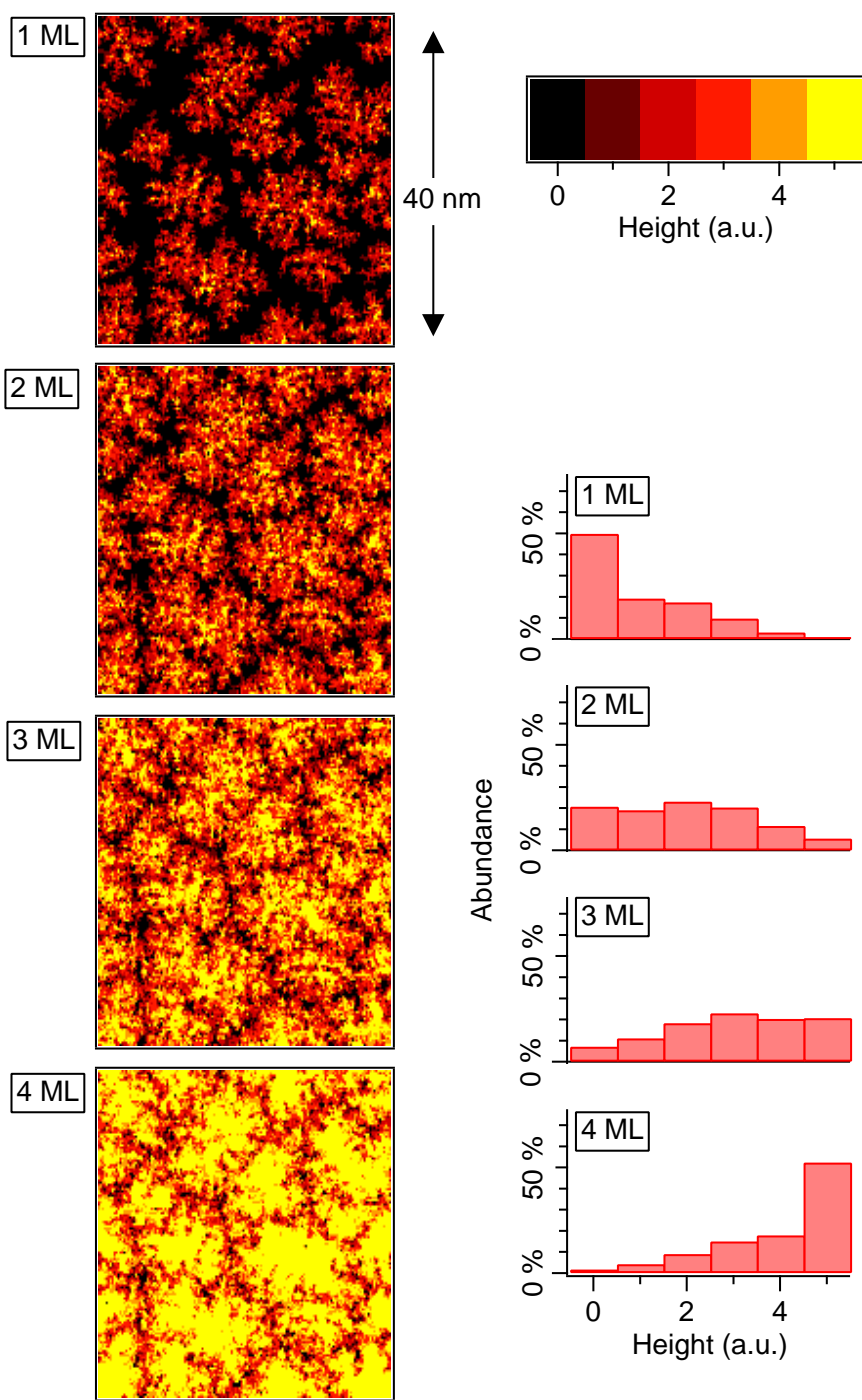


Figure 4.17: Model of the Ag growth during deposition at room temperature. The images in the left hand column show simulated STM images throughout the deposition. The figures on the right hand side show the distribution of heights taken from the simulated images. The 3 monolayer coverage is comparable to the measured STM image and height distribution shown in figure 4.6.

The next step is to compare the results of the model with the available measurements from the actual deposition process: The deposition was carried out in front of the LEED screen, thus it was possible to make real-time measurements of the LEED pattern. Using a constant screen voltage, lens voltages, emission and so forth, the changes in the observed LEED pattern are only dependent on the deposition, thus a constant electron energy of 60 eV was selected (since this allows the first order Si(111) and Ag(111) spots to be seen), and the LEED pattern was photographed throughout the deposition. Unfortunately, the light emitted from the evaporator increased the background intensity of the LEED screen, therefore it was necessary to heat the evaporator using pulsed heating, and to synchronise the photography such that photographs were made between pulses. This was relatively simple to achieve once a digital camera was found that could be easily controlled from a remote computer. The LEED spot intensities were then estimated by integrating the intensity recorded by each pixel on the camera over a circular area around each spot. By repeating this process for a similar circle that was close to (but not enclosing) a spot, the background was estimated. The results are shown in the upper panel of figure 4.18.

From the model of the Ag/Si surface, a simulated LEED pattern can be made. The intensity of the Si(7x7) spots was simply estimated as being proportional to the area of the surface with no absorbed Ag. To estimate the intensity of the Ag(1x1) and Si(1x1) spots, some further assumptions are required: The electrons which contribute to the Si(1x1) spots are assumed to be attenuated by passing through an overlayer following Beer's law. It was also assumed that the Ag overlayer forms following the Ag(111)(1x1) crystal structure, thus the Ag(1x1) spot intensity is estimated by considering the proportion of the surface which is covered, and the thickness of the coverage - using a geometric sum term to model the attenuation of the deeper Ag layers. The results of his model are shown in the lower panel of figure 4.18.

By comparing the two panels of figure 4.18, two inferences can be drawn; a) the model fits the measured data surprising well, and thus we can assume that the model provides a reasonable description of the surface and b) the model can be used to provide an approximate calibration of the evaporator. Thus it was estimated that the evaporator produces a 1 monolayer coverage in approximately 40 to 50 seconds.

For the measurements presented in figure 4.14, a surface comprising of a percolating network of islands was required. In the above models, the percolation threshold was found to be at ≈ 2.5 monolayers, thus a nominal coverage of $\approx 3.0 \pm 0.5$ monolayers was made by depositing for 135 seconds.

The final step in this model is to estimate the conductivity of the Ag film.

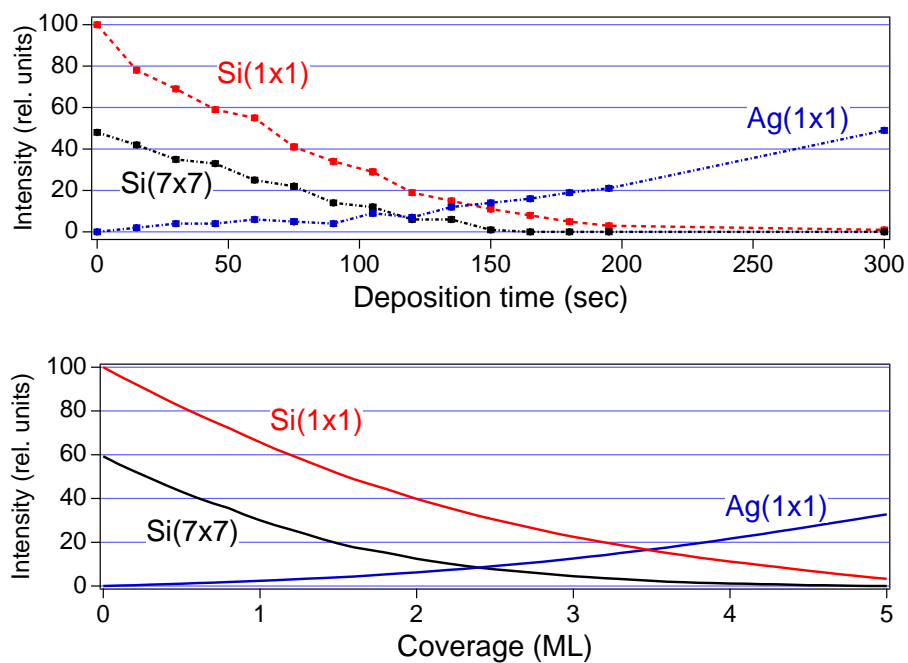


Figure 4.18: Graphs of the LEED intensity as a function of coverage. In the upper panel, the measured LEED spot intensities are plotted against the deposition time and in the lower panel, the simulated LEED intensity versus coverage is plotted. By comparison of the two, the accuracy of the model can be judged, and the evaporation rate can be estimated.

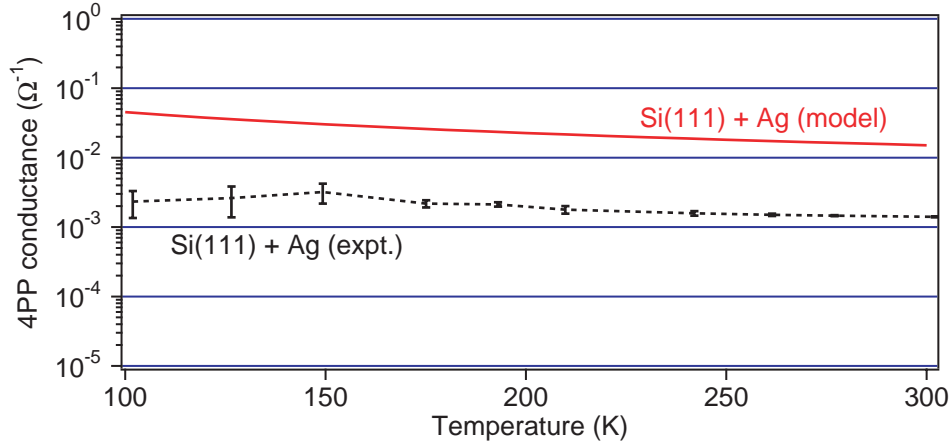


Figure 4.19: Graph to show the modeled and measured conductivity of the Si(111) surface after the deposition of a nominal 3 monolayer coverage of Ag. Although the model and measurements differ by about an order of magnitude, the temperature dependence is small in both cases, and is not dissimilar.

In order to produce a realistic model, a number of complex factors have to be considered, namely the quantum size effects which are known to occur in such thin films and the parameters of the percolating network. However, a much simpler but less accurate model can be made by assuming the film already displays the bulk properties, and that it is a uniform 3 monolayer thick layer. Both of these assumptions are inaccurate and will result in the conductivity of the film being overestimated, however this should provide a rough estimate.

The temperature dependent bulk properties of silver have been well studied [166]. Using the temperature dependent conductivity from this reference, it is straightforward to simulate the 4 point probe measurement. The results of this estimation, as well as the actual measured data are shown in figure 4.19.

From figure 4.19 it is clear that the model overestimates the conductance by about an order of magnitude. This is to be expected because of the assumptions made in modeling the film. However, it is interesting to note that the temperature dependence of the conductivity is reasonably well described by the model. This indicates that the film has "metallic" behaviour in the sense that the temperature dependent conductivity is governed by changes in the mean free path.

Finally, both the model and the measurement show that the conductivity is several orders of magnitude higher than the bulk conductivity of "sample A", thus the measurement is surface dominated at all temperatures in the studied range.

4.3.2.2 Understanding the Space Charge Region

In the previous section, modeling the conductance was relatively simple since the surface always dominated the measurement and thus the bulk and space charge layer contributions could be ignored. For the other surfaces studied, this is not necessarily the case. Therefore, in order to understand the measurements, a model of the temperature dependent conductance of the space charge layer and bulk is required.

The magnitude of the band bending at the surface (V_s) can be found experimentally; using a technique such as ARUPS, the pinning of the Fermi level at the surface (E_{sf}) can be estimated from measurements of the binding energy of the Valence Band Maximum (VBM). The position of the Fermi level in the bulk, relative to the VBM can be calculated when the bulk properties of the semiconductor are known. It is more usual to refer to the bulk Fermi position relative to the position of the intrinsic level (E_i), and this potential is known as ϕ_b . Since ϕ_b is temperature dependent, so too is the magnitude of the band bending. This is shown schematically in figure 4.20 for the Si(111)(7×7) surface and the weakly doped *p*-type bulk of "Sample A".

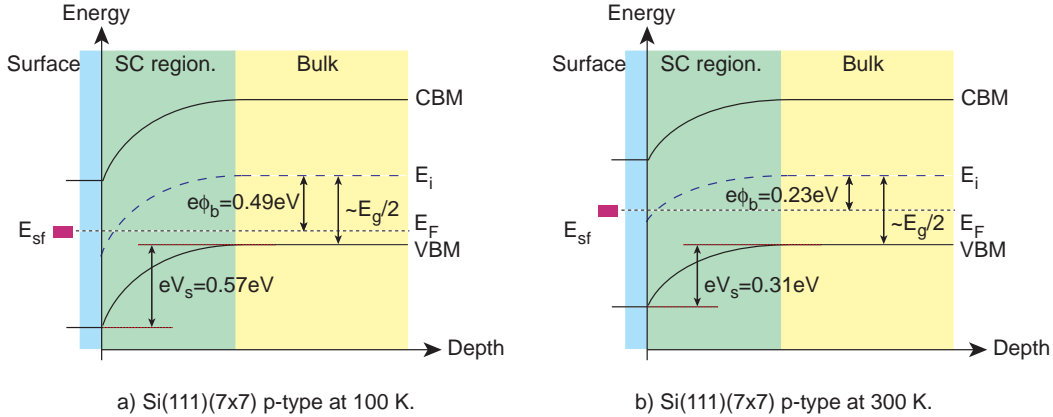


Figure 4.20: Schematic illustration of the band bending at the Si(111)(7×7) surface. The band bending at low temperature (left hand panel) is more pronounced than at higher temperatures (right hand panel) since the Fermi level in the bulk is pinned closer to the valence band maximum. In both cases the space charge region consists of a weak inversion layer.

From reference [179], the Fermi level at the surface is found to be pinned by a surface state at 0.65 eV above the VBM. From reference [180], ϕ_b is found to be 0.49 eV at 100 K and 0.23 eV at 300 K. E_i is found to be very

close to mid-gap for this weakly doped sample, thus $E_i = 0.57$ eV. From these estimates, it is straightforward to show that the band bending at the surface (V_s) is 0.57 eV at 100 K and 0.31 eV at 300 K. This means that the space charge layer consists primarily of a region of strong hole depletion, and close to the surface it is weakly inverted (that is, that the intrinsic level of forced below the Fermi level), and thus the space charge layer close to the surface is a region of weak electron accumulation.

From such arguments, one can qualitatively say that the space charge layer will be poorly conducting for this system. The small region of electron accumulation will locally have an enhanced conductivity, however, in combination with the hole depletion region, it is effectively a PN junction to currents passing from the bulk to the surface. Furthermore, it is clear that the strength of the band bending is temperature dependent, and so too is the mobility of the carriers. Thus, one can see that the temperature dependent conductivity of the space charge layer needs to be considered quantitatively. In order to do this, the carrier densities (n and p) and mobilities (μ_n and μ_p) as a function of depth (z) and temperature (T) are required, since the conductivity is given by:

$$\sigma(z, T) = e (\mu_n(z, T)n(z, T) + \mu_p(z, T)p(z, T)) \quad (4.17)$$

The number of carriers is given by:

$$n(z, T) = n_b(T) \exp\left(\frac{eV(z, T)}{kT}\right) \quad (4.18)$$

$$p(z, T) = p_b(T) \exp\left(\frac{eV(z, T)}{kT}\right) \quad (4.19)$$

where n_b and p_b are the bulk values of n and p , and V is the strength of the band bending.

At this point, one can see that the values of n and p will change by many orders of magnitude because of the exponential dependence on V and T . By comparison, the mobilities μ_n and μ_p will only change (relative to the bulk) by a numerical factor - in this case $\approx \times 2$ (see reference [111] and figure 14 therein). Thus, although such a change is not normally considered negligible, in comparison with the change in n and p it is. Therefore, the model can be simplified by assuming $\mu_n = \mu_n(bulk) = \text{constant}$ and $\mu_p = \mu_p(bulk) = \text{constant}$.

From equations 4.17, 4.18 and 4.19, one can see that the conductivity can be estimated using only the fundamental properties of the semiconductor,

provided that $V(z, T)$ is known. $V(z, T)$ can be estimated from the following expression:

$$\frac{z}{L} = \int_{V_s}^V \frac{1}{2\sqrt{\left(\frac{\cosh(u_b+v)}{\cosh u_b} - v \tanh u_b - 1\right)}} \quad (4.20)$$

where u_b and v are the so-called reduced potentials:

$$u_b = \frac{e\phi_b}{kT} \quad (4.21)$$

$$v = \frac{eV}{kT} \quad (4.22)$$

and L is the Debye length:

$$L = \sqrt{\frac{\epsilon\epsilon_0 kT}{e^2(n+p)}} \quad (4.23)$$

from references [181] and [111].

Unfortunately, there is no general analytical solution to equation 4.20, therefore it must be solved numerically. This is carried out using a MathCad script from which $V(z)$ is found for a given system. From this, it is straightforward to estimate the conductivity throughout the space-charge layer. Figure 4.21 shows the solution for "Sample A" with the (7×7) reconstructed surface for temperatures in the range 100 K to 300 K.

From figure 4.21, it can be seen that the carrier density changes by several orders of magnitude across the space charge region. By comparison, the change in the carrier mobility is insignificant.

A similar calculation can also be carried out for the $(\sqrt{3} \times \sqrt{3})$ surface; figure 4.22 shows a schematic band diagram for this surface on the substrate of "sample A". There are two important differences from the (7×7) surface; firstly the band bending is much weaker since the surface state pins the Fermi level closer to the VBM, and secondly, there is a much greater uncertainty since a significant spread of values for E_{sf} has been reported [127, 131, 143, 145]. Perhaps the reason for this uncertainty is that the position of the surface state is strongly dependent on the coverage; from ref [145], it can be seen that as the Ag coverage is increased from 1.00 atomic layers to 1.09 atomic layers, E_{sf} shifts from 0.19 eV to 0.30 eV. However, in reference [131] E_{sf} is reported as shifting from 0.08 eV to maximum of 0.26 eV (at a coverage of 1.022 monolayers) and then reducing again for further increases in coverage. In figure 4.22, the Fermi level is assumed to be pinned at 0.08 eV above the VBM and thus the space charge region at 100 K is depicted as weakly depleted, however, by considering the uncertainty in E_{sf} , the band bending could in fact be weakly accumulating.

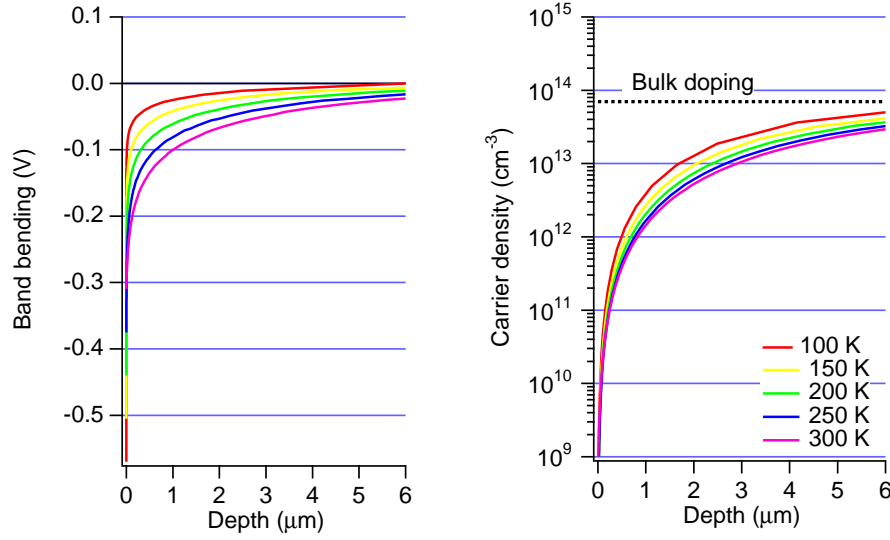


Figure 4.21: A numerical solution of equation 4.20 for "sample A" with the (7×7) reconstructed surface at a range of temperatures. The left hand panel shows the band bending as a function of depth whilst the right hand panel shows the hole densities.

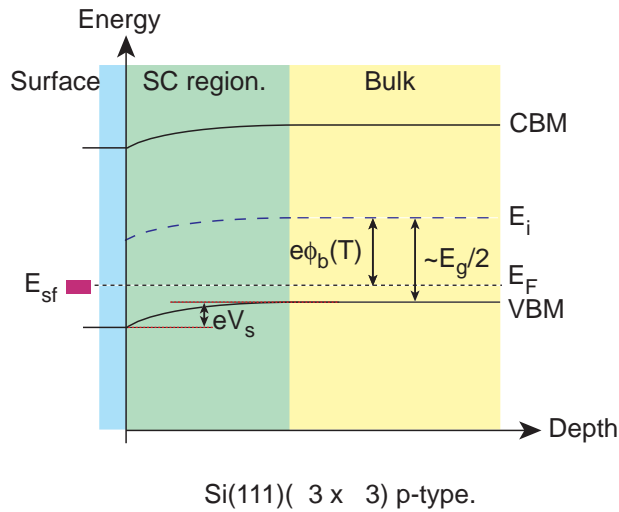


Figure 4.22: Schematic illustration of the band bending for $(\sqrt{3} \times \sqrt{3})\text{Ag}$ (1 monolayer coverage) at 100 K. Although there is some uncertainty regarding the pinning of the Fermi level at the surface, the band bending is weak compared to that of the (7×7) surface.

Once, the parameters of the band diagram are known, equation 4.20 can be solved for this surface and the temperature dependent conductivity estimated. Since there is a large uncertainty in V_s , a large uncertainty in the conductivity is also expected.

To summarise; the temperature dependent conductivity throughout the space charge layer has been calculated. For the (7×7) surface, the space charge layer consists primarily of a hole-depletion region, but close to the surface weak inversion is seen. For the $(\sqrt{3} \times \sqrt{3})$ surface, thus situation is not so certain; the relatively large uncertainty in the pinning of the Fermi level at the surface means that the space charge layer may exhibit weak hole-depletion or weak electron-accumulation. In any case, it is clear that the band bending is much less severe than for the (7×7) surface.

4.3.2.3 The Bulk and Space Charge Contributions to the Measured Conductance

Now that the conductivity throughout the space charge layer has been estimated, the question of the significance of the bulk and space charge layer contributions to the measured conductivity can be addressed.

In section 4.1.2.3, Poisson's equation could be solved analytically for isotropic surface and bulk cases. For a varying conductivity (such as in the space charge layer), an analytical solution does not exist, thus a numerical model is required:

First, the sample is modeled as a semi-infinite 3D array of elemental boxes. Each elemental unit represents a sufficiently small piece of the sample that the potential drop within the unit is negligible, and thus can be treated as constant. Each element is assigned a conductivity based on its depth from the surface, using the conductivities estimated in the previous section. The conservation equation used previously (equation 4.1) can be written in cartesian coordinates as:

$$\frac{\partial}{\partial x} \left(\sigma \frac{\partial \phi}{\partial x} \right) + \frac{\partial}{\partial y} \left(\sigma \frac{\partial \phi}{\partial y} \right) + \frac{\partial}{\partial z} \left(\sigma \frac{\partial \phi}{\partial z} \right) = 0 \quad (4.24)$$

this can then be approximated as:

$$\begin{aligned} & \left(\frac{\sigma_{x+\delta x, y, z} (\phi_{x+2\delta x, y, z} - \phi_{x, y, z}) - (\sigma_{x-\delta x, y, z} (\phi_{x, y, z} - \phi_{x-2\delta x, y, z}))}{4(\delta x)^2} \right) + \\ & \left(\frac{\sigma_{x, y+\delta y, z} (\phi_{x, y+2\delta y, z} - \phi_{x, y, z}) - (\sigma_{x, y-\delta y, z} (\phi_{x, y, z} - \phi_{x, y-2\delta y, z}))}{4(\delta y)^2} \right) + \\ & \left(\frac{\sigma_{x, y, z+\delta z} (\phi_{x, y, z+2\delta z} - \phi_{x, y, z}) - (\sigma_{x, y, z-\delta z} (\phi_{x, y, z} - \phi_{x, y, z-2\delta z}))}{4(\delta z)^2} \right) = 0 \end{aligned} \quad (4.25)$$

Using an iterative procedure, the elements in contact with the current carrying probes are assigned constant potentials (in this case +1 V and -1 V) and potentials of the other elements can be estimated. The iterations are repeated until the potentials converge to a solution.

Since all variables use S.I. units, the current in amperes can now be calculated at each elemental boundary by considering the difference in potential between the two neighbouring elements, their conductivity and the area of touching face of the elemental unit. For example, the current ($I_{x,y,z}$) flowing between two elements which are neighbours in the x direction, located at (x, y, z) and $(x + \delta x, y, z)$ is given by:

$$I_{x,y,z} = (V_{x,y,z} - V_{x+\delta x,y,z})\sigma_{x,y,z} \frac{\delta y \delta z}{\delta x} \quad (4.26)$$

where $\delta y \delta z$ is the area of the elemental unit in the plane perpendicular to the x direction, and δx is the spacing of the elemental units in the x direction.

By integrating the current over a surface (S) which encloses one of the current sources, the total current can be estimated. Since the potential of the current source was set at a fixed potential, the simulated 4 point resistance is given simply as:

$$R_{App} = \frac{V_2 - V_3}{\sum_S I_i} \quad (4.27)$$

where V_2 and V_3 are the potentials at the positions of the 2nd and 3rd probes, respectively.

Now, the bulk and space-charge layer contributions to the measured conductance can be estimated as a function of temperature and surface Fermi-level position. This is presented in the following section

4.3.3 Results: Modeling the Conductance

Using the models presented above, the measured 4 point probe conductance can be simulated. The bulk and space charge layer contributions can be estimated using only the fundamental parameters of the sample. However, in order to include the surface contribution, a semi-empirical approach is required.

4.3.3.1 Si(111)(7×7)

The results of the simulations for "Sample A" with the (7×7) reconstructed surface, along with the corresponding experimental data, are shown in figure 4.23. Additionally, a simple model which only includes the bulk contribution is included. This is discussed later in this section.

As discussed in section 4.2.3.1, the low temperature saturation of the measured data is assumed to be due to the surface contribution dominating the conductance. Thus a value for the surface conductivity has been extracted from the measured data and included in the semi-empirical model.

From figure 4.23, it can be seen that there is quite good agreement between the model and the measured data. The high and low temperature saturations are reproduced, and so too is the sharp transition at around 200 K. In the model, a dramatic decrease in the conductance of the space charge layer is seen, and this confirms the validity of the assumption that the lower saturation is caused by the surface conductance dominating the measurement. However, there are also some notable differences between the model and the experiment. First, the transition is much steeper than the model shows, and secondly, the slight negative gradients in the high and low temperature saturations are not reproduced.

The sharpness of the transition is probably underestimated in the model since a number of oversimplifications are made - for example, the temperature dependence of the mobility is ignored. In section 4.2.3.1, it was suggested that the slight negative gradient arises from the increase in phonon interactions at elevated temperatures. It is therefore not surprising that the model fails to replicate this since the carrier mobility was taken to be constant in order to simplify the calculations. However, it is worth investigating this in a little more detail because this negative gradient in the conductivity is somewhat counter-intuitive since it is commonly accepted that, although a negative gradient may occur in metals, in semiconductors the thermal increase in the number of carriers will always result in a positive gradient in the conductivity.

In this case, this is simply not true. In the temperature range 100 K to 300 K, the number of carriers in the bulk is almost constant - in fact the number varies by less than 1 % across this range. Qualitatively, this can be understood as being the temperature range in which all of the extrinsic carriers have been excited, but in which none of the intrinsic carriers have been excited. Using ref [180], it is straightforward to calculate the carrier density for this sample. This has been carried out, and the results are plotted in figure 4.24. In addition to this, the change in the bulk carrier mobility is also plotted. Although this was taken to be constant relative to the change in the number of carriers in the space charge region, in the high temperature saturation it is the only significant factor and therefore it dominates the temperature dependence of the conductivity in this temperature range.

Using these estimations for the carrier density and mobility, it is straightforward to simulate the bulk conductance - that is, the conductance that one would expect to measure if the measurement was bulk dominated. This is

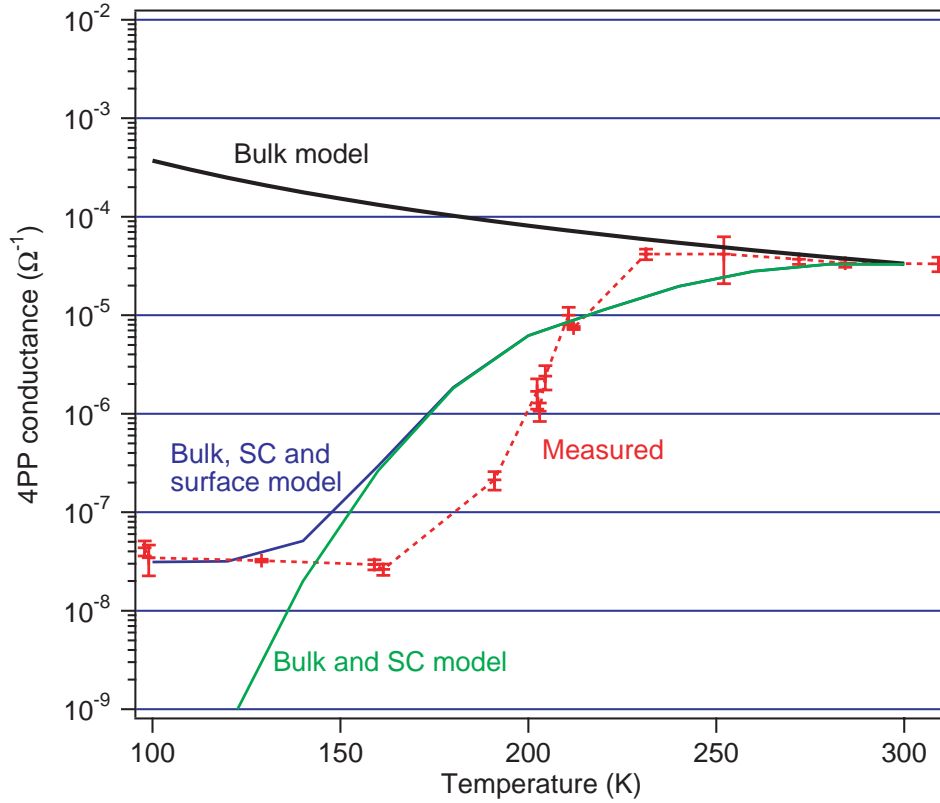


Figure 4.23: Graph to show the modeled and measured conductances of the Si(111)(7×7) surface, space charge (SC) layer and bulk. At higher temperatures, the measured conductance (red data points and red dotted line) is close to that of the modeled bulk contribution (solid black line), but as the temperature decreases, the space charge layer becomes increasing insulating until the measured conductance becomes dominated by the surface component. The model which includes the bulk and space charge layer is depicted by a solid green line and the semi-empirical model which also includes the surface contribution is depicted by a solid blue line.

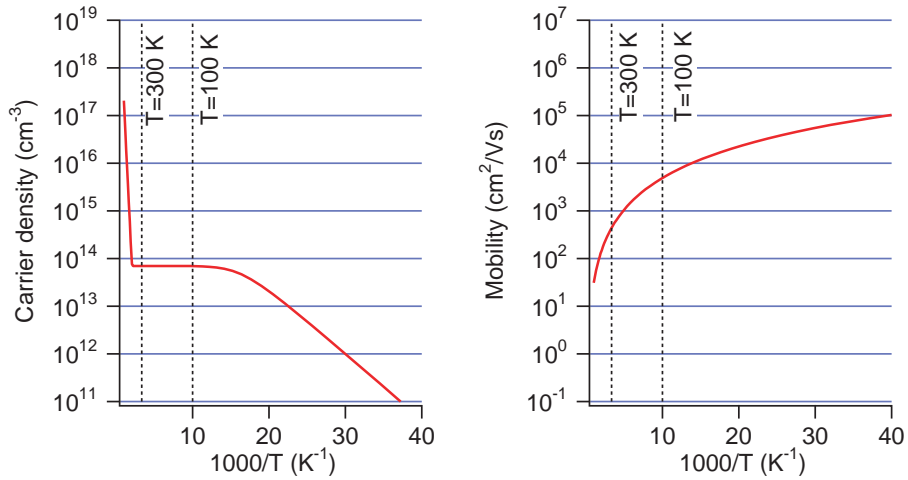


Figure 4.24: Model of the temperature dependence of the carrier density (left hand panel) and the mobility (right hand panel) in the bulk of sample A. The models on which this calculations are based are described in ref [180].

shown in figure 4.23, and is seen to accurately describe the high temperature measurements.

Finally, it can be noted that the low temperature saturation has a similar negative gradient to that of the high temperature measurements. Although it is not straightforward to calculate the carrier density and mobility at the surface, it could be assumed that the dominating mechanism here is the thermal increase in phonons, rather than any thermal change in the carrier density - exactly analogous to the bulk case.

The final step is to incorporate the surface state conductance into the model. This has been left out thus far because the bulk and space charge layers can be modeled using only the fundamental properties of the sample whereas the present understanding of surface transport phenomena does not allow a similar approach to be made for the surface conductance. Therefore the surface conductance requires an empirical approach:

From section 4.2.3.1 and in particular figure 4.13, it was inferred from the low temperature measurements that the surface conductivity of Si(111)(7×7) was $9 \times 10^{-9} \Omega^{-1}$. This can now be incorporated into the surface layer of the 3D numerical model.

Images of current density which were calculated using the above model are presented in figure 4.25. The left hand panels depict Sample A with the Si(111)(7×7) surface reconstruction at 100 K. The right hand panels depict the same sample and surface but at 300 K

In this case, the model comprises cubic elemental units of side length $1 \mu\text{m}$, and sufficient elements are included such that the current density at the boundaries is insignificant. 100 iterations were required for convergence, and this took approximately 10 hours to process.

Qualitatively, it can be seen from the images presented in figure 4.25 that the current density is confined to the surface layers at low temperature, but penetrates further into the bulk at higher temperatures. As discussed previously, this is not surprising since the space charge layer is much more conductive at higher temperatures, and thus the current can pass into the more conductive bulk.

4.3.3.2 Si(111)($\sqrt{3} \times \sqrt{3}$)Ag

The modeling procedure was repeated for the Si(111)($\sqrt{3} \times \sqrt{3}$)Ag samples. In this case, there is more uncertainty in the model since the pinning of the Fermi level at the surface is unclear. Although this results in larger uncertainties in the modeled conductances, the general trend is the same regardless of the estimation of E_{sf} used. Therefore, it is still interesting to apply the model.

Using a mid-range estimate of $E_{sf} = 0.26 \text{ eV}$ from ref [145], the space charge layer is found to be a relatively weak hole-depletion layer at low temperatures and a weak hole-accumulation layer at room temperature. A quantitative estimate of the 4 point conductance from the numerical 3D model presented previously is plotted in figure 4.26.

From the figure, it is clear that there is no agreement between the model and the measured data. The space charge layer and bulk conductance is almost always significantly less than the measured conductance - especially at high and low temperatures. The model was repeated for the available range of estimates of E_{sf} , and a reasonable fit to the measured conductance could not be made.

Since the model does not include the surface component of the conductance, the only simple explanation is that the measured conductance is always surface dominated, and thus the bulk and space charge layer contributions are irrelevant. This is not entirely surprising since the same conclusion was drawn from the surface covered with silver islands in sections 4.2.3.2 and 4.3.2.1, and the measured conductivities are of similar magnitudes (relative to the bulk and space charge conductances).

The interesting point now is to ascertain the reason for the observed transition in the measured conductance. At first glance, this transition appears to be similar to that seen in the measurements of Si(111)(7×7) shown in figure 4.13. However, closer inspection reveals that the transition occurs over a much smaller temperature range, and that there is some interesting structure

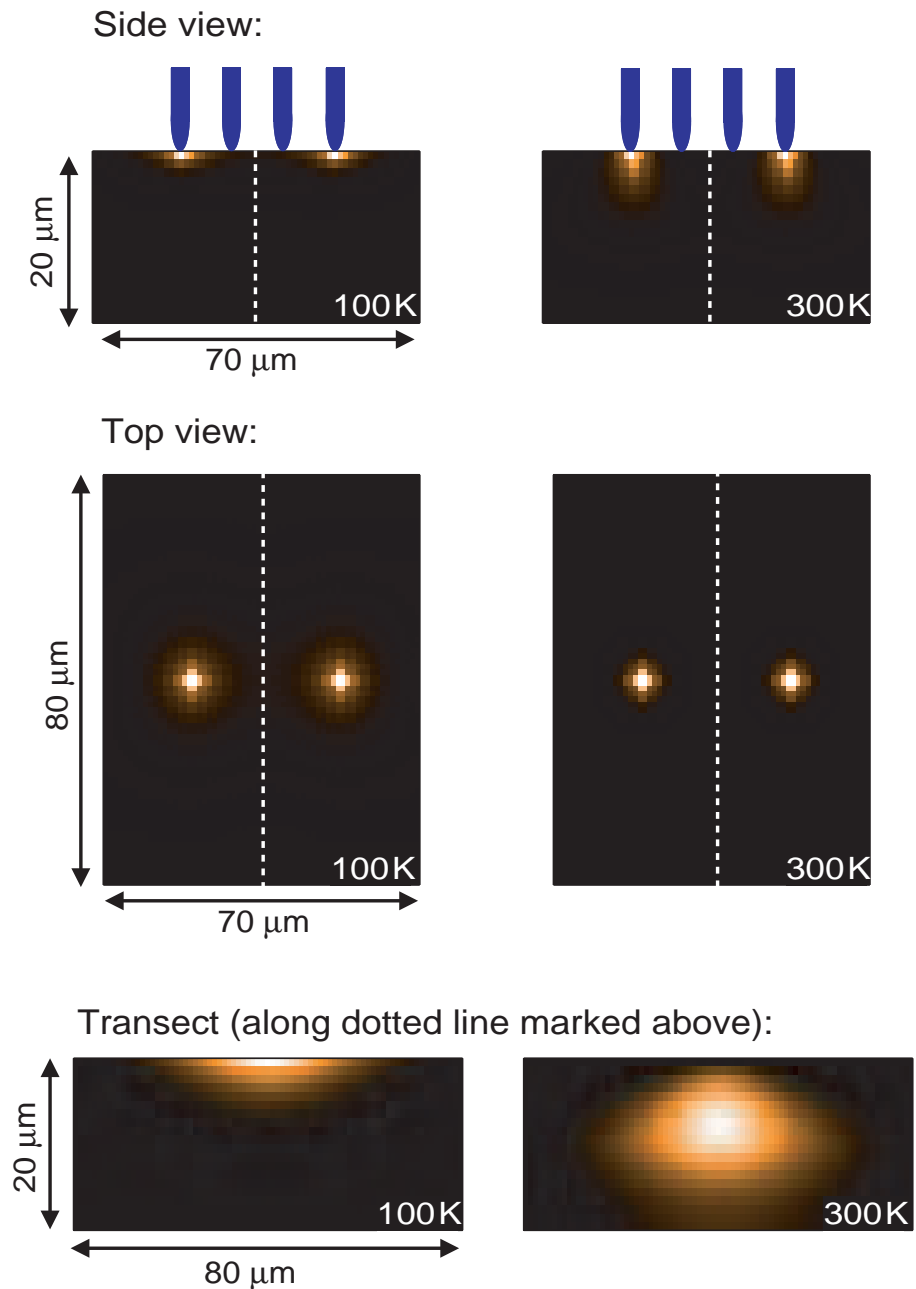


Figure 4.25: Images of current density from the numerical 3D solution of Poisson's equation. The upper panels show a cross-section along the axis of the 4 point probe, the middle panels show the view of the surface and the lower panels show a transect through the perpendicular bisector of the probe axis. The individual panels use different intensity scales for current density.

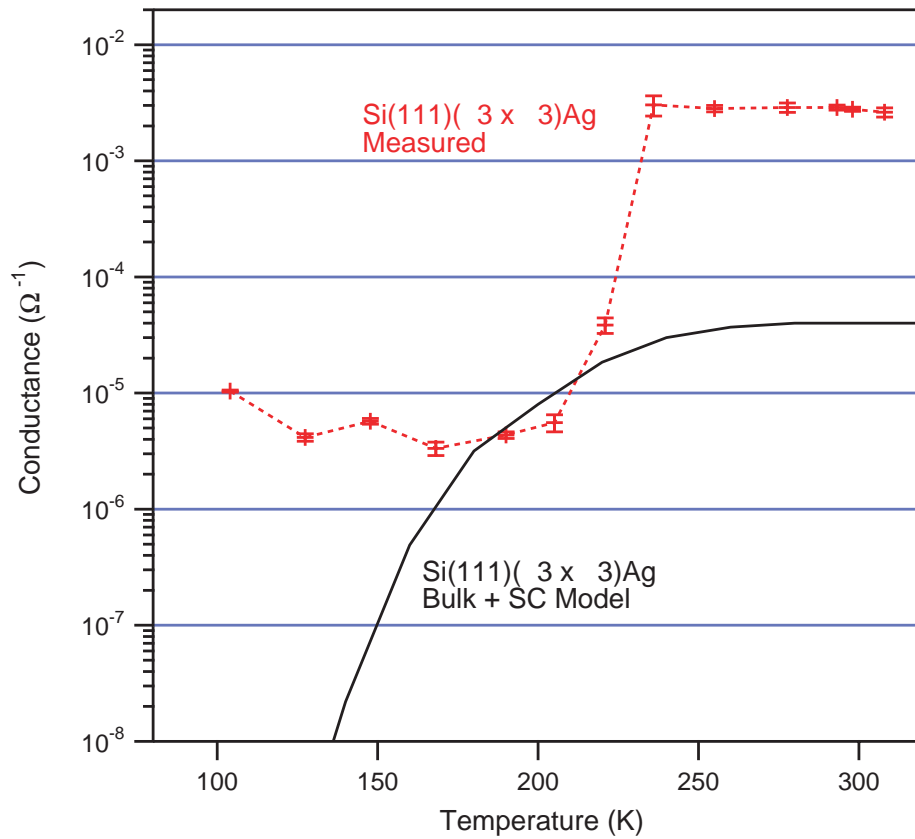


Figure 4.26: Graph of the modeled and measured conductance of the Si(111)($\sqrt{3} \times \sqrt{3}$)Ag surface. The model fails to describe the sharp transition seen in the measured data. Since the model does not include the surface contribution to the measured conductance, this transition is ascribed as being due to a sharp change in the surface conductivity.

in the low temperature range. In the measurements of the (7×7) surfaces, the low temperature measurements follow a simple power dependency within the bounds of experimental error, but that is not the case here.

These observations are indicative of a surface phase transition. i.e. the measurements are always surface dominated, but the value of the surface conductance displays a strong temperature dependence. Such a phase transition has been reported for this surface from a variety of techniques (see section 4.2.1.3), and although the transition temperature and indeed the nature of the transition is still debated, it is not surprising that it has a dramatic influence on the surface conductivity.

A further point to consider is that these measurements were found (in section 4.2.3.3) to be not exactly repeatable. It has been reported that the properties of the surface are significantly affected by the addition of Ag atoms slightly beyond an exact monolayer coverage. Since this is difficult to control precisely, it is possible that this accounts for the differences in the measurements. This provides further evidence for the measurements being surface dominated, and may in fact explain the differences in surface properties reported elsewhere - namely the room temperature surface conductivity and the transition temperature from other techniques [121, 122, 131, 148].

There are also many other possible explanations for the differences in the reported transition temperature, for example the measured transition temperature is dependent on the technique used: Consider a temperature at which the surface is partly exhibiting regions of the low and high temperature phases simultaneously. With a 4 point probe, the measurement depends on which phase forms a percolating network, whilst electron diffraction techniques are most sensitive to the phase which covers the largest area with a coherent phase. For example, if the surface is covered equally by HCT and IET domains, then the HCT phase will be seen most predominantly since the IET domains are divided into two possible geometries (usually named IET+ and IET-).

4.4 Conclusion

Measurements have been made on several different surface preparations of Si(111). In order to understand these measurements it is necessary to quantitatively model the temperature dependent behaviour of the bulk and space charge regions. Without accurately modeling the behaviour of the space charge layer, it is difficult - if not impossible - to determine the contribution of the bulk and space charge layers to the measured conductance. This may explain some of the disagreement in previous reports of the surface con-

ductivity of Si(111)(7×7).

The study of the clean (7×7) surface has shown a strong temperature dependance between 170 K and 230 K. Above this temperature range, the measured conductance is shown to be dominated by the bulk, whereas in the low temperature regime, the measured conductance is surface dominated. Both of the limits have a slight negative gradient which is consistent with the bulk and surface conductivities being influenced by thermal decreases in the carrier mobility. The surface conductivity is estimated at $9 \times 10^{-9} \Omega^{-1}$, which indicates that the surface is a poor metal - perhaps close to a metal-insulator transition.

It has been suggested that steps on the surface could have a dramatic influence on the surface conductivity. In order to address this, the Si(111)(7×7) surface has been studied with a range on step densities. It was found that the steps increase the conductivity, with the highest step density (30 monatomic steps per μm) corresponding to an increase in the surface conductivity of $\approx \times 50$ relative to the nominally step free surface.

The Si(111)($\sqrt{3} \times \sqrt{3}$) surface has also been studied. Although the temperature dependent conductance is qualitatively similar to that of the (7×7) surface, it has been shown that the observed behaviour cannot be due to changes in the bulk and space charge conductivities. Instead, the observed temperature dependence is believed to be due to a surface phase transition. The room temperature surface conductivity is estimated as $(6.1 \pm 0.3) \times 10^{-4} \Omega^{-1}$, which is in agreement with the previous reports for this surface.

Measurements on a percolating network of silver islands on the Si(111)(7×7) surface have also been performed. The growth mode and film thickness were estimated using a simple simulation. The measured conductance of this surface was found to be always surface dominated. Although the conductivity was found to be around an order of magnitude less than one would expect for bulk silver, the temperature dependance was found to be similar to that of bulk silver.

Chapter 5

Summary and outlook:

5.1 Overview of Present work

The main focus of this project has been on increasing the understanding of the transport properties of surfaces since this is lacking in the current understanding of surface physics. However, attention has also been paid to some of the factors which influence the surface conductivity such as the geometric and electronic properties of the surface. The conclusions from the present work are summarized in the following sections.

5.1.1 The Surface Geometric Structure

In chapter 2, LEED-IV measurements of the Bi(111) surface were presented. By comparison with calculations, it was shown that the surface structure is close to that of the truncated bulk, with small temperature dependent relaxations in the spacings of the first and second inter-layer distances. Although these findings are consistent with an intuitive understanding of the surface, they are in sharp contrast to the enormous relaxations reported previously.

From these measurements, it was also possible to deduce the R.M.S. vibrational amplitudes and their temperature dependence. The agreement between theory and calculations was excellent.

5.1.2 The Surface Electronic Structure

In chapter 3, ARUPS measurements of the Bi(111) surface were presented. By considering the spin-split nature of the surface, and by careful temperature dependent measurements of the Fermi level crossing of the electron pocket, it has been possible to exclude the existence of the suggested charge density wave on this surface.

Careful analysis of the temperature dependent MDC linewidth has allowed an improved estimation of the electron-phonon mass enhancement parameter to be made. This was calculated as $\lambda = 0.40 \pm 0.05$ which is significantly smaller than the value of $\lambda = 2.3 \pm 0.2$ reported by Ast and Höchst [24].

5.1.3 Transport Measurements

In chapter 4, the development of the multi-point probe instrument was discussed and measurements and models of surface conductivity were presented. In particular, Si(111) was studied; the characteristic (7×7) reconstructed surface was measured, and the surface conductivity was found to be extremely poor (around $10^{-9} \Omega^{-1}$, with a weak temperature dependence that was attributed as being due to phonon interactions). This is consistent with the surface being a very poor metal, or perhaps close to a Mott-Hubbard metal-insulator transition. At higher temperatures, the measured conductivity undergoes a transition of several orders of magnitude, and by modeling the behaviour of the space charge region, this was attributed as being due to the thermally increased conductivity of the hole depletion layer. Thus at high temperatures, the measured conductivity is consistent with the nominal bulk conductivity of the sample.

Silver was deposited onto the Si(111) surface. At room temperature, the silver was found to form a percolating network of islands with a preferred height of 5 atomic layers. The temperature dependent conductivity of this film was found to be similar to that of bulk silver, but around an order of magnitude less.

By annealing the above film, the Si(111) $(\sqrt{3} \times \sqrt{3})$ Ag surface was formed. The measurements of conductivity were found to be surface dominated across the studied temperature range (100 to 300 K). The surface conductivity was found to undergo an interesting transition at around 200 K and this was attributed to the geometric phase transition which has been reported elsewhere.

Vicinally cut Si(111) (7×7) was also studied. The surface conductivity was found to be enhanced by more than an order of magnitude relative to a nominally step free surface.

5.2 The Outlook

Meaningful discussions of the future are difficult, therefore this section concentrates instead on some preliminary measurements that have been made on more exotic materials. The materials are of great applied and fundamental interest, and would be worth considering for future study.

In addition, some possible practical improvements that could be made in order to increase the usefulness of the instruments are discussed.

5.2.1 Novel Surfaces for Future Study

Since the technique for studying the surface transport properties is relatively new, it has so far only been used to perform measurements on fundamental materials; a semi-conductor and a semi-metal.

Measurements of the electronic structure of more complex materials have been performed and reveal that it would also be interesting to study the transport properties of such materials.

5.2.1.1 Bismuth

Although bismuth is considered to be a poor conductor, the bulk resistivity of $1.3 \times 10^{-8} \Omega \text{ cm}$ [35] is many orders of magnitude lower than that of a typical semi-conductor (*cf.* "Sample A" which has a bulk resistivity of $190 \Omega \text{ cm}$). This gives rise to several practical challenges. In particular, consider the I-V curves from SI(111) shown in figure 4.12. Using a current range of $\pm 500 \text{ nA}$, the expected voltage change (assuming that the measurement is bulk sensitive) is $\approx \pm 1 \times 10^{-8} \text{ V}$ for a $10 \mu\text{m}$ probe (see equation 4.10).. In the current set-up, this is significantly smaller than the noise.

In order to reduce this problem, a larger current range can be studied. For example, using the present setup, the maximum current of $\pm 100 \mu\text{A}$ would give a potential change of $\approx \pm 2 \times 10^{-6} \text{ V}$. However, this is still small relative to the noise and would make it very difficult to see any structure in the measurements at small currents.

Another approach is to use smaller probes. Decreasing the probe size to $1 \mu\text{m}$ corresponds to an increase of $\times 10$ in the measured resistance. Also, by using measuring the dependence of the measured resistance on the probe spacing, it should be possible to see whether the sample is conducting through the surface or bulk (see equations 4.7 and 4.10).

Preliminary conductivity measurements on the (110) and (111) surfaces of bismuth have been performed using a 12 point probe. This probe offers spacing from 1.5 to $18 \mu\text{m}$. By statistically reducing the noise as much as possible, it was possible to show that the measured room temperature conductances showed good agreement with the expected bulk values. The spacing dependence was also consistent with the measurements being bulk dominated. Within experimental error, the I-V curves were linear across the entire current range. The signal to noise ratio was insufficient to allow any further inferences to be made.

It would be of great interest to further these measurements using smaller (and thus more surface sensitive) probes. Attempts to further reduce the experimental noise are also required. Low temperature measurements would also be of interest, but these will be even more difficult to perform since the noise in the measurements has been observed to increase at low temperatures.

5.2.1.2 Organic Semiconductors

Measurements of Si(111) surfaces have already been performed successfully. In fact, the 4 point probe with its current range of probe spacings appears to be ideally suited to measurements on semiconducting substrates with interesting surface modifications. One possibility for future study is into the realm of organic semiconductor, or more specifically organic semiconducting films on well studied semiconducting substrates.

It has recently been shown that the details of the substrate and surface preparation can be used to control the geometric and electronic properties at such semiconductor interfaces [10, 182, 183][X]. This can be used to select whether or not a space charge layer exists which can insulate the bulk and thus select the surface sensitivity of the 4 point probe.

The electronic properties of these semiconductors can commonly be subtly changed by chemical modification. For example, the central metal ion in the phthalocyanine molecule can be substituted [9][IX] and thus the conductivity can be changed by up to four orders of magnitude [184]. This makes them potentially useful in opto-electronic devices such as light emitting diodes [8][VIII].

The perylene derivatives such as PTCDA (Perylene-3,4,9,10-TetraCarboxylic-3,4,9,10-DiAnhydride) also display similar properties [11][XI], and like the metal phthalocyanines, they are large planar molecules which can be grown as ordered thin films. The molecular orientation relative to the substrate has been shown to be strongly dependent on the surface preparation and film thickness [185, 186], Thus by carefully controlling the surface preparation, interesting variations in the geometric structure of the overlayer can be achieved.

Therefore, since much is already known about the geometric and electronic properties of these films, it would be interesting to complete the study by investigating the influence of such modifications on the transport properties.

5.2.1.3 High T_c Superconductors

The mechanism of conductivity in superconductors with high critical temperatures (T_c) remains one of the great unsolved questions in solid state physics.

Perhaps we can improve our understanding by studying high T_c superconductors in reduced dimensions, and by studying the changes in both the electronic structure and transport properties at the transition temperature.

In fact several interesting possibilities exist; for example by evaporation, one can change the dopant concentration at the surface whilst measuring the transport properties and electronic structure. The question of dopants is especially interesting; it is generally assumed that increasing the dopant concentration not only increases the carrier density, but also results in an increase in electron-impurity scattering, and thus there is an optimal doping concentration [187]. A similar effect is seen in semiconductors, and one solution is to use modulation doping: Although the conductivity close to the overdoped areas is locally reduced because of the decreased mean free path, the overall conductivity is somewhat enhanced because of the additional delocalised extrinsic carriers.

Another interesting question is that of coherence length; superconductivity is usually described in terms of Cooper pair conduction, i.e. two carriers which are coherent over a characteristic length. The smallest 4 point probes currently available are on a scale comparable to the coherence length of a Cooper pair, thus it will soon be possible to apply a potential difference on a superconducting surface on a lengthscale that is small enough to only affect individual carriers. This could help to answer fundamental questions on the behaviour of individual carriers and on Cooper pair coherence.

One practical problem with conductivity measurements on superconducting materials is that the bulk conductance may dominate any surface effects. Thus, as well as thin superconducting films being of fundamental interest, it may become necessary to measure on such films grown on poorly conducting substrates. This requires being able to produce superconducting thin films. One possibility is MgB_2 , which is known to be superconducting in the bulk and has successfully been grown as thin films on the $\text{Mg}(0001)$ surface [188]. K_3C_{60} is also a possibility, it can be grown as an ordered thin film on the $\text{Ag}(111)$ surface, and in the bulk it undergoes a superconducting transition at 18 K [189, 190]. This is discussed in more detail in the following section.

5.2.1.4 Potassium Doped C_{60} Films

K_nC_{60} structures present a number of challenges, both theoretically and experimentally: Orientational disorder, temperature dependent phase transitions, weak molecular interaction, strong electron-phonon interactions and the very small Brillouin zone have combined effects which are difficult to distinguish.

Preliminary measurement of the electronic structure of K_3C_{60} and K_6C_{60} have been carried out. A brief summary of these measurements is given below,

but a more thorough treatment can be found in references [6][VI] and [7][VII]. Although these films have many similarities, there are also some striking differences:

The thin films of K_nC_{60} were prepared on Ag(111). The films were prepared using the method of "vacuum distillation" described by Poirier [191]. Although this preparation was quite complex, the K_3C_{60} and K_6C_{60} films were repeatedly prepared successfully.

Temperature dependent ARUPS measurements of K_6C_{60} have been performed from which several interesting conclusions have been drawn. The low temperature measurements indicate that the linewidths of the Highest Occupied Molecular Orbital (HOMO) and Lowest Unoccupied Molecular Orbital (LUMO) features are significantly broader than one would expect from a one-electron band dispersion, but apart from this, the experimental data show good agreement with the calculations of Erwin and Pederson [192]. From the temperature dependent linewidths, the electron-phonon mass enhancement parameter (λ) has been estimated as $\lambda_{LUMO} = 1.08 \pm 0.03$ and $\lambda_{HOMO} = 1.18 \pm 0.03$ for the LUMO and HOMO features respectively. However, there is still some uncertainty in the present understanding regarding the significance of the contribution of the K^+ phonons.

Unlike the insulating K_6C_{60} film, K_3C_{60} is thought to be a strongly correlated metal [193] and undergoes a superconducting transition at around 18 K [189, 190]. One of the factors that is believed to govern the transition temperature is the strength of the electron-phonon coupling. In the case of K_3C_{60} structures, the spectrum of intra-molecular vibrations extends to high energies (approximately 200 meV), and gives rise to strong electron phonon coupling. Since the width of the valence and conduction bands is significantly lower than the Hubbard energy [189, 194], electron correlations are also expected to influence the transition temperature.

Also in contrast to K_6C_{60} , the calculations and measurements show a large discrepancy. For example, the dispersion in the $\bar{\Gamma}-\bar{M}-\bar{\Gamma}$ direction is significantly less than the predicted value of 200 meV [192], in fact it appears to be about half of this value. It has also been shown that the electronic structure is very sensitive to the C_{60} orientation, so perhaps a temperature dependent re-ordering complicates the situation.

In conclusion, both the K_3C_{60} and K_6C_{60} surfaces are intriguing. Although preliminary measurements of the electronic structure are interesting, high quality measurements of the electronic structure are still lacking. A complimenting study of the transport properties of these surfaces may help to improve the present level of understanding.

5.2.1.5 Structured Surfaces and Devices

Another interesting application of the 4 point probe, is to directly measure the conductivity of small scale objects, such as molecular electronic components, carbon nanotubes and so forth. Although this has already been attempted by Lin *et al.* [195] amongst others, the technique is very much still in its infancy. By improving the lateral repeatability of our 4 point probe position, and by adding a more powerful microscope - ideally an electron microscope - similar feats could be attempted with our instrument.

5.2.2 Instrumental Limitations

5.2.2.1 Limitations to the Measurements of Conductivity

One of the major fundamental limitations of the instrument is the probe size. As probes become smaller, they become more susceptible to mechanical damage, they also become more difficult to resolve optically. The current limit is a probe spacing of around $1\ \mu\text{m}$ since probes significantly smaller than this would be impossible to resolve with the current microscope. However, such small probes are also proving difficult to fabricate. The latest developments are concentrated on monocantilevers with multiple contacts. This alleviates the problem somewhat since the monocantilevers can be fabricated to be large enough to resolve, whilst the electrical contacts can become as small as necessary. Such monocantilevers also have significantly more mechanical strength than the equivalent 4 cantilever probe.

Another significant improvement would be to use instrumental feedback to control the approach of the probe; the current optical feedback will always have limitations, whereas instrumental feedback could allow a faster and safer automatic approach to be made, and would no longer require a microscope.

There will always be a lower limit to the probe spacing that can be achieved. As shown in equation 4.13, this corresponds to the limit of surface resistance (relative to bulk resistance) that can be measured. Thus, for superconducting bulk samples, it may become impossible to measure the surface resistance. Perhaps the only solution to this is to increase the resistance of the bulk - for example by producing the same surface structure on a poorly conducting substrate.

It is interesting to measure the dependence of the probe orientation relative to that of the sample. This currently requires similar samples being mounted at different orientations on the sample holder since there is no possibility to rotate the sample holder in the measuring stage. This always adds some uncertainty since small differences in the surface preparation could be significant.

It would be advantageous to have a rotatable sample stage - especially for studying structured surfaces.

One of the problems encountered with recent measurements is the issue of probe misalignment; the probes are easily damaged when there is a difference in the horizontal alignment of the probe and the sample. Currently, it is required to open the chamber in order to correct this, and with smaller samples it can be very difficult to make a correct alignment. The problem could be alleviated by making the sample position adjustable in vacuum.

Recent work by Hasegawa *et al.* [196] has shown that it is interesting to make real-time measurements whilst the surface is modified (in their case during the evaporation of silver). In principle, the same setup could be employed in our system. For example, this would allow the percolation threshold of island coverages to be easily seen.

Finally, the ongoing issue of reliability needs to be addressed. The current setup requires frequent repairs and modifications. The smaller probes can be easily broken, and in order to replace them, the chamber must be opened. After replacing the probe, the sample has been exposed to air and thus needs to be prepared again. This makes it difficult to make a long series of measurements using the same probe and surface preparation. This will become increasingly important when measuring on samples which are difficult to prepare - for example MgB_2 and K_nC_{60} .

There are several possible solutions to this problem: For example, making a probe that can be replaced through a loadlock (such as one finds in commercial STM systems) would reduce the need for opening the chamber. Alternatively, having a second chamber in which to store clean samples during venting would be advantageous. Perhaps the ideal solution is to use a vacuum transfer case which allows in-vacuum transfer to other chambers since this also increases the range of sample preparation and diagnostic techniques available.

5.2.2.2 Instrumental Limits in Other Measurements

There is always a need to improve the energy and momentum resolutions in ARUPS. Whilst the measurements presented in chapter 3 are made with relatively high resolution, there is a need to improve this when studying phenomena which occur on a small energy scales such as electron-phonon coupling.

In these measurements, the experimental resolution is primarily limited by the spectrometer. However, spectrometers are currently becoming available with resolutions in the sub-meV range. After upgrading to such a spectrometer, the spacial- and energy- resolutions of the synchrotron light source will become more significant.

Therefore, an improved spectrometer, light source and perhaps improved

data processing would allow phenomena on small energy scales, and with small effective masses to be probed in more depth.

5.3 Conclusion

In conclusion, measurements of geometric and electronic surface structure have been made using well established techniques. By comparison with calculations, some interesting surface properties such as the surface relaxations, vibrational amplitudes, Debye temperatures, electron-phonon coupling strengths and so forth, have been found. The absence of a charge density wave is also apparent.

Measurements of surface conductivity have also been performed. However since the technique is less well established, a significant amount of development was required. Also, previously reported attempts at similar measurements have suffered from inaccurate interpretation. By modifying the bulk and surface properties independently, the surface and bulk sensitivity of the measurements can be observed. A simple model of the surface and shallow bulk properties was used to confirm these observations. Once the measurements are interpreted, some interesting effects can be seen; for example the role of electron-phonon coupling, the doping effect of step edges and the influence of geometry altering surface phase transitions.

The combination of such measurements increases our understanding of the factors which influence surface conductivity. Such measurements could now be performed on superconducting thin films, or anisotropic organic semiconductors in an attempt to improve our understanding of the mechanism of conduction. This is especially interesting in the case of high T_c superconductors since much is lacking in the current understanding.

Chapter 6

Acknowledgements

6.1 General Comments

First and foremost, I would like to thank Philip Hofmann for his guidance during this project.

I would like to acknowledge the assistance of Zeshen Li and Søren Vrønning Hoffmann for helping to solve many technical problems. Also, I would like to acknowledge the assistance of the ISA staff and the mechanical workshop.

I would like to thank our colleagues from Capres A/S; especially Peter Petersen, Mette Balslev and Jesper Hansen and from Denmark's Technical University; especially Peter Bøggild and Lauge Gammelgaard for the many useful discussions on 4 point probes, and for supplying the countless number of probes used during this project.

Finally, I would like to thank Nykola Jones for proof reading this thesis, and all of my friends and colleagues for their support during this project.

The project has been funded as part of the "MiNaP" innovation consortium. For more details see www.minap.dk.

6.2 Specific Acknowledgements

The work presented in this thesis covers a wide range of measurements on a wide range of instruments, as well as theoretical studies and so forth. Therefore, a number of important collaborations have been made and supporting work has been carried out (either partially or wholly) by helpful colleagues.

In this section, one can find a summary of all the contributions to this work that were not made by myself. To the best of my knowledge, this list is comprehensive.

6.2.1 Chapter 2: The Surface Geometric Structure

The LEED-IV measurements made in this chapter were made jointly with Harry Mönig. The calculations were performed by Jeibling Sun.

6.2.2 Chapter 3: The Surface Electronic Structure

The ARUPS measurements of bismuth were performed with the assistance of Casper Kirkegaard.

6.2.3 Chapter 4: Transport Measurements

The original 4 point probe setup was constructed by Torben Hansen. The improvements to the measuring software were made with the help of Casper Kirkegaard, Some of the data was collected jointly with Torben Hansen and Jesper Kallehauge.

The in-vacuum flux-free solder connections to the probe were made by Jesper Djuurhuus from GPV Electronics A/S.

6.2.4 Chapter 5: Conclusions and Outlook

The measurements on K_nC_{60} , and on organic semiconductors were performed jointly with many collaborators. I would therefore like to acknowledge the assistance of all of the co-authors of publications [6] [VI] to [11] [XI].

List of Abbreviations

Below is a glossary containing the abbreviations used in this thesis, along with a definition and the page number where each term is first used.

ADC	Analogue to Digital Convertor	43
AES	Auger Electron Spectroscopy	6
ARUPS	Angular Resolved Ultra Violet Photoemission Spectroscopy	13
CDW	Charge Density Wave	13
DAC	Digital to Analogue Convertor	42
EDC	Energy Distribution Curve	17
EELS	Electron Energy Loss Spectroscopy	47
FWHM	Full Width Half Maximum	18
HCT	Honeycomb Chained Triangle	49
HOMO	Highest Occupied Molecular Orbital	95
IET	In-Equivalent Triangle	49
IPES	Inverse Photo-Emission Spectroscopy	16
LEED	Low Energy Electron Diffraction	5
LEED-IV	Low Energy Electron Diffraction - Intensity versus Voltage	6
LUMO	Lowest Unoccupied Molecular Orbital	95
MDC	Momentum Distribution Curve	17
NMR	Nuclear Magnetic Resonance	47

RGA	Residual Gas Analysis	42
RHEED	Reflection High Energy Electron Diffraction	49
RMS	Root Mean Square	9
SOC	Spin Orbit Coupling	22
STM	Scanning Tunneling Microscopy	5
STS	Scanning Tunneling Spectroscopy	16
TEM	Transition Electron Microscope	28
TSP	Titanium Sublimation Pump	38
VBM	Valence Band Maximum	76

Bibliography

- [1] [I] H. Mönig, J. Sun, M. Koroteev, G. Bihlmayer, J. Wells, E. V. Chulkov, K. Pohl, and Ph. Hofmann. The structure of the (111) surface of bismuth: LEED analysis and first principles calculations. *Phys. Rev. B*, 72:085410, 2005.
- [2] [II] J. E. Gayone, C. Kirkegaard, J. W. Wells, S. V. Hoffmann, Z. Li, and Ph. Hofmann. Determining the electron-phonon mass enhancement parameter λ on metal surfaces. *Applied Physics A*, 80:943–949, 2005.
- [3] [III] T. K. Kim, J. Wells, C. Kirkegaard, Z. Li, S. V. Hoffmann, J. E. Gayone, I. Fernandez-Torrente, P. Haberle, J. I. Pascual, K. T. Moore, A. J. Schwartz, H. He, J. C. H. Spence, K. H. Downing, S. Lazar, F. D. Tichelaar, S. V. Borisenko, M. Knupfer, and Ph. Hofmann. Evidence against a Charge Density Wave on Bi(111). *Phys. Rev. B*, 72(8):085440, 2005.
- [4] [IV] Justin W. Wells and Keith Birkinshaw. A matrix approach to resolution enhancement of XPS spectra by a modified Maximum Entropy method. *Journal of Electron Spectroscopy and Related Phenomena*, 152:37–43, 2006.
- [5] [V] J.W. Wells, J.F. Kallehauge, T.M. Hansen, and Ph. Hofmann. Thermal switching and surface conductivity of Si(111)(7x7). *submitted to PRL*.
- [6] [VI] A. Goldoni, C. Cepek, L. Petaccia, S. Lizzit, J. E. Gayone, J. Wells, and Ph. Hofmann. Electronic structure and many body effects in K_3C_{60} and K_6C_{60} . *to be published*.

- [7] **[VII]** A. Goldoni, L. Petaccia, G. Zampieri, S. Lizzit, C. Cepek, E. Gayone, J. Wells, and Ph. Hofmann. Evidence for bandlike dispersion in $K_6C_{60}(110)$ films. *Phys. Rev. B*, 74(4):045414, Jul 2006.
- And*
- A. Goldoni, L. Petaccia, G. Zampieri, S. Lizzit, C. Cepek, E. Gayone, J. Wells, and Ph. Hofmann. Band-like dispersion in the photoemission spectra of $K_6C_{60}(110)$ films. *AIP Conference Proceedings*, 786:3-7, Jul 2005.
- [8] **[VIII]** D. A. Evans, H. J. Steiner, A. R. Vearey-Roberts, A. Bushell, G. Cabailh, S. O'Brien, J. W. Wells, I. T. McGovern, V. R. Dhanak, and T. U. Kampen. Synchrotron radiation studies of inorganic-organic semiconductor interfaces. *Nuclear Instruments and Methods in Physics Research Section B: Beam Interactions with Materials and Atoms*, 199:475–480, 2003.
- [9] **[IX]** J. W. Wells, G. Cabailh, D. A. Evans, S. Evans, A. Bushell, and A. R. Vearey-Roberts. An XPS study of the interaction between tin(II) phthalocyanine and polycrystalline iron. *Journal of Electron Spectroscopy and Related Phenomena*, 141:67–72, 2004.
- [10] **[X]** A. R. Vearey-Roberts, H. J. Steiner, S. Evans, I. Cerrillo, J. Mendez, G. Cabailh, S. O'Brien, J. W. Wells, I. T. McGovern, and D. A. Evans. Growth and morphology of SnPC films on the S-GaAs(001) surface: a combined XPS, AFM and NEXAFS study. *Applied Surface Science*, 234:131–137, 2004.
- [11] **[XI]** T U Kampen, G Gavrilu, H Méndez, D R T Zahn, A R Vearey-Roberts, D A Evans, J Wells, I McGovern, and W Braun. Electronic properties of interfaces between perylene derivatives and GaAs(001) surfaces. *Journal of Physics: Condensed Matter*, 15(38):S2679–S2692, 2003.
- [12] F. Jona. Low-energy electron diffraction study of surfaces of antimony and bismuth. *Surface Science*, 8:57–76, 1967.
- [13] V. S. Édel'man, D. Y. Sharvin, I. N. Khlyustikov, and A. M. Troyanovskii. STM revealing of twin microlayers with quantized width on cleaved bismuth surface. *Europhysics Letters*, 34:115–120, 1996.
- [14] Christian R. Ast and Hartmut Höchst. Electronic structure of a bismuth bilayer. *Phys. Rev. B*, 67:113102, 2003.

- [15] D. L. Adams, H. B. Nielsen, and M. A. Van Hove. Quantitative analysis of low-energy-electron diffraction: Application to Pt(111). *Phys. Rev. B*, 20(12):4789–4806, Dec 1979.
- [16] David L. Adams, V. Jensen, X. F. Sun, and J. H. Vollesen. Multilayer relaxation of the Al(210) surface. *Phys. Rev. B*, 38:7913, 1988.
- [17] David L. Adams. On the calculation of interlayer multiple-scattering in LEED *Journal of Physics C*, 16:6101, 1983.
- [18] J. B. Pendry. *Low Energy Electron Diffraction*. Academic Press, London, 1974.
- [19] M. A. Van Hove and S. Y. Tong. *Surface Crystallography by LEED*. Springer-Verlag, Berlin, 1979.
- [20] K. G. Ramanathan and T. M. Srinivasan. Specific heat of bismuth at liquid helium temperatures. *Physical Review*, 99:442, 1955.
- [21] C. Walfried, D. N. McIlroy, J. Zhang, P. A. Dowben, G. A. Katrich, and E. W. Plummer. Determination of the surface Debye temperature of Mo(112) using valence band photoemission. *Surface Science*, 363:296–302, 1996.
- [22] R. M. Goodman and G. A. Somorjai. Low-energy electron diffraction studies of surface melting and freezing of lead, bismuth and tin single-crystal surfaces. *J. Chem. Phys.*, 52:6325, 1970.
- [23] Christian R. Ast and Hartmut Höchst. Indication of charge-density wave formation on Bi(111). *Phys. Rev. Lett.*, 90:016403, 2003.
- [24] Christian R. Ast and Hartmut Höchst. Two-dimensional band structure and self-energy of Bi(111) near the $\bar{\Gamma}$ point. *Phys. Rev. B*, 66:125103, 2002.
- [25] Yi Liu and Roland E. Allen. Electronic structure of the semimetals Bi and Sb. *Phys. Rev. B*, 52:1566, 1995.
- [26] X. Gonze, J.-P. Michenaud, and J.-P. Vigneron. First-principles study of As, Sb, and Bi electronic properties. *Phys. Rev. B*, 41:11827–11836, 1990.
- [27] G. Jezequel, Y. Petroff, R. Pinchaux, and F. Yndurain. Electronic structure of the Bi(111) surface. *Phys. Rev. B*, 33:4352–4355, 1986.

- [28] G. Jezequel, J. Thomas, and I. Pollini. Experimental band structure of semimetal bismuth. *Phys. Rev. B*, 56:6620–6626, 1997.
- [29] J. Thomas, G. Jezequel, and I. Pollini. Photoemission study of the bulk and surface electronic structure of Bi(111). *Journal of Physics: Condensed Matter*, 11:9571–9580, 1999.
- [30] M. Hengsberger, P. Segovia, M. Garnier, D. Purdie, and Y. Baer. Photoemission study of the carrier bands in Bi(111). *The European Physical Journal B*, 17:603–608, 2000.
- [31] A. Tanaka, M. Hatano, K. Takahashi, H. Sasaki, S. Suzuki, and S. Sato. Growth and angle-resolved photoemission studies of bismuth epitaxial films. *Surface Science*, 433-435:647–651, 1999.
- [32] A. Tanaka, M. Hatano, K. Takahashi, H. Sasaki, S. Suzuki, and S. Sato. Bulk and surface electronic structures of the semimetal Bi studied by angle-resolved photoemission spectroscopy. *Phys. Rev. B*, 59:1786–1791, 1999.
- [33] Ch. R. Ast and H. Höchst. High-resolution photoemission mapping of the three-dimensional band structure of Bi(111). *Phys. Rev. B*, 70:245122, 2004.
- [34] Ph. Hofmann. The surfaces of bismuth: Structural and electronic properties. *Progress in Surface Science*, 81:191–245, 2006.
- [35] www.webelements.com.
- [36] F. Patthey, W.-D. Schneider, and H. Micklitz. Photoemission study of the Bi(111) surface. *Phys. Rev. B*, 49:11293–11296, 1994.
- [37] Ch. R. Ast and H. Höchst. Fermi surface of Bi(111) measured by photoemission spectroscopy. *Phys. Rev. Lett.*, 87:177602, 2001.
- [38] S. Hüfner. *Photoelectron spectroscopy*. Springer, Berlin, 3rd ed. edition, 2003.
- [39] E. W. Plummer and W. Eberhardt. Angle-resolved photoemission as a tool for the study of surfaces. *Advances in Chemical Physics*, 49:533–656, 1982.
- [40] S. D. Kevan, editor. *Angle-resolved photoemission*, volume 74 of *Studies in Surface Chemistry and Catalysis*. Elsevier, Amsterdam, 1992.

- [41] F. J. Himpsel. Angle-resolved measurements of the photoemission of electrons in the study of solids. *Advances in Physics*, 32:1–51, 1983.
- [42] C. S. Fadley. Angle-resolved X-ray photoelectron spectroscopy. *Progress in Surface Science*, 16:275–388, 1984.
- [43] R. Matzdorf. Investigation of line shapes and line intensities by high-resolution UV-photoemission spectroscopy - some case studies on noble-metal surfaces. *Surface Science Reports*, 30:153–206, 1998.
- [44] Ch. Søndergaard. *An Investigation of Surface Electronic Structure and Electron-Phonon Interaction by Angle-Resolved Photoemission Spectroscopy*. Ph.D.-thesis, University of Aarhus, 2001.
- [45] C. Kirkegaard, T. K. Kim, and Ph. Hofmann. Self-energy determination and electron-phonon coupling on Bi(110). *New Journal of Physics*, 7:99, 2005.
- [46] W. Eberhardt and E. W. Plummer. Angle-resolved photoemission determination of the band structure and multielectron excitations in Ni. *Phys. Rev. B*, 21:3245–3255, 1980.
- [47] B. Hellsing, A. Eiguren, and E. V. Chulkov. Electron-phonon coupling at metal surfaces. *Journal of Physics: Condens. Matter*, 14:5959–5977, 2002.
- [48] E. W. Plummer, Junren Shi, S.-J. Tang, Eli Rotenberg, and S. D. Kevan. Enhanced electron-phonon coupling at metal surfaces. *Surface Science Reports*, 74:251, 2003.
- [49] P. M. Echenique, R. Berndt, E. V. Chulkov, Th. Fauster, A. Goldmann, and U. Höfer. Decay of electronic excitations at metal surfaces. *Surface Science Reports*, 52:219, 2004.
- [50] Junren Shi, S.-J. Tang, Biao Wu, P. T. Sprunger, W. L. Yang, V. Brouet, X. J. Zhou, Z. Hussain, Z.-X. Shen, Zhenyu Zhang, and E. W. Plummer. Direct extraction of the Eliashberg function for electron-phonon coupling: a case study of Be(10 $\bar{1}$ 0). *Phys. Rev. Lett.*, 92:186401, 2004.
- [51] N. V. Smith, P. Thiry, and Y. Petroff. Photoemission linewidth and quasiparticle lifetimes. *Phys. Rev. B*, 47:15476–15481, 1993.
- [52] E. D. Hansen, T. Miller, and T.-C. Chiang. Observation of photoemission line widths narrower than the inverse lifetime. *Phys. Rev. Lett.*, 80:1766–1769, 1998.

- [53] S. LaShell, E. Jensen, and T. Balasubramanian. Nonquasiparticle structure in the photoemission spectra from the Be(0001) surface and determination of the electron self energy. *Phys. Rev. B*, 61:2371–2374, 2000.
- [54] J. E. Gayone, S. V. Hoffmann, Z. Li, and Ph. Hofmann. Strong energy dependence of the electron-phonon coupling on Bi(100). *Phys. Rev. Lett.*, 91:127601, 2003.
- [55] Yu. M. Koroteev, G. Bihlmayer, J. E. Gayone, E. V. Chulkov, S. Blügel, P. M. Echenique, and Ph. Hofmann. Strong spin-orbit splitting on Bi surfaces. *Phys. Rev. Lett.*, 93:046403, 2004.
- [56] G. Grüner. *Density waves in solids*, volume 89 of *Frontiers in physics*. Perseus Publishing, Cambridge, Massachusetts, 1994.
- [57] E. Tosatti. Surface states, surface metal-insulator transition, and surface insulator-metal transitions. In E. Bertel and M. Donath, editors, *Electronic surface and interface states on metallic systems*. World Scientific, Singapore, 1995.
- [58] Tetsuya Aruga. Charge-density waves on metal surfaces. *Journal of Physics: Condens. Matter*, 14:8393, 2002.
- [59] S. V. Hoffmann, C. Søndergaard, C. Schultz, Z. Li, and Ph. Hofmann. An undulator-based spherical grating monochromator beamline for angle-resolved photoemission spectroscopy. *Nuclear Inst. and Methods in Physics Research, A*, 523:441, 2004.
- [60] F.M. Smits. Measurement of sheet resistivities with the four-point-probe. *Bell System Technical Journal*, 37:711–718, 1958.
- [61] L.M. Valdes. Resistivity measurements on germanium for transistors. *Proceedings of the IRE*, pages 420–427, 1954.
- [62] I. Shiraki, F. Tanabe, R. Hobarra, T. Nagao, and S. Hasegawa. Independently driven four-tip probes for conductivity measurements in ultra-high vacuum. *Surf. Sci.*, 493:633, 2001.
- [63] T. Hansen. Tools for nanoscale conductivity measurements. PhD thesis, Technical University of Denmark, 2003.
- [64] D.R. Lide, editor. *CRC Handbook of Chemistry and Physics*. CRC Press Inc., 80th ed., 1999.

- [65] Richard Friend. Materials science: Polymers show they're metal. *Nature*, 441(7089):37–37, 2006.
- [66] R. E. Schlier and H. E. Farnsworth. Structure and adsorption characteristics of clean surfaces of germanium and silicon. *The Journal of Chemical Physics*, 30(4):917–926, 1959.
- [67] Walter A. Harrison. Surface reconstruction on semiconductors. *Surface Science*, 55:1–19, 1976.
- [68] G. Binnig, H. Rohrer, Ch. Gerber, and E. Weibel. 7×7 reconstruction on Si(111) resolved in real space. *Phys. Rev. Lett.*, 50(2):120–123, Jan 1983.
- [69] F. J. Himpsel. Structural model for Si(111)-(7×7). *Phys. Rev. B*, 27(12):7782–7785, Jun 1983.
- [70] E. G. McRae. Surface stacking sequence and (7×7) reconstruction at Si(111) surfaces. *Phys. Rev. B*, 28(4):2305–2307, Aug 1983.
- [71] P. A. Bennett, L. C. Feldman, Y. Kuk, E. G. McRae, and J. E. Rowe. Stacking-fault model for the Si(111)-(7×7) surface. *Phys. Rev. B*, 28(6):3656–3659, Sep 1983.
- [72] S. Y. Tong, H. Huang, C. M. Wei, W. E. Packard, F. K. Men, G. Glander, and M. B. Webb. Low-energy electron-diffraction analysis of the Si(111) 7×7 structure. *Journal of Vacuum Science and Technology A: Vacuum, Surfaces, and Films*, 6(3):615–624, May-Jun 1988.
- [73] I. K. Robinson, W. K. Waskiewicz, P. H. Fuoss, and L. J. Norton. Observation of strain in the Si(111) 7×7 surface. *Phys. Rev. B*, 37(8):4325–4328, Mar 1988.
- [74] K. Takayanagi, Y. Tanishiro, S. Takahashi, and M. Takahashi. Structure-analysis of Si(111)- 7×7 reconstructed surface by transmission electron-diffraction. *Surface science*, 164(2-3):367–392, Dec 1985.
- [75] John E. Northrup. Origin of surface states on Si(111)(7×7). *Phys. Rev. Lett.*, 57(1):154, Jul 1986.
- [76] Guo-Xin Qian and D. J. Chadi. Si(111)- 7×7 surface: Energy-minimization calculation for the dimer- $\sqrt{3}\times\sqrt{3}$ stacking-fault model. *Phys. Rev. B*, 35(3):1288–1293, Jan 1987.

- [77] Robert D. Meade and David Vanderbilt. Adatoms on Si(111) and Ge(111) surfaces. *Phys. Rev. B*, 40(6):3905–3913, Aug 1989.
- [78] Gary B. Adams and Otto F. Sankey. Ab initio molecular-dynamical relaxation applied to the silicon(111)- 5×5 surface reconstruction. *Phys. Rev. Lett.*, 67(7):867–870, Aug 1991.
- [79] I. Stich, M. C. Payne, R. D. King-Smith, J-S. Lin, and L. J. Clarke. Ab initio total-energy calculations for extremely large systems: Application to the Takayanagi reconstruction of Si(111). *Phys. Rev. Lett.*, 68(9):1351–1354, Mar 1992.
- [80] Karl D. Brommer, M. Needels, B. Larson, and J. D. Joannopoulos. Ab initio theory of the Si(111)- (7×7) surface reconstruction: A challenge for massively parallel computation. *Phys. Rev. Lett.*, 68(9):1355–1358, Mar 1992.
- [81] H. Lim, K. Cho, I. Park, J. D. Joannopoulos, and Efthimios Kaxiras. Ab initio study of hydrogen adsorption on the Si(111)- (7×7) surface. *Phys. Rev. B*, 52(24):17231–17237, Dec 1995.
- [82] Jeongnim Kim, Mei-Ling Yeh, Furrukh S. Khan, and John W. Wilkins. Surface phonons of the Si(111)- 7×7 reconstructed surface. *Phys. Rev. B*, 52(20):14709–14718, Nov 1995.
- [83] D. R. Alfonso, C. Noguez, D. A. Drabold, and S. E. Ulloa. First-principles studies of hydrogenated Si(111)- 7×7 . *Phys. Rev. B*, 54(11):8028–8032, Sep 1996.
- [84] E. Louis, F. Flores, F. Guinea, and C. Tejedor. Many-body effects in the (111)-silicon dangling-bond surface states. *Solid State Communications*, 44:1633–1636, 1982.
- [85] José Ortega, Fernando Flores, and Alfredo Levy Yeyati. Electron correlation effects in the Si(111)- 7×7 surface. *Phys. Rev. B*, 58(8):4584–4588, Aug 1998.
- [86] J. E. Rowe and H. Ibach. Surface and bulk contributions to ultraviolet photoemission spectra of silicon. *Phys. Rev. Lett.*, 32(8):421–424, Feb 1974.
- [87] D. E. Eastman, F. J. Himpsel, J. A. Knapp, and K.C. Pandey. Angle resolved photoemission studies of semiconductor bulk and surface states. *Inst. Phys. Conf. Ser.*, 43:1059, 1979.

- [88] G. V. Hansson, R. I. G. Uhrberg, and S. A. Flodstrom. Electronic structure of the Si(111) 7 x 7 surface studied by angle-resolved photoelectron spectroscopy. *Journal of Vacuum Science and Technology*, 16(5):1287–1289, 1979.
- [89] F. Houzay, G. M. Guichar, R. Pinchaux, P. Thiry, Y. Petroff, and D. Dagneaux. Angle-resolved photoemission of the Si(111) 7 x 7 surface. *Surface Science*, 99:28–33, 1980.
- [90] T. Yokotsuka, S. Kono, S. Suzuki, and T. Sagawa. Angle-resolved ultraviolet photoemission study of Si(111) 7 x 7 and 1 x 1 surfaces. *Solid State Communications*, 39:1001–1004, 1981.
- [91] F. J. Himpsel, D. E. Eastman, P. Heimann, B. Reihl, C. W. White, and D. M. Zehner. Electronic structure of the annealed Ge(111) and Si(111) surfaces: Similarities in local bonding. *Phys. Rev. B*, 24(2):1120–1123, Jul 1981.
- [92] R. I. G. Uhrberg, G. V. Hansson, J. M. Nicholls, P. E. S. Persson, and S. A. Flodström. Photoemission study of the surface and bulk electronic structures of Si(111)7×7 and Si(111) $\sqrt{3} \times \sqrt{3}$:Al. *Phys. Rev. B*, 31(6):3805–3810, Mar 1985.
- [93] H. Neddermeyer, U. Misse, and P. Rupieper. Photoemission study of the surface electronic structure of Si(111) 1 x 1 and Si(111) 7 x 7. *Surface Science*, 117:405–416, 1982.
- [94] J. E. Demuth, W. J. Thompson, N. J. DiNardo, and R. Imbihl. Photoemission-based photovoltage probe of semiconductor surface and interface electronic structure. *Phys. Rev. Lett.*, 56(13):1408–1411, Mar 1986.
- [95] Per Martensson, Wei-Xin Ni, Göran V. Hansson, J. Michael Nicholls, and Bruno Reihl. Surface electronic structure of Si(111)7×7-Ge and Si(111)5×5-Ge studied with photoemission and inverse photoemission. *Phys. Rev. B*, 36(11):5974–5981, Oct 1987.
- [96] R. I. G. Uhrberg, T. Kaurila, and Y.-C. Chao. Low-temperature photoemission study of the surface electronic structure of Si(111)7 × 7. *Phys. Rev. B*, 58(4):R1730–R1733, Jul 1998.
- [97] R. Losio, K. N. Altmann, and F. J. Himpsel. Fermi surface of Si(111)7x7. *Phys. Rev. B*, 61(16):10845–10853, Apr 2000.

- [98] R. J. Hamers, R. M. Tromp, and J. E. Demuth. Surface electronic structure of Si(111)-(7×7) resolved in real space. *Phys. Rev. Lett.*, 56(18):1972–1975, May 1986.
- [99] R. Wolkow and Ph. Avouris. Atom-resolved surface chemistry using scanning tunneling microscopy. *Phys. Rev. Lett.*, 60(11):1049–1052, Mar 1988.
- [100] F. J. Himpsel and Th. Fauster. Probing valence states with photoemission and inverse photoemission. *Journal of Vacuum Science and Technology A: Vacuum, Surfaces, and Films*, 2(2):815–821, 1984.
- [101] J. M. Nicholls and B. Reihl. Adatom electronic structure of the Si(111)7×7 surface. *Phys. Rev. B*, 36(15):8071–8074, Nov 1987.
- [102] F. J. Himpsel. Inverse photoemission from semiconductors. *Surface Science Reports*, 12:3–48, 1990.
- [103] U. Backes and H. Ibach. Evidence for a 2d-metallic state of the clean 7 x 7 Si(111) surface. *Solid State Communications*, 40:575–577, 1981.
- [104] J. E. Demuth, B. N. J. Persson, and A. J. Schellsorokin. Temperature-dependent surface-states and transitions of Si(111)-7x7. *Phys. Rev. Lett.*, 51(24):2214–2217, 1983.
- [105] J. M. Layet, J. Y. Hoarau, H. Lüth, and J. Derrien. Dispersion of the dangling-bond surface states of Si(111)-(7×7). *Phys. Rev. B*, 30(12):7355–7357, Dec 1984.
- [106] D. Fick, R. Veith, H. D. Ebinger, H. J. Jänsch, C. Weindel, H. Winnefeld, and J. J. Paggel. Electron correlations in the clean and hydrogen-covered Si(111)-(7×7) surface at extremely low Li coverages. *Phys. Rev. B*, 60(12):8783–8790, Sep 1999.
- [107] R. Schillinger, C. Bromberger, H. J. Jansch, H. Kleine, O. Kuhlert, C. Weindel, and D. Fick. Metallic Si(111)-(7x7)-reconstruction: A surface close to a Mott-Hubbard metal-insulator transition. *Phys. Rev. B*, 72(11):115314, Sep 2005.
- [108] B. N. J. Persson. Electronic conductivity of Si(111)-7×7. *Phys. Rev. B*, 34(8):5916–5917, Oct 1986.
- [109] Seiji Heike, S. Watanabe, Y. Wada, and T. Hashizume. Electron conduction through surface states of the Si(111)-(7 × 7) surface. *Phys. Rev. Lett.*, 81(4):890–893, 1998.

- [110] Y. Hasegawa, Lyo I.-W., and Ph. Avouris. Measurement of surface state conductance using stm point contacts. *Surf. Sci.*, 357-358:32, 1996.
- [111] Kwonjae Yoo and H. H. Weitering. Electrical conductance of reconstructed silicon surfaces. *Phys. Rev. B (Condensed Matter and Materials Physics)*, 65(11):115424, 2002.
- [112] S. Hasegawa and S. Ino. *Phys. Rev. Lett.*, 68(8):1192–5, 1992.
- [113] T. Tanikawa, K. Yoo, I. Matsuda, S. Hasegawa, and Y. Hasegawa. Non-metallic transport property of the Si(111)7x7 surface. *Phys. Rev. B*, 68(11):113303, Sep 2003.
- [114] <http://en.wikipedia.org/wiki/metallic>.
- [115] T. Takahashi, S. Nakatani, N. Okamoto, T. Ishikawa, and S. Kikuta. Study on the Si(111) $\sqrt{3} \times \sqrt{3}$ -Ag surface structure by X-ray diffraction. *Jpn. J. Appl. Phys. 2, Lett. (Japan)*, 27(5):753 – 5, 1988/05/.
- [116] M. Katayama, R. S. Williams, M. Kato, E. Nomura, and M. Aono. Structure analysis of the Si(111) $\sqrt{3} \times \sqrt{3}$ r30°-Ag surface. *Phys. Rev. Lett.*, 66(21):2762–2765, May 1991.
- [117] Toshio Takahashi, Shinichiro Nakatani, Naoko Okamoto, Tetsuya Ishikawa, and Seishi Kikuta. A study of the Si(111)-Ag surface by transmission x-ray diffraction and x-ray diffraction topography. *Surface Science*, 242(1-3):54–58, 1991.
- [118] H. Aizawa, M. Tsukada, N. Sato, and S. Hasegawa. Asymmetric structure of the Si(111)($\sqrt{3} \times \sqrt{3}$)Ag surface. *Surface Science*, 429(1-3):L509–L514, 1999.
- [119] S. Watanabe, Y. Kondo, Y. Nakamura, and J. Nakamura. Atomic and electronic structure of the Si(111)($\sqrt{3} \times \sqrt{3}$)Ag surface reexamined using first-principles calculations. *Science and Technology of Advanced Materials*, 1:167–172, 2000.
- [120] Iwao Matsuda, Harumo Morikawa, Canhua Liu, Satoru Ohuchi, Shuji Hasegawa, Taichi Okuda, Toyohiko Kinoshita, Carlo Ottaviani, Antonio Cricenti, Marie D’angelo, Patrick Soukiassian, and Guy Le Lay. Electronic evidence of asymmetry in the Si(111)($\sqrt{3} \times \sqrt{3}$)Ag structure. *Phys. Rev. B (Condensed Matter and Materials Physics)*, 68(8):085407, 2003.

- [121] K. Takahashi, H. Tajiri, K. Sumitani, K. Akimoto, H. Sugiyama, Xiaowei Zhang, and H. Kawata. X-ray diffraction study of the phase transition of the Si(111)($\sqrt{3} \times \sqrt{3}$)Ag surface. *Surf. Rev. Lett. (Singapore)*, 10(2-3):519 – 24, 2003/04/.
- [122] H. Nakahara, T. Suzuki, and A. Ichimiya. Ag/Si(1 1 1) surface phase transition at low temperature studied by RHEED. *Applied Surface Science*, 234(1-4):292–296, 2004.
- [123] K. J. Wan, X. F. Lin, and J. Nogami. Reexamination of the Ag/Si(111)- $\sqrt{3} \times \sqrt{3}$ surface by scanning tunneling microscopy *Phys. Rev. B (Condensed Matter)*, 45(16):9509–12, 1992.
- [124] N. Sato, T. Nagao, and S. Hasegawa. Si(111)-($\sqrt{3} \times \sqrt{3}$)-Ag surface at low temperatures: symmetry breaking and surface twin boundaries *Surface Science*, 442(1):65–73, 1999.
- [125] Iwao Matsuda, Toru Hirahara, Mitsuru Konishi, Canhua Liu, Harumo Morikawa, Marie D’angelo, Shuji Hasegawa, Taichi Okuda, and Toyohiko Kinoshita. Evolution of Fermi surface by electron filling into a free-electronlike surface state. *Phys. Rev. B*, 71(23):235315, 2005.
- [126] J. M. Nicholls, F. Salvan, and B. Reihl. Surface states of ordered Au, Ag, and Cu overlayers on Si(111) studied by inverse photoemission. *Phys. Rev. B*, 34(4):2945–2948, Aug 1986.
- [127] S. Kono, K. Higashiyama, T. Kinoshita, T. Miyahara, H. Kato, H. Oh-sawa, Y. Enta, F. Maeda, and Y. Yaegashi. Surface and bulk core-level shifts of the Si(111) $\sqrt{3} \times \sqrt{3}$ -Ag surface: Evidence for a charged $\sqrt{3} \times \sqrt{3}$ layer. *Phys. Rev. Lett.*, 58(15):1555–1558, Apr 1987.
- [128] G. S Herman, J. C. Woicik, A. B. Andrews, and J. L. Erskine. High-resolution photoelectron spectroscopy study of ($\sqrt{3} \times \sqrt{3}$)r30°-Ag on Si(111). *Surface Science*, 290:L643–L648, 1993.
- [129] K. Markert, P. Pervan, W. Heichler, and K. Wandelt. Structural and electronic properties of Ag/Si(111) and Au/Si(111) surfaces. *Journal of Vacuum Science and Technology A: Vacuum, Surfaces, and Films*, 7(4):2873–2878, 1989.
- [130] L. S. O. Johansson, E. Landemark, C. J. Karlsson, and R. I. G. Uhrberg. Fermi-level pinning and surface-state band structure of the Si(111)-($\sqrt{3} \times \sqrt{3}$)r30°-Ag surface. *Phys. Rev. Lett.*, 63(19):2092–2095, Nov 1989.

- [131] Y. Nakajima, S. Takeda, T. Nagao, and S. Hasegawa. Surface electrical conduction due to carrier doping into a surface-state band on Si(111)($\sqrt{3} \times \sqrt{3}$)Ag. *Phys. Rev. B: Condensed Matter*, 56(11):6782–, 1997.
- [132] J. Viernow, M. Henzler, W. L. O’Brien, F. K. Men, F. M. Leibsle, D. Y. Petrovykh, J. L. Lin, and F. J. Himpsel. Unoccupied surface states on Si(111) $\sqrt{3} \times \sqrt{3}$ -Ag. *Phys. Rev. B*, 57(4):2321–2326, Jan 1998.
- [133] G. Le Lay, M. Gothelid, A. Cricenti, C. Hakansson, and P. Perfetti. Atomic origins of the si 2p surface core-level shifts of the ”prototypical” Si(111)($\sqrt{3} \times \sqrt{3}$)r(30 degrees)-Ag structure. *Europhysics Letters*, 45(1):65–70, Jan 1999.
- [134] E. J. van Loenen, J. E. Demuth, R. M. Tromp, and R. J. Hamers. Local electron states and surface geometry of Si(111)- $\sqrt{3} \times \sqrt{3}$ Ag. *Phys. Rev. Lett.*, 58(4):373–376, Jan 1987.
- [135] R. J. Wilson and S. Chiang. Structure of the Ag/Si(111) surface by scanning tunneling microscopy. *Phys. Rev. Lett.*, 58(4):369–372, Jan 1987.
- [136] K. J. Wan, X. F. Lin, and J. Nogami. Reexamination of the Ag/Si(111)- $\sqrt{3} \times \sqrt{3}$ surface by scanning tunneling microscopy. *Phys. Rev. B*, 45(16):9509–9512, Apr 1992.
- [137] J. M. Carpinelli and H. H. Weitering. Low-temperature reconstruction pathway to the Si(111)($\sqrt{3} \times \sqrt{3}$)r30°-Ag interface. *Phys. Rev. B*, 53(19):12651–12654, May 1996.
- [138] D. W. McComb, D. J. Moffatt, P. A. Hackett, B. R. Williams, and B. F. Mason. Scanning-tunneling-microscopy investigation of the nucleation and growth of Ag/Si(111)-($\sqrt{3} \times \sqrt{3}$). *Phys. Rev. B*, 49(24):17139–17148, Jun 1994.
- [139] Y. Borensztein and R. Alameh. Optical evidence for interface electronic states at Ag/Si interfaces. *Surface Science*, 274:L509–L514, 1992.
- [140] S. Watanabe, M. Aono, and M. Tsukada. Theoretical calculations of the scanning-tunneling-microscopy images of the Si(111) $\sqrt{3} \times \sqrt{3}$ -Ag surface. *Phys. Rev. B*, 44(15):8330–8333, Oct 1991.
- [141] Y. G. Ding, C. T. Chan, and K. M. Ho. Structure of the ($\sqrt{3} \times \sqrt{3}$)r30° Ag/Si(111) surface from first-principles calculations. *Phys. Rev. Lett.*, 67(11):1454–1457, Sep 1991.

- [142] Y. G. Ding, C. T. Chan, and K. M. Ho. Ding, Chan, and Ho reply. *Phys. Rev. Lett.*, 69(16):2452, Oct 1992.
- [143] J. N. Crain, K. N. Altmann, C. Bromberger, and F. J. Himpsel. Fermi surfaces of surface states on Si(111)-Ag, Au. *Phys. Rev. B*, 66(20):205302, Nov 2002.
- [144] R. I. G. Uhrberg, H. M. Zhang, T. Balasubramanian, E. Landemark, and H. W. Yeom. Photoelectron spectroscopy study of Ag/Si(111) $\sqrt{3} \times \sqrt{3}$ and the effect of additional Ag adatoms. *Phys. Rev. B*, 65(8):081305, Feb 2002.
- [145] J. N. Crain, M. C. Gallagher, J. L. McChesney, M. Bissen, and F. J. Himpsel. Doping of a surface band on Si(111)($\sqrt{3} \times \sqrt{3}$)Ag. *Phys. Rev. B*, 72(4):045312, Jul 2005.
- [146] L.J. van der Pauw. *Philips Res. Rep.*, 13:1, 1958.
- [147] R. Schad, S. Heun, T. Heidenblut, and M. Henzler. Metallic and nonmetallic conductivity of thin epitaxial silver films. *Phys. Rev. B*, 45(19):11430–11432, May 1992.
- [148] S. Hasegawa, I. Shiraki, T. Tanikawa, C.L. Petersen, T.M. Hansen, P. Boggild, and F. Grey. Direct measurement of surface-state conductance by microscopic four-point probe method. *Journal of Physics: Condensed Matter*, 14:8379 – 92, 2002.
- [149] G. Le Lay. Physics and electronics of the noble-metal/elemental-semiconductor interface formation: A status report. *Surface Science*, 132:169–204, 1983.
- [150] Katsuyoshi Kobayashi. Electrical resistance across a step of the Si(111)-Ag surface. *Surface Science*, 583(1):16–28, 2005.
- [151] Iwao Matsuda, Masashi Ueno, Toru Hirahara, Rei Hobarra, Harumo Morikawa, Canhua Liu, and Shuji Hasegawa. Electrical resistance of a monatomic step on a crystal surface. *Phys. Rev. Lett.*, 93(23):236801, 2004.
- [152] Y. Gotoh, S. Ino, and H. Komatsu. Effect of surface contamination on the Stranski-Krastanov growth mode of an Ag/Si system. *Journal of Crystal Growth*, 56(2):498–504, 1982.

- [153] Y. Gotoh and S. Ino. Surface-structures of Ag on Si(111) surface investigated by RHEED. *Japanese Journal of Applied Physics*, 17(12):2097–2109, 1978.
- [154] V. Perez-Dieste, J. F. Sanchez, M. Izquierdo, L. Roca, J. Avila, and M. C. Asensio. The growth of silver films on Si(1 1 1)-(7 x 7) studied by using photoelectron diffraction. *Applied Surface Science*, 212-213:235–243, 2003.
- [155] Y. Gotoh and S. Ino. Epitaxial-growth of silver on an Si(111) 7x7 surface at room-temperature. *Thin Solid Films*, 109(3):255–261, 1983.
- [156] S. Ino and Y. Gotoh. RHEED study of Si(111) surface-structures induced by Ag evaporation. *Japanese Journal of Applied Physics*, 16(12):2261–2262, 1977.
- [157] Lin Huang, S. J. Chey, and J. H. Weaver. Metastable structures and critical thicknesses: Ag on Si(111)-7x7. *Surface Science*, 416(1-2):L1101–6, 1998.
- [158] L. Gavioli, K. R. Kimberlin, M. C. Tringides, J. F. Wendelken, and Zhenyu Zhang. Novel growth of Ag islands on Si(111): Plateaus with a singular height. *Phys. Rev. Lett.*, 82(1):129–32, 1999.
- [159] Pavel Kocan, Pavel Sobotik, Ivan Ost’adal, and Miroslav Kotrla. Self-organized growth of Ag islands on Si(1 1 1)-(7 x 7)-optimization of an STM experiment by means of kMC simulations. *Surface Science*, 566-568:216–220, 2004.
- [160] P. Kocan, I. Ost’adal, and P. Sobotik. Growth of silver structures on silicon surfaces observed in vivo by scanning tunneling microscopy. *Surface Science*, In Press, Uncorrected Proof:–, 2006.
- [161] H. Hirayama, A. Yamasaki, and T. Kawata. Change of optical second harmonic generation intensity during Ag deposition on Si(1 1 1)7 x 7 and Si(1 1 1)-Ag surfaces. *Surface Science*, 532-535:922–927, 2003.
- [162] Robert L. Park, B. T. Jonker, H. Iwasaki, and Q. G. Zhu. Quantum size effects in the reflection of slow electrons from thin films. *Applications of Surface Science*, 22-23:1–13, 1985.
- [163] Thomas G. Pedersen, Kjeld Pedersen, and Thomas B. Kristensen. Optical second-harmonic generation as a probe of quantum well states in ultrathin Au and Ag films deposited on Si(111). *Thin Solid Films*, 364:86–90, 2000.

- [164] Kjeld Pedersen, Thomas B. Kristensen, Thomas G. Pedersen, Per Morgen, Zheshen Li, and Soren V. Hoffmann. Optical second-harmonic generation and photoemission from quantum well states in thin Ag films on Si(1 1 1). *Surface Science*, 482-485:735–739, 2001.
- [165] I. Matsuda and Han Woong Yeom. Study of the quantum-well states in ultra-thin silver films on Si surfaces. *Journal of Electron Spectroscopy and Related Phenomena*, 126(1-3):101–15, 2002.
- [166] D.R. Smith and F.R. Fickett. Low-temperature properties of silver. *Journal of Research of the National Institute of Standards and Technology*, 100(2):119, 1995.
- [167] P. Segovia, D. Purdie, M. Hengsberger, and Y. Baer. Observation of spin and charge collective modes in one-dimensional metallic chains. *Nature*, 402:504–507, 1999.
- [168] Johannes V. Barth, Giovanni Costantini, and Klaus Kern. Engineering atomic and molecular nanostructures at surfaces. *Nature*, 437:671–679, 2005.
- [169] Mustafa M. Ozer, James R. Thompson, and Hanno H. Weitering. Hard superconductivity of a soft metal in the quantum regime. *Nat Phys*, 2:173–176, 2006.
- [170] A. Rota, A. Martinez-Gil, G. Agnus, E. Moyen, T. Maroutian, B. Bartenlian, R. Megy, M. Hanbucken, and P. Beauvillain. Au island growth on a Si(1 1 1) vicinal surface. *Surface Science*, 600:1207–1212, 2006.
- [171] J.-L. Lin, D. Y. Petrovykh, J. Viernow, F. K. Men, D. J. Seo, and F. J. Himpsel. Formation of regular step arrays on Si(111)7 x 7. *Journal of Applied Physics*, 84(1):255–260, 1998.
- [172] Yu Suzuki. Private communication.
- [173] J. Kuntze, A. Mugarza, and J. E. Ortega. Ag-induced zero- and one-dimensional nanostructures on vicinal Si(111). *Applied Physics Letters*, 81(13):2463–2465, 2002.
- [174] S. Hasegawa, I. Shiraki, F. Tanabe, R. Hobara, T. Kanagawa, T. Tanikawa, I. Matsuda, C.L. Petersen, T.M. Hansen, P. Boggild, and F. Grey. Electrical conduction through surface superstructures measured by microscopic four-point probes. *Surf. Rev. Lett. (Singapore)*, 10(6):963 – 80, 2003/12/.

- [175] T. U. Kampen. Private communication.
- [176] C. H. Wu, C. Jacob, X. J. Ning, S. Nishino, and P. Pirouz. Epitaxial growth of 3C—SiC on Si(111) from hexamethyldisilane. *Journal of Crystal Growth*, 158:480–490, 1996.
- [177] Yu Suzuki, Michael Hietschold, and Dietrich R. T. Zahn. Growth of copper phthalocyanine on hydrogen passivated vicinal silicon(1 1 1) surfaces. *Applied Surface Science*, In Press, Corrected Proof:–, 2006.
- [178] D.K. Ferry and S.M. Goodnick. *Transport in Nanostructures*. Cambridge University Press, 1 ed. 1997.
- [179] G. Hollinger and F. J. Himpsel. Oxygen chemisorption and oxide formation on Si(111) and Si(100) surfaces. *Journal of Vacuum Science and Technology A: Vacuum, Surfaces, and Films*, 1(2):640–645, 1983.
- [180] <http://ece-www.colorado.edu/~bart/book/book/>.
- [181] H. Luth. *Surfaces and Interfaces of Solid Materials*. Springer, third edition, 1992.
- [182] D. A. Evans, H. J. Steiner, A. R. Vearey-Roberts, V. Dhanak, G. Cabailh, S. O’Brien, I. T. McGovern, W. Braun, T. U. Kampen, S. Park, and D. R. T. Zahn. Perylenes and phthalocyanines on GaAs(0 0 1) surfaces. *Applied Surface Science*, 212-213:417–422, 2003.
- [183] G. Salvan, S. Silaghi, B. Paez, T. U. Kampen, and D. R. T. Zahn. Modification of GaAs(1 0 0) surfaces upon adsorption of perylene derivatives. *Applied Surface Science*, 234:178–184, 2004.
- [184] N. Papageorgiou, J. C. Mossoyan, M. Mossoyan-Deneux, G. Terzian, E. Janin, M. Gothelid, L. Giovanelli, J. M. Layet, and G. Le Lay. High resolution synchrotron radiation PES study of PbPC deposited on Pt(111). *Applied Surface Science*, 162-163:178–183, 2000.
- [185] A. Das, G. Salvan, T. U. Kampen, W. Hoyer, and D. R. T. Zahn. Influence of substrate surfaces on the growth of organic films. *Applied Surface Science*, 212-213:433–437, 2003.
- [186] T. U. Kampen, G. Salvan, A. Paraian, C. Himcinschi, A. Yu. Kobitski, M. Friedrich, and D. R. T. Zahn. Orientation of perylene derivatives on semiconductor surfaces. *Applied Surface Science*, 212-213:501–507, 2003.

- [187] K. McElroy, Jinho Lee, J. A. Slezak, D. H. Lee, H. Eisaki, S. Uchida, and J. C. Davis. Atomic-scale sources and mechanism of nanoscale electronic disorder in $\text{Bi}_2\text{Sr}_2\text{CaCu}_2\text{O}_{8+\delta}$. *Science*, 309(5737):1048–52, 2005.
- [188] R. Macovez, C. Cepek, M. Sancrotti, A. Goldoni, L. Petaccia, R. Larciprete, and S. Lizzit. Ultra-high-vacuum epitaxial growth of $\text{MgB}_2(0001)$ thin films on $\text{Mg}(0001)$ via molecular beam epitaxy. *Journal of Physics: Condens. Matter*, 16:S3451–S3458, 2004.
- [189] O. Gunnarsson. Superconductivity in fullerides. *Rev. Mod. Phys.*, 69(2):575–606, Apr 1997.
- [190] A. F. Hebard, M. J. Rosseinsky, R. C. Haddon, D. W. Murphy, S. H. Glarum, T. T. M. Palstra, A. P. Ramirez, and A. R. Kortan. Superconductivity at 18 K in potassium-doped C_{60} . *Nature*, 350:600, 1991.
- [191] D. M. Poirier. Isolation of fulleride phases by distillation. *Applied Physics Letters*, 64(11):1356–1358, 1994.
- [192] Steven C. Erwin and Mark R. Pederson. Electronic structure of crystalline K_6C_{60} . *Phys. Rev. Lett.*, 67(12):1610–1613, Sep 1991.
- [193] A. Goldoni, Sangaletti, Parmigiani L., F. Comelli, G., and G. Paolucci. Surface and bulk normal state transport properties in K_3C_{60} . *Phys. Rev. Lett.*, 87:076401, 2001.
- [194] R. W. Lof, M. A. van Veenendaal, B. Koopmans, H. T. Jonkman, and G. A. Sawatzky. Band gap, excitons, and coulomb interaction in solid C_{60} . *Phys. Rev. Lett.*, 68(26):3924–3927, Jun 1992.
- [195] R. Lin, P. Boggild, and O. Hansen. Microcantilever equipped with nanowire template electrodes for multiprobe measurement on fragile nanostructures. *Journal of Applied Physics*, 96(5):2895–2900, 2004.
- [196] S. Hasegawa, N. Sato, I. Shiraki, C. L. Petersen, P. Boggild, T. M. Hansen, T. Nagao, and F. Grey. *Japanese Journal of Applied Physics, Part 1 (Regular Papers, Short Notes & Review Papers)*, 39(6B):3815–22, 2000.